Investigation of structural properties in biomolecular systems using synchrotron-based spectroscopies

Dissertation
zur Erlangung des akademischen Grades
Doctor rerum naturalium
(Dr. rer. nat.)

vorgelegt der Fakultät Mathematik und Naturwissenschaften der
Technischen Universität Dresden von

Dipl.-Phys. Kurt Kummer

geboren am 27. Dezember 1982 in Schwedt/Oder

Eingereicht am 25. November 2009

Die Dissertation wurde in der Zeit von Oktober 2007 bis November 2009
am Institut für Festkörperphysik angefertigt.

Gutachter: Prof. Dr. Clemens Laubschat (TU Dresden)

Prof. Dr. Eckhardt Rühl (FU Berlin)

Abstract

Solid state approaches to structural properties like diffraction or microscopy techniques often cannot be applied to biomolecular systems, at least not without special post-preparation which often corrupts the desired properties of the pristine systems. In this work the capabilities of synchrotron-based, soft X-ray spectroscopies as an alternative way to unravel structural properties of such systems are tested. To this end, three exemplary systems were investigated each with the focus on another facet and characteristic length scale. The first example are DNA-alkanethiol self-assembled monolayers, also known as DNA microarrays or DNA chips, for which a way to monitor and controllably tune the structural composition on the mesoscopic scale of many thousands of molecules was sought for. The second example focuses on the single-molecule and submolecular scale in metal-protein hybrid compounds with the aim to identify the binding site of metal atoms or ions within protein molecules and the underlying interaction mechanisms. The most fundamental structural scale, the level of single bonds and molecular orbitals, is addressed in the last example where it was tried to elaborate an approach to map the topology of molecular orbitals based upon X-ray absorption properties. This approach was put to the practical test for the characteristic $\pi^*_{peptide}$ orbitals in protein backbones. For all three investigated examples, spectroscopies using soft X-ray synchrotron radiation were able to extract the desired information, thus confirming that they may grant alternative access to structural properties of soft-matter systems in cases where standard approaches fail.

Kurzfassung

Klassische Festkörpertechniken zur Strukturuntersuchung, wie Streu- oder Mikroskopiemethoden, können häufig nicht auf Biomolekülsysteme angewandt werden, zumindest nicht ohne spezielle Postpräparation, die die ursprünglichen Eigenschaften dieser Systeme oft verfälscht. In dieser Arbeit soll untersucht werden, inwieweit Röntgenspektroskopien basierend auf Synchrotronstrahlung einen alternativen Zugang zu Struktureigenschaften solcher Systeme bieten. Dazu wurden drei Systeme exemplarisch untersucht, jeweils mit Schwerpunkt auf einen anderen Aspekt und charakteristischen Längenbereich. Für selbstorganisierende DNA-Alkanthiol-Schichten, sogenannte DNA-Chips, wurde nach eine Weg gesucht, ihre strukturelle Zusammensetzung auf der mesoskopischen Ebene vieler tausend Moleküle zu bestimmen und kontrolliert zu modifizieren. Metallisierte Proteinstrukturen wurden auf Einzelmolekül- bzw. submolekularer Ebene untersucht, mit dem Ziel, die Orte der Metallanlagerung innerhalb des Proteins und die zugrundeliegenden Wechselwirkungsmechanismen zu identifizieren. Die unterste strukturelle Ebene, der Bereich einzelne Bindungen und Molekülorbitale, wurde adressiert am Beispiel der $\pi^*_{peptide}$ Orbitale des Proteinrückrats. Dafür wurde eine Methode zur Kartographierung einzelner Orbitale anhand von Röntgenabsorptionseigentschaften herausgearbeitet und praktisch getestet. In allen drei Fällen konnten Röntgenspektroskopien die nötigen Informationen liefern und damit ihr Potential für Strukturuntersuchungen in weicher Materie unter Beweis stellen.

Contents

1 Preface

Since about 20 years ago when biotechnology and organic semiconductor technologies began to rise research into organic and biomolecules has found a renaissance and has constantly intensified ever since. Today these systems are subject to one of the most lively branches of material science and the inexhaustible fund of organic compounds makes them an oceanic pool for diverse technological applications spanning various imaginable fields from organic solar cells and LEDs over biosensors to molecular computing. The main reason for this success is that these new materials do reveal numerous new and unique properties when compared to hitherto employed inorganic compounds.

One and possibly the most striking principally new aspect of organic and biological systems is their capability to self-organize into even highly complex functional structures. With that bottom-up fabrication, i.e. the self-assembly of entire technological units from solutes without external steering, comes into sight. Naturally, the development and purposeful application of such revolutionary new fabrication methods would always require a way to monitor composition and properties of the resulting nanoscopic structures. Unfortunately, those techniques that are routinely applied to characterize structural properties of "classical", inorganic systems are in many cases not well-suited for this purpose. Reciprocal or real-space imaging, i.e. diffraction or high-resolution microscopy techniques, reach their limitations when it comes to soft matter structures. Microscopic studies are often not suitable, because they are relatively slow, not chemically selective and require special post-preparation of the samples, which rules them out for *in situ* monitoring of the formation process of such structures. The absence of *3-dimensional* crystalline order, on the other hand, often precludes the use of diffraction methods.[1]

In certain cases the application of synchrotron-based spectroscopies could open an alternative pathway towards the desired structural information. Although these spectroscopies address the electronic rather than the spatial structure of matter they can also provide with some insight into the latter because of the close correlation between both. In the present work, the capability of spectroscopies using soft X-ray synchrotron radiation for structural characterization of biomolecular systems is tested at three distinct exam-

---

[1]Note that, to date, X-ray diffraction is the major tool to explore the spatial structure of proteins. However, its application is bound to the availability of specifically grown protein crystals.

ples, each of them with relevance for present or future applications. In all three cases the classical imaging tools could not have helped to resolve the open puzzles. Moreover, the examples were chosen such that they cover very diverse length scales from the extended nanometer scale to the scale of single molecular subgroups and atoms down to the scale of individual orbitals. In this way, it will be tried to give an estimate of the might and application range of synchrotron-based, soft X-ray spectroscopies as an unconventional tool for structure-related studies of biomolecular systems.

The first example is that of DNA microarrays studied on the mesoscopic scale and thus covering a large number of molecules at the same time with the intention to unravel the intermolecular interactions during their self-assembly and the resulting structural properties. The application of X-ray photoemission spectroscopy (XPS) allowed to find a way how to monitor and controllably tune the structure and therewith the performance of DNA microarrays. The second example aims into the field of hybrid metal-biomolecule compounds. There it is tried to answer the question how the binding sites of metal atoms in a complex biomolecule can be identified and how the interaction between metal and biological species can be characterized experimentally. The third example penetrates into the most fundamental structural level of biomolecules, the level of single bonds, and discusses how the topology of even individual molecular orbitals can be explored, at the example of a huge protein composed of thousands of atoms.

Beside this introduction the present work consists of five more chapters. It will proceed with a short introduction into the applied synchrotron-based spectroscopic techniques covering both their fundamentals as well as their experimental realization. This chapter will be followed by three chapters, each on one of the above mentioned examples, where the capability of those techniques to unravel structural properties of biomolecular systems is put to the practical test. The final chapter will then give a short summary of the obtained results.

2 Synchrotron-based spectroscopies in the soft X-ray range

2.1 Photoelectron spectroscopy

Photoelectron spectroscopy is a powerful tool to probe the occupied electronic states in atoms, molecules and solids using the photoelectric effect [1]. Thereby, an electron is excited into free continuum states above the vacuum level E_{vac} by absorption of a photon of sufficiently high energy. The kinetic energy of the excited electron depends on both its binding energy (BE) and the photon energy. In the photon energy range below 80 eV this method is often referred to as ultraviolet photoelectron spectroscopy (UPS) and particularly useful for probing valence states, whereas at higher photon energies it is denoted as X-ray photoelectron spectroscopy (XPS) and allows to access core-level states.

2.1.1 Basic principles

The photoemission (PE) process can be considered as a perturbation of the electronic ground-state $|i\rangle$ of a system by an incident electromagnetic field upon which an electron is excited out of the system into free continuum states $|j\rangle$ above the vacuum level E_{vac}. Using first order perturbation theory this process can be theoretically described using Fermi's golden rule

$$P_{ij} = \frac{2\pi}{\hbar} \frac{e^2}{4m^2} \left| \langle j \,|\, \hat{\boldsymbol{p}} \, \boldsymbol{A} + \boldsymbol{A} \, \hat{\boldsymbol{p}} |\, i \rangle \right|^2 \rho_j \times \delta_E \, \delta_{\boldsymbol{k}} \, \delta_J \qquad (2.1)$$

with $\boldsymbol{A}$ the vector potential of the electromagnetic field, $\hat{\boldsymbol{p}}$ the momentum operator and ρ_j the density of final states, where we have neglected nonlinear terms in $\boldsymbol{A}$. The first term determines the excitation probability while the second term ensures conservation of energy (δ_E), momentum ($\delta_{\boldsymbol{k}}$) and angular momentum (δ_J).

Because of the conservation of energy and momentum during the photoemission process the outcoming electrons carries information on both energy and dispersion of the excited
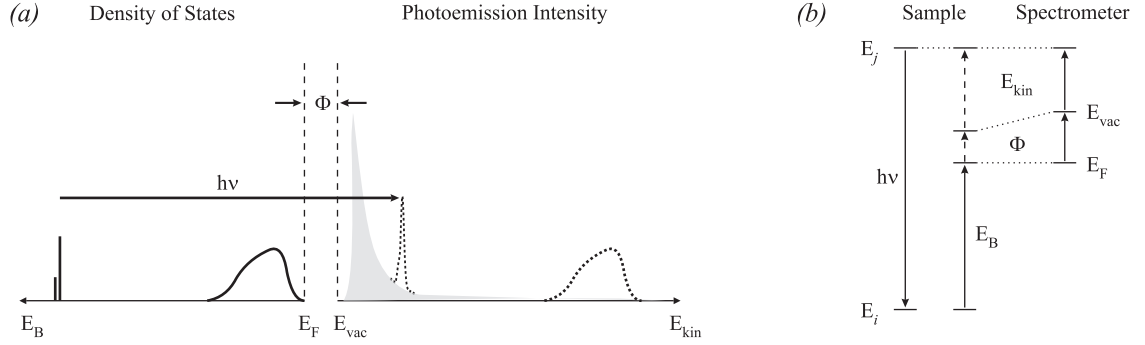
Figure 2.1: (a) Because of energy conservation the kinetic energy distribution of the photoelectrons reflects the density of electronic states in the probed sample. The grey-shaded area is to indicate the spectral contribution of photoelectrons inelastically scattered prior to detection. (b) Energy scheme of the PE process.

electronic states. Thus by detection of the kinetic energy and the emission angle of the excited electron one can obtain insight into the electronic structure of the probed sample. Angle-resolved photoelectron spectroscopy (ARPES) is usually applied to map the band structure of the dispersive valence states in crystalline solids which lie at low binding energies. In the present work, however, biomolecular samples with no crystal order and thus no dispersive electronic states were investigated. Therefore, all PE spectra were recorded in the angle-integrated mode where one sums up over many directions k and measures only the energy distribution of the emitted electrons at a fixed photon energy. This is illustrated in *Figure 2.1a*. The principal energy balance is given by the following equation

$$E_{kin} = h\nu - E_B - \Phi \tag{2.2}$$

with E_{kin} the kinetic energy of the detected photoelectron, $h\nu$ the photon energy, E_B the binding energy with respect to the Fermi level and Φ the work function of the spectrometer (see also *Figure 2.1b*).

It should be noted that in order to determine electron binding energies it is not sufficient enough to fix the photon energy and measure the kinetic energy distribution, but it is also required to know Φ. However, accurate measurements of the spectrometer work function are usually time-consuming. The most common approach to align PE spectra on the binding energy scale is therefore to use the Fermi step or a core-level line of a metallic reference sample, e.g. the Au $4f_{7/2}$ line at 84.0 eV, for energy calibration. When measured in the same experimental setup the energy separation between a sample PE line and the reference PE line enables determination of E_B using (2.2) without knowledge of the actual work function (and photon energy).

$$E_B = E_{B,ref} - (E_{kin,ref} - E_{kin}) = E_{B,ref} - \Delta E_{kin} \tag{2.3}$$

In the present work, this approach is standardly applied to connect kinetic and binding energy scale.

2.1.2   Core-level energy shifts in photoemission spectra

Often also referred to as chemical shifts, core-level shifts are possible binding energy differences of core-level states in molecules and solids with respect to the free atom. These shifts generally occur for two different reasons. On the one hand there might be an actual difference in the ground-state binding energy, related to so-called initial-state effects. On the other hand, the transition energy into the detected final-state is usually affected by correlation and relaxation effects during the photoemission process. These so-called final-state effects are no real property of the electronic ground state itself but rather a result of its high-energy photoexcitation. Both initial and final state effects on core-level binding energies can be exploited for chemical analysis using electron spectroscopy [2, 3].

Ground state charge transfer

The exact core-level binding energy of an atom of a particular element depends on its chemical environment. Considering an electron in a core-level state, its binding energy is in first approximation determined by the Coloumb potential generated by the atomic nucleus and the other electrons. Any change in the chemical environment will cause a spatial redistribution of the valence electron density, resulting in a changed potential as seen by the core electron and therewith in a shifted binding energy. Electron charge transfer away from the considered atom will decrease the ability of the valence electron system to screen the core-level electrons from the core potential and vice versa. Thus, as a general rule, core-level electrons of atoms surrounded by a low electronegativity, electron donating environment should show lower binding energies and those in a high electronegativity environment higher binding energies as compared to the monoelemental molecule or solid.

A simple but prominent example is the lithium $1s$ level in lithium metal and lithium oxide. A schematic picture of the electronic structure of these two compounds is given in *Figure 2.2*a. In lithium metal the $2s$ electrons exhibit wave functions delocalized over the whole solid with a finite probability density around the lattice sites of the Li atoms. They can thus contribute to the screening of the Li $1s$ electrons from the core potential. In lithium oxide on the other hand, the Li $2s$ charge is basically localized around the strongly electronegative oxygen site in order to establish the preferred closed $2p^6$ configuration. Because of the now strongly reduced valence electron charge density in the vicinity of the lithium core, their screening effect for the Li $1s$ electrons is lost, resulting in a higher binding energy. In turn, the O $1s$ binding energy is reduced due to additional screening by the two added $2p$ electrons. Another example of the influence of ground state charge transfer in PE spectra is given in *Figure 2.2*b at the example of the ethyl trifluoracetate molecule. The impact of the increasingly electronegative chemical environment on the C $1s$ binding energies is striking. These examples unambiguously demonstrate that though a simplification the initial state picture of ground-state charge transfer already yields in many cases successful explanation of core-level shifts. This applies in particular for low-
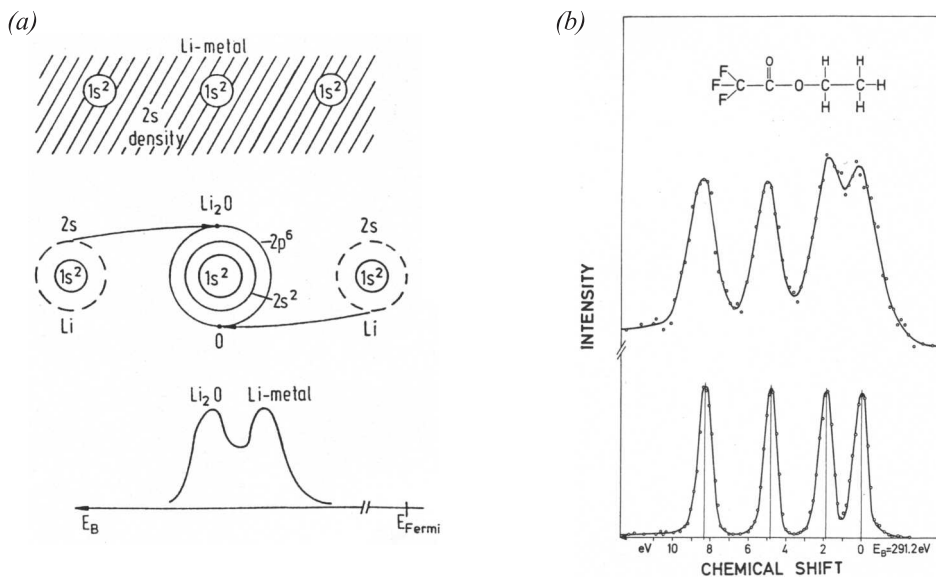
Figure 2.2: *(a) Schematic of the electronic structure and the Li 1s PE spectrum of lithium metal and lithium oxide. In lithium oxide the Li 2s charge is basically transfered to the oxygen site and thus does not contribute anymore to the core potential screening. Accordingly, the Li 1s binding energy increases compared to the metal. (b) Impact of increasingly electronegative binding partners of carbon in ethyl trifluoracetate on the C 1s electron binding energies.*

Z molecules, like the here discussed biomolecules, where electron correlations effects are rather minor [4].

Core-hole effect and core-hole screening

An aspect of photoelectron spectroscopy, one should be fully aware of, is that the photoe-mission final state is lacking one electron with respect to the initial state. Therefore, PE spectroscopy does not yield ground state energies but always energy differences between initial and final state. The binding energy of a photoelectron emitted from an N electron system is thus given by

$$E_B = E_j^{N-1} - E_i^N \qquad (2.4)$$

where E_j^{N-1} and E_i^N stand for the energies of the $(N-1)$ and N electron system in the final and initial state, respectively, where the final state system exhibits the surplus positive charge of the generated core hole. This is often denoted as "core-hole" effect and usually restricts access to total energies in practice.

There are a couple of theoretical approaches trying to relate the measured binding energies to single particle energies as obtained e.g. by Hartree-Fock or band-structure calculations. The simplest one assumes, that electrostatic screening of the photo-hole takes place instantaniously and that there are no energy relaxations of other orbitals, i.e.

electron-electron and electron-hole interactions are completely ignored. In fact, this approach works well for the interpretation of valence band spectra of solids, where the number N of itinerant electrons is large and the spatial distribution of the screening charge is similar to that of the photo-hole. It fails, however, for core-level spectroscopics where the effect of a localized hole cannot be fully compensated by occupation of extended screening orbitals. In this case, the $(Z + 1)$-approximation may be applied that accounts for intraatomic relaxations replacing a core-ionized atom of atomic number Z by a valence -ionized atom of atomic number $(Z + 1)$. Assuming again immediate screening of the valence-ionized state the binding energy is now given by the energy difference of the respective single-particle energies of the $(Z + 1)$ and Z atoms [3].

For the present work, however, a more elemental consideration of the core-hole effect might be sufficient because the chemical shifts are compared only among the experimental data and not with theoretical results. Then, the core-hole impact should be similar for all PE spectra of a particular core-level, because in organic molecules with their largely overlapping orbitals the respective screening potential can always be immediately occupied by a transfer of valence charge. In addition, one might argue that the screening of the core-hole charge could be somehow enhanced at atomic sites with larger valence charge density, i.e. a less electronegative environment. This effect, however, would shift the measured core-level BE in the same direction as the discussed ground-state charge transfer. It is therefore reasonable to assume that for low-Z molecules the core-hole effect does not pervert interpretation of core-level shifts obtained within the initial state picture.

Free vs. surface-adsorbed molecules

When comparing photoemission spectra of adsorbed atoms and molecules with respective spectra of the free species in the gas-phase there is usually a difference in binding energy, when referred to the same vacuum level E_vac. For the same core level binding energies of the gas phase species can exceed those of the adsorbed one by 1 eV to 3 eV. This is due to many-body effects, that can lower the hole relaxation energy in the adsorbed species considerably [5].

Figure 2.3 gives a schematic explanation of the shift in final state binding energies of photoelectrons emitted from an adsorbed molecule. In general, photoemission of an electron from an surface-adsorbed atom or molecule leaves behind a core or valence hole in an environment very different from that in the free atom or molecule. The substrate surface can now be involved in the screening of the hole's positive charge by charge transfer to the adsorbate. In addition, surface charges due to excitation of surface plasmons can interact with both the created hole and the photoemitted electron. For strongly chemisorbed species the former process is dominant, whereas when the surface-adsorbate coupling is reduced the surface plasmon screening mechanism becomes important.
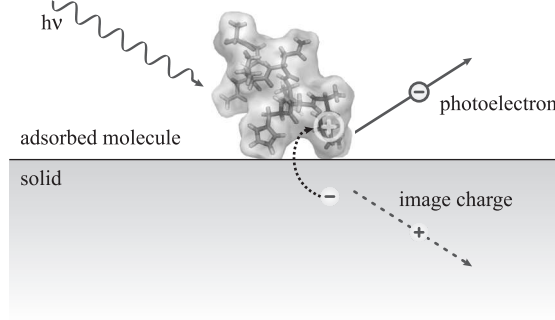
Figure 2.3: The substrate can be involved in the screening of the created photo-hole both by charge transfer to the adsorbate and by creation of a surface charge due to plasmon excitation. Furthermore, Coulomb interaction between the photoelectron and an associated surface charge can cause a further shift of the photoemission line.

2.1.3   Analysis of core-level PE spectra

Quantitative analysis of core-level PE spectra

Photoemission spectra can be analyzed not only with respect to the energy position of certain PE lines, but also quantitatively by comparison of their intensities. The intensity I_α of a PE line α is given by the following, phenomenological equation

$$I_\alpha = N_\alpha \, \sigma_\alpha(h\nu) \, J_{ph}(h\nu) \, \lambda(E_{kin}) \, D(E_{kin}) \, T(E_{pass}) \, K = N_\alpha \, \sigma_\alpha \, J_{ph} \, \lambda \, S \qquad (2.5)$$

where N_α denotes the number of probe atoms associated with the PE line α, σ_α the specific photoexcitation cross section of the excited core-level as a function of photon energy $h\nu$, J_{ph} the incident photon flux, λ the electron mean free path, K a constant accounting for experimental station design, D the detector efficiency, and T the analyzer transmission function. The three last-mentioned variables can be combined to the sensitivity S, which is a function of the photoelectron kinetic energy E_{kin} and the analyzer pass energy E_{pass}.

To enable comparison of intensities of different PE lines, they should be measured in the same kinetic energy window and with the same experimental settings, because then S and λ can be assumed as constant and one has to account only for the cross section and incident photon flux. The relative concentration C_α^{rel} of species α inside the sample is then given by

$$C_\alpha^{rel} = \frac{N_\alpha}{N} = \frac{I_\alpha/(\sigma_\alpha \, J_{ph,\alpha})}{\sum_n I_n/(\sigma_n \, J_{ph,n})}. \qquad (2.6)$$

where I_n denote the measured intensities, and σ_n and $J_{ph,n}$ are available from tabulated results of calculations [6] and the separately measured beamline photon flux curve, respectively. Moreover, if two PE components of one particular core-level spectrum are compared σ and J_{ph} become constant and the measured intensities I_n can be compared directly.
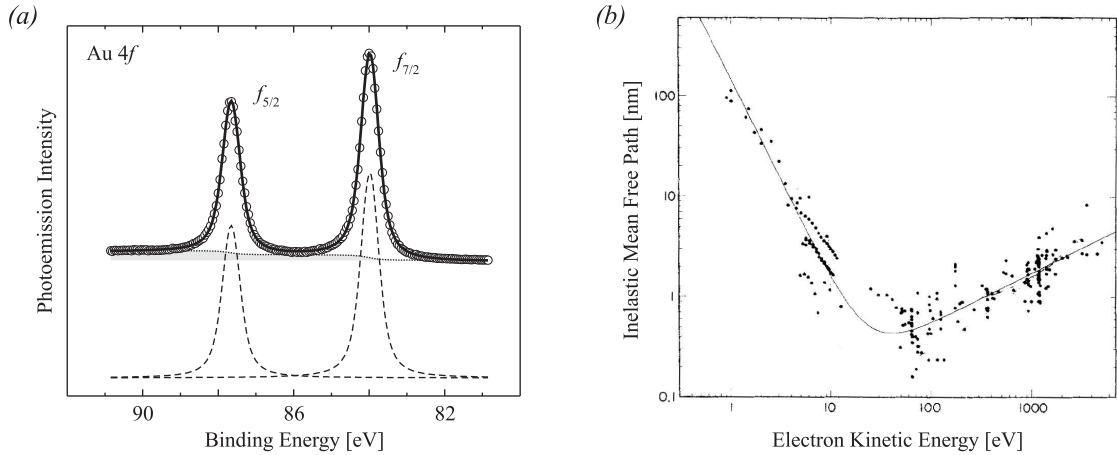
Figure 2.4: (a) Au 4f PE spectrum of a gold layer (circles) along with results of a least-squares fit analysis (lines). Assuming life-time broadened Lorentzians convoluted with a Gaussian function yields convincing agreement with the experimental line shape. The grey-shaded area denotes the Shirley background that was assumed to model inelastic contributions. (b) "Universal curve" of the inelastic mean free path λ as a function of electron kinetic energy.

Line widths and line shapes

Usually, line widths in XPS spectra are of the order 1 eV (FWHM, full width half maximum). They are determined by the natural line width Γ_n, the line width of the x-ray source Γ_s and the energy resolution of the analyzer Γ_a [7]. In good approximation the experimental line width Γ can be considered as

$$\Gamma^2 = \Gamma_n^2 + \Gamma_s^2 + \Gamma_a^2 \qquad \text{with } \Gamma_n \approx \frac{\hbar}{\tau} = \frac{6.6^{-16} \, \text{eV s}}{\tau} \qquad (2.7)$$

where τ is the life-time of the hole state and governed by the intraatomic Auger-effect. It decreases strongly with increasing binding energy. Core-hole elimination by a Coster-Kronig process, i. e. transition of valence electron into the core-hole and simultaneous Auger-emission of an electron of the same valence level, occurs within $\sim 10^{-15}$ s, for example. Only with modern synchrotron sources and electron energy analyzers, experimental resolutions much smaller than the natural line widths became accessible.

The primary spectrum, created by photoexcitation of an electron, is generally of Lorentzian line shape broadened by the life-time of the hole state [3]. However, a perfect Lorentzian line shape is very seldom observed because it is often severely modified by the immediate response of the electron system to the positive photo hole. In insulators there is a tendency of differential charging leading to a symmetric, Gaussian broadening of the peak. In metals, on the other hand, electron-hole pair generation can result in a notably asymmetric Doniach-Sunjic kind of line shape [8]. Moreover, phonon broadening effect must in principle always be accounted for, too. For all practical purposes either a life-time broadened Lorentzian or Doniach-Sunjic line shape is assumed for fit analysis,

convoluted with a Gaussian to account for the limited experimental resolution. This approach usually yields convincing agreement with experimentally observed line shapes (see *Figure 2.4a*).

Inelastic contributions

In practice photoemission lines are superimposed by a background of inelastically scattered secondary electrons that form step-like features at the low binding energy side of the photoemission lines, the so-called "inelastic tail". Contrasting to electrical conductivity that is dominated by low-energy electron-phonon interaction, the inelastic mean free path of high-energy photoelectrons is governed by electron-electron and electron-plasmon scattering that depend on the mean electron density and vary only weakly with the composition of the material. In consequence, the inelastic electron mean free path as a function of the kinetic energy follows a "universal curve" shown in *Figure 2.4b* [9]. In particular, for electron kinetic energies between 100 eV and 1000 eV, characteristic for C $1s$, N $1s$ and O $1s$ PE in the soft X-ray range, the mean free path is in the order of only tens of Ångströms and, thus responsible for the extremely high surface sensitivity of PES. In the analysis of core-level spectra secondary electrons are usually accounted for by inclusion of an integral background as first proposed by Shirley [10].

2.1.4   Instrumentation

The principal design of a PE spectrometer is shown in *Figure 2.5*. It consists of a dedicated photon source with suitable properties, an electron analyzer to determine the kinetic energy of the emitted photoelectrons both enclosed in an ultra-high vacuum (UHV) sample environment.

UHV environment

Though the general effect had been understood already in the early year of the last century [1], the rise of PES as a spectroscopic method started only in the beginning seventies of the last century when UHV technology became accessible. Reason is the high surface sensitivity of the method that requires clean surfaces. As can be shown easily in the framework of the kinetic gas theory, a pressure of 10^{-6} mbar leads to the formation of one monolayer adsorbates within the order of one second, if a stiching coefficient of one is assumed for the impinging gas molecules. For a typical duration of an experiment of 1000 seconds and coverages below 10% of a monolayer it is, thus, necessary to reduce the pressure to about 10^{-10} mbar. Moreover, a sufficient signal to noise ratio also requires, that most of the excited photoelectrons can cover the distance between sample and analyzer without any scattering, which again calls for UHV conditions.
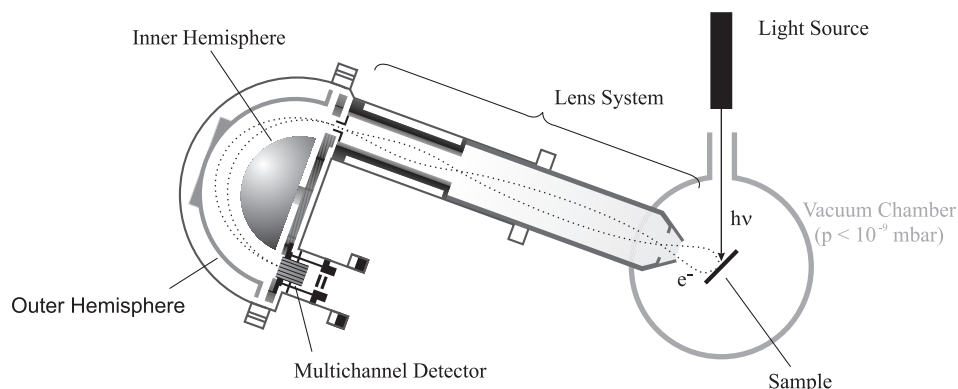
Figure 2.5: Typical layout of a photoelectron spectrometer equipped with a hemispherical electron energy analyzer.

X-ray Source

An X-ray source sufficient for PE experiments must fulfill basically three requirements: The photon energy must be high enough to access the desired electronic states, the intensity must be high enough to generate a detectable yield of photoelectrons and the spectral width must be small to gain a good energy resolution.

There are a couple of different photon sources in use today: gas discharge lamps, X-ray tubes, synchrotron radiation and since short table-top laser systems and (X-ray) free electron lasers. The latter two will have their domain in fs-time-resolved, pump-probe PE experiments where ultra-short and narrow photon pulses are required, but in turn possess a couple of principal disadvantages when it comes to "classical" PE experiments. Gas discharge lamps are restricted to photon energies below 50 eV and only applicable for UPS. Among X-ray sources, only Mg and Al K_α radiation, corresponding to photon energies of 1253.6 eV and 1486.6 eV, respectively, fulfill the requirements of intensity and spectral width.

In contrast to these two laboratory sources synchrotron radiation [11, 12] makes the entire photon energy range from the UV to the hard X-ray region available, but is accessible at only a small number of facilities worldwide. Nonetheless, many studies including the present one rely on the special properties of synchrotron radiation, in particular its tunability and polarization. In addition, only synchrotron beamlines dedicated to spectroscopy routinely achieve superior resolving powers $E/\Delta E$ of 10,000 and more by now, which are necessary to perform high-resolution experiments (cf. 2.1.3). Measurements for the present work were performed at the Russian-German Beamline of the BESSY Synchrotron in Berlin and the beamline D1011 of the MAXlab facility. Technical specifications are given in A.1. The generation of radiation in a synchrotron-fed electron storage ring shall not be dealt with here, since its fundamental principle is commonly known and discussed in details in

the literature, e.g. in references 1.17-24 of [3].

Electron Energy Analyzer

Equally to the photon source the utilized photoelectron energy analyzer must posses a very fine energy discrimination in order to resolve spectral features close to the life-time governed limit of natural line widths (cf. 2.1.3). At present, concentric hemispherical analyzers (CHA) meet these requirements best. They use an electrostatic field to filter electrons of a certain kinetic energy and block electrons of other kinetic energies. The general design is shown in *Figure 2.5*. The main components of such an analyzer are two concentric hemispheres set to an electric potential difference ΔV such that the inner hemisphere is positive and the outer hemisphere negative. Electrons of too low or too high kinetic energy are caught by the inner or outer hemisphere, respectively, ensuring that only electrons with the so-termed pass energy E_{pass} pass the analyzer and reach the detector that is usually based on an electron multilayer like a channeltron or channelplate. In front of the entrance slit usually a lens system is placed that has several functions: collecting the photoelectrons, focusing and electrostatically retarding them to energies of the magnitude of E_{pass}. Pass energies are usually chosen as constant in the energy range between 1 eV and 10 eV, whereby a low voltage is accompanied by high resolution but low counting rate, whereas high voltages result in low resolution but high counting rate. An operation mode with constant pass energy is denoted as constant analyser energy (CAE) mode and employed in XPS almost exclusively. This is due to the fact that a fixed pass energy guarantees constant energy resolution and transmission across the whole energy range, which is indispensable for quantitative XPS analysis. Energy spectra are recorded by ramping the retarding potential of the lens system and plotting the counting rate as a function of kinetic energy, i.e. ramp voltage.

It should be mentioned that for some future experiments in the time-resolved domain the currently developed time-of-flight (ToF) analyzers [13] may gain importance. They allow much higher transmission rates than the present detectors and will be able to measure three dimensions, the energy and the two components k_x and k_y of the emitted photoelectrons simultaneously at a single shot. But in turn they require a photon source that delivers ultra-short photon pulses, perfectly synchronized in time with the detector. Hence their application range will be probably limited to pulsed laser light sources like the currently constructed few X-ray free electron lasers. There, however, they could perform much better than the established CHA.

2.2 X-ray absorption spectroscopy

When photons in the X-ray energy range hit a sample target they can excite electron transitions into unoccupied bound, quasibound or continuum states by being absorbed and transferring their energy onto an electron. In X-ray absorption spectroscopy (XAS) the absorption strength of a sample is measured as a function of incident photon energy. One can thus gain detailed insight into the structure of unoccupied electronic states of a sample [14].

2.2.1 Cross section and oscillator strength

The natural measure for absorption strength is the X-ray absorption cross section σ_{ij} of an atom or molecule which is defined as the electron excitation probability per unit time P_{ij} divided by the incident photon flux Φ.

$$\sigma_{ij} = \frac{P_{ij}}{\Phi} \tag{2.8}$$

For the incident electromagnetic field we can use the vector potential $\boldsymbol{A}$ of a plane wave.

$$\boldsymbol{A} = \boldsymbol{e}\, A_0 \exp(i(\boldsymbol{k}\boldsymbol{r} - \omega t)) \overset{\boldsymbol{k}\boldsymbol{r} \ll 1}{\approx} \boldsymbol{e}\, A_0 \exp(-i\omega t) \tag{2.9}$$

Here it is assumed that the X-ray wavelength is large compared to characteristic atomic dimensions, which is the well-known dipole approximation. The photon flux Φ can now be obtained as the incident energy flux, i.e. the time-averaged amplitude of the Poynting vector, divided by the photon energy

$$\Phi = \frac{\overline{S}}{\hbar\omega} = \frac{\epsilon_0 c E_0^2}{2\hbar\omega} = \frac{\epsilon_0 c A_0^2 \omega^2}{2\hbar\omega} \tag{2.10}$$

where the last identity follows from the Coulomb gauge $\boldsymbol{E} = \partial_t \boldsymbol{A}$. Taking P_{ij} from (2.1) and inserting (2.9) we finally yield

$$\sigma_{ij}(E) = \left(\frac{4\pi\hbar}{m}\right)^2 \frac{\alpha}{\hbar\omega} \left| \langle j \,|\, \boldsymbol{e}\, \hat{\boldsymbol{p}} | \, i \rangle \right|^2 \rho_j(E) \tag{2.11}$$

which is the cross section for an X-ray absorption process causing the electron transition $|i\rangle \to |j\rangle$. At that $\alpha = 1/137$ is the well-known fine-structure constant and $\boldsymbol{e}$ the direction of the electric field vector. Naturally, the sum over all σ_{ij} yields the the total X-ray absorption cross section σ as a function of photon energy.

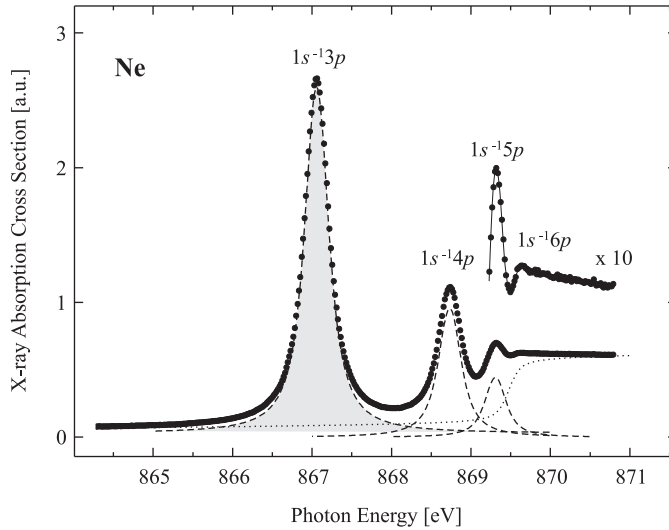$$\sigma(E) = \sum_{i,\,j} \sigma_{ij}(E) \tag{2.12}$$

Figure 2.6: X-ray absorption cross section of Ne in the photon energy range of the $1s^2 \rightarrow 1s^1 np^1$ Rydberg excitations. The dots show the measured spectrum and the thin lines results of a least-squares fit analysis with Gaussian-broadened Lorentzian line shapes. The energy integral under a particular resonance peak gives an independent measure of its intensity, the oscillator strength f, which is indicated here with a grey-shading for the example of the $1s^{-1}3p$ resonance.

It should be noted that though defining the total absorption of the considered atom or molecule at each particular photon energy, the σ_{ij} are, in practice, no suitable measure for the full absorption ascribed to a certain resonant transition $|i\rangle \rightarrow |j\rangle$.

For infinite final state life-times the density $\rho_j(E)$ in (2.11) would make a contribution only at a specific transition energy $E_{ij} = E_j - E_i$ and a discrete line at the resonant photon energy $\hbar\omega_{res} = E_{ij}$ would be observed in the absorption spectrum. In fact, however, ρ_j is always life-time broadened resulting in a finite line width Γ_{ij} of the absorption line. This is illustrated in *Figure 2.6* where the Rydberg series of Ne is shown in a cross section versus energy plot [15]. Consider for instance the $1s^2 \rightarrow 1s^1 3p^1$ resonance peak. Its measured height is given by $\sigma_{1s3p}(E)$, but surely depends on line shape and line width of the peak and therewith on final state life time, experimental resolution etc. It is therefore convenient to define a dimensionless quantity for the intensity of resonance, the oscillator strength f, that is independent on measured line widths and shapes and relates to the X-ray absorption cross sections σ as follows [16]

$$\sigma_{ij} = C \frac{df_{ij}}{dE} \tag{2.13}$$

with $C = 8\pi^2 \alpha\hbar^2/m = 109.8$ Mb eV. The prefactor C is chosen such that the cumulative oscillator strength of all conceivable excitations of a particular core-level is equal to the core-level's electron occupancy, i.e. 2 in case of $1s$ core-levels [16]. In practice, it can of course not exceed $2 - f_{occupied}$ for any given system, where $f_{occupied}$ denotes the cumulative oscillator strength of forbidden transitions into occupied final states. Because the oscillator

strength f is the energy integral of the cross section, it is not affected by any life-time or experimental broadening anymore and simply corresponds to the area below a resonance peak (grey-shaded area in *Figure 2.6*). It is therefore a suitable measure of the intensity of a resonance. Integration of (2.13) yields the following expression for f_{ij}

$$f_{ij} = \frac{2}{m\hbar\omega} \left| \langle j | \, \boldsymbol{e} \, \hat{\boldsymbol{p}} | i \rangle \right|^2 \tag{2.14}$$

One might get a better understanding of the physical meaning of the dipole matrix element in (2.11) and (2.14) when using the position space equivalent of the total momentum operator (cf. [17])

$$\hat{\boldsymbol{p}} = \frac{im(E_j - E_i)}{\hbar} \, \hat{\boldsymbol{r}} \tag{2.15}$$

In good approximation, we can identify $E_{ij} = E_j - E_i$ with $\hbar\omega$, although it should be noted that $\hbar\omega$ is the experimentally determined transition energy, whereas E_j and E_i are eigenvalues of the approximate Hamiltonian. Inserting the expression for $\hat{\boldsymbol{p}}$ in (2.14) finally yields

$$f_{ij} = \frac{2m}{\hbar^2} \, E_{ij} \left| \boldsymbol{e} \, \langle j | \, \hat{\boldsymbol{r}} | i \rangle \right|^2 \tag{2.16}$$

Evidently the oscillator strength f_{ij} of a transition $|i\rangle \rightarrow |j\rangle$ is determined by both spatial overlap and energy separation of the corresponding initial and final state.

2.2.2 Characteristics of X-ray absorption spectra

I will now turn to a discussion of the characteristic features that can be observed in X-ray absorption spectra, including their origin, and how the line shape of these features can be modeled when attempting a curve-fit analysis of experimental data.

Bound, quasibound and continuum state resonances

If we reconsider (2.11) excitation of an atomic core level $|i\rangle$ requires a finite density ρ_j of unoccupied final states accessible with the offered photon energy $h\nu$. In the simplest picture we can assume ρ_j to be a step-like function with a distinct jump from zero to a constant finite value at the ionization potential (IP). Then electron transition $|i\rangle \rightarrow |j\rangle$ can only be excited if the incident photon energy $h\nu$ is equal to or exceeds the minimum energy needed to excite electrons into continuum states above IP. This is illustrated in *Figure 2.7a* where I also show a corresponding absorption spectrum for the neon atom that was calculated within the above, simplified picture [6]. It shows indeed a distinct jump when the photon energy crosses the $1s$ absorption edge, followed by a monotonically descending behavior for higher photon energies. This general spectral shape is part of any measured absorption spectrum and I will refer to it as the atomic part of an absorption
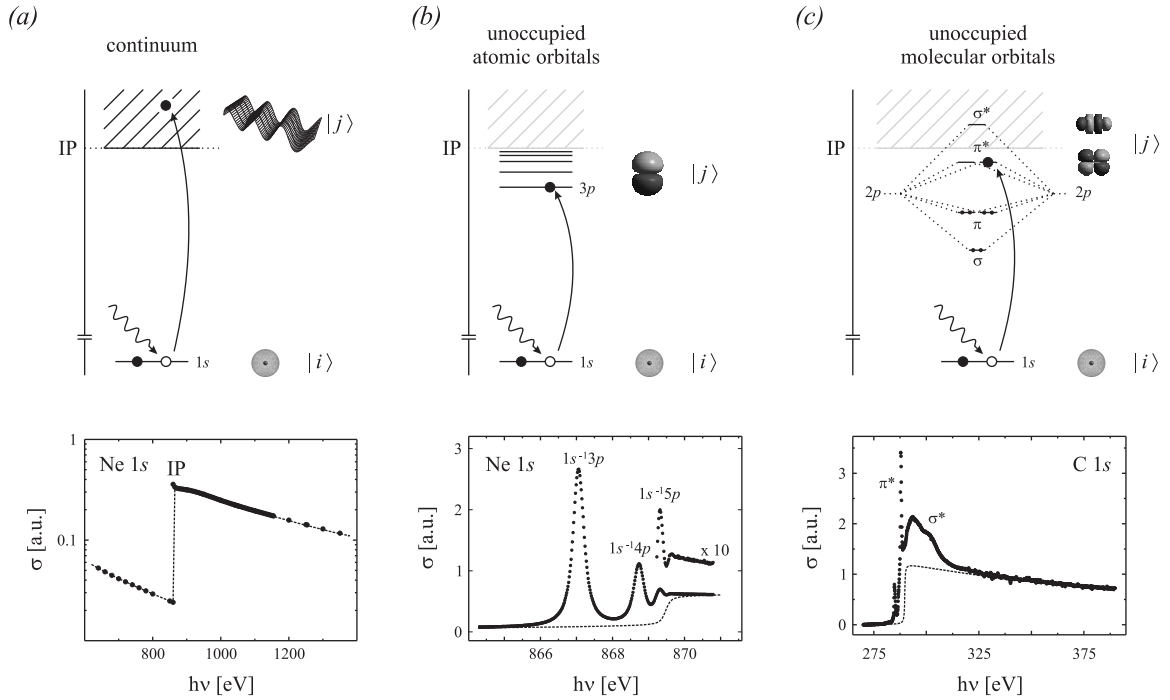
Figure 2.7: (a) Electron transitions into free continuum states above the ionization potential set in each time the energy of the exciting photons crosses an X-ray absorption edge. In XAS spectra those edges are reflected by a step-like feature with a monotonically descending tail. (b) In real atoms additional Rydberg states below the IP are accessible via dipole transitions causing an additional near-edge fine-structure below the continuum step. (c) In molecular systems unoccupied molecular orbitals provide with dipole accessible states in the vicinity of the continuum step. Due to electron-core-hole Coulomb interaction π^* resonances are pulled below the IP in energy and thus feature a very long life-time, whereas σ^* resonances lie above the IP and reflect electron transitions into only quasi-bound states. Both cause a rich fine-structure around the absorption edges, at which the former appear as narrow lines below and the latter as broader structures above the continuum step.

spectrum from now on. Note, that this atomic-like X-ray absorption corresponds to a photoemission process and the final state kinetic energy would be the physical quantity measured in PES.

Two properties of the shown spectrum should be explained more deeply here. First, the monotonically descending behavior of the high-energy tail above the threshold can be understood from the fact, that with increasing kinetic energy the wavelength of the emerging electron wave packet decreases. As a result the overlap between the extremely localized initial state and the final state decreases which is reflected in a decreased excitation cross section. Secondly, the finite cross section below the $1s$ threshold corresponds to the high-energy tails of the lower lying $2s$ and $2p$ absorption steps that interfere the insetting $1s$ absorption in the considered photon energy region.

Modeling ρ_j as a step-like function around the IP is of course a simplification, that cannot be maintained when it comes to comparison with experimental absorption spectra. Considering excitations of Ne $1s$ electrons again, but this time including unoccupied inneratomic states (*Figure 2.7b*), we find a number of possible dipole transitions for photon energies below the ionization threshold, namely the whole $1s^2 \rightarrow 1s^1 np^1$ ($n = 3, 4, \ldots$) Rydberg series. The corresponding resonances add a number of pre-edge peaks to the atomic-like spectrum. Because the final states are bound states below the ionization potential, they possess a rather long life-time before core-hole deexcitation via fluorescence or Auger processes takes place. Hence the corresponding peaks exhibit a rather narrow line width of only a few hundred meV.

Going from the free atom to molecules (*Figure 2.7c*) the atomic valence orbitals are now replaced by molecular orbitals, and instead of the former Rydberg states there are now the unoccupied molecular orbitals that enrich the final state density ρ_j as compared to the simple, atomic-like step-function. These additionally accessible states can cause a very pronounced near-edge fine structure (NEXAFS), that usually spans the energy range between circa -10 eV below and 30-40 eV above an absorption edge. In the case of $1s$ excitations this basically involves p-symmetry derived π^* and σ^* orbitals, because of the dipole selection rules. Since this work is exclusively concerned with organic molecules, composed of first, second and third row atoms, the occurring molecular bonds involve only s and p electrons, which justifies the below restriction to σ^* and π^* orbitals and $1s$ absorption edges. The lowest unoccupied molecular orbitals (LUMOs) are usually of π^* symmetry, whereas the σ^* orbitals appear at higher energies. For the neutral molecule the latter normally lie above the IP while the π^* states are pulled below due to the core-hole effect, i.e. electron-hole Coulomb interaction (cf. 2.1.2).[1]

Because the energy position of π^* resonances falls below the IP for all known $1s$ absorption spectra of low-Z molecules, they appear as discrete sharp peaks below the continuum step. The populated π^* orbitals represent bound states and the final state lifetime is defined by the decay of the core-hole, which primarily takes place via the Auger process, i.e. deexcitation of the excited electron from the π^* state to the K-shell and simultaneous emission of a valence electron. This process takes a relatively long time leading to lifetime widths of about 100 meV. In contrast to π^* resonances σ^* resonances reveal a very spectral shape which is due to their character of quasi-bound states. Although these states lie above the ionization potential they do not decay immediately. It was proposed that they are stabilized by a hump in the potential shape [18]. Therefore, σ^* resonances are often also denoted as shape resonances. However, the need of a potential barrier was controversely discussed, since these resonances can also be explained in a molecular orbital picture. Sheehy *et al.* have shown that in this pictures virtual states above the vacuum

---

[1]The core-hole effects are not necessarily of the same size for continuum and NEXAFS transitions, because in the former case the final state is a hole state more or less screened by conduction or valence electrons, while in NEXAFS the excitation takes place directly into different screening orbitals with the total number N of electrons unchanged!
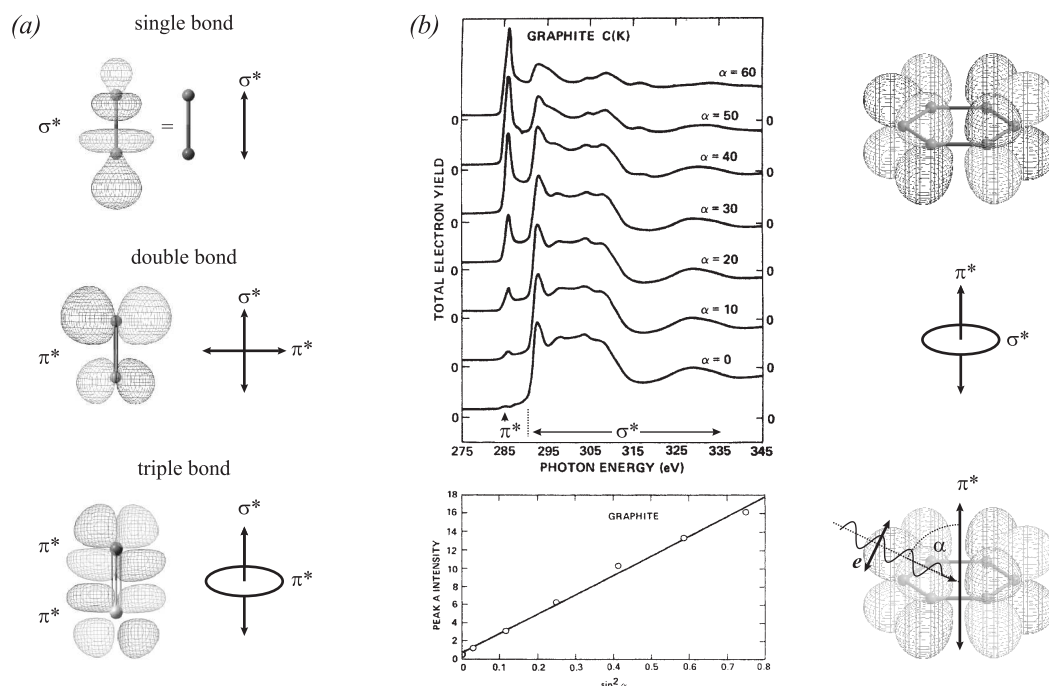
Figure 2.8: (a) Orientation of σ^* and π^* molecular orbitals in single-, double- and triple-bond diatomics. (b) The collective order of π^* and σ^* orbitals in graphite sheets give rise to an angular dependent in the intensities of the corresponding resonances. Quantitative analysis of the π^* peaks reveals the expected $\sin^2$ dependence of the oscillator strength on the relative angle α between the directions of light incidence and molecular orientation. (Spectra taken from [20].)

level exist without applying a potential barrier concept [19]. This leads to a description as a two-step one-electron process, where first the electron is excited to a virtual σ^* molecular orbital, followed by the emission of a photoelectron. Which picture soever is used, all of them yield a very short decay time, resulting in broad spectral widths as compared to that of π^* resonances (cf. *Figure 2.7c*).

Polarization dependence of resonance intensities

Intensities of NEXAFS resonances can show angular dependences in polarization dependent studies because molecular bonds and the associated orbitals are highly directional. This is illustrated in *Figure 2.8a* at the example of simple diatomics. Single bonded molecules are characterized by a σ^* orbital along the molecular axis (vector type), double bonds posses an additional orthogonal π^* orbital (vector type), and triple bonded molecules two orthogonal π^* orbitals (plane type). The angular dependence of $1s$ NEXAFS spectra is determined essentially by the spatial orientation of the final state molecular orbital, i.e. the direction of its maximum orbital amplitude. This becomes immediately apparent from

the position space representation of the oscillator strength f_{ij} given in (2.16)

$$f_{ij} = \frac{2m}{\hbar^2} \, E_{ij} \, |\boldsymbol{e} \, \langle j \, | \, \hat{\boldsymbol{r}} | \, i \rangle|^{\,2}$$

with $\boldsymbol{e}$ the unity vector pointing in the direction of electrical field. In the case of spherically symmetric, $1s$ initial states the matrix element points in the direction of the final state's maximum orbital amplitude. Thus, only the spatial orientation of the final state orbital governs the angular dependence of K-shell spectra. More precisely, the angular dependence of the oscillator strength is given by

$$f_{ij} \propto \sin^2 \alpha \tag{2.17}$$

for a vector final state when α denotes the incidence angle of light with respect to the orbital direction and by

$$f_{ij} \propto \cos^2 \alpha \tag{2.18}$$

for a plane-type final state where α is the angle between the orbital plane and the Poynting vector of the incident light [14].

This polarization dependence of resonance intensities can be observed in systems that exhibit a collective orientation of molecular orbitals, like for instance graphite. As depicted in *Figure 2.8b* the individual carbon layers of graphite posses delocalized π^* states pointing out of the atomic plane and in-plane σ^* orbitals. The shown series of NEXAFS spectra taken at increasing angles α of the incident light with respect to the π^* direction unambiguously demonstrates a polarization dependence of the π^* and σ^* resonance intensities (top panel) and quantitative analysis of the π^* peak revealed the predicted $\sin^2 \alpha$ dependence.

In contrast, in systems where the individual molecular orbitals are not collectively aligned, the discussed angular dependence of resonance intensities cannot be observed because all polarization dependent effects are averaged out. Compared to the maximum possible oscillator strength f_{ij}^{max} found when the final state orbitals are all perfectly aligned parallel to $\boldsymbol{e}$ the measured average oscillator strength f_{ij} will then appear lowered.

$$f_{ij} = f_{ij}^{max} \int\limits_{0}^{\pi/2} \sin^2 \alpha \; d\alpha = \frac{\pi}{4} \, f_{ij}^{max} \tag{2.19}$$

The "building blocks" approach for large molecules

Interpretation of NEXAFS spectra of larger molecules, i.e. the assignment of the observed resonances to particular molecular final states, is usually not straight-forward. Surely, molecular orbital (MO) calculations can help to unravel near-edge fine structures in
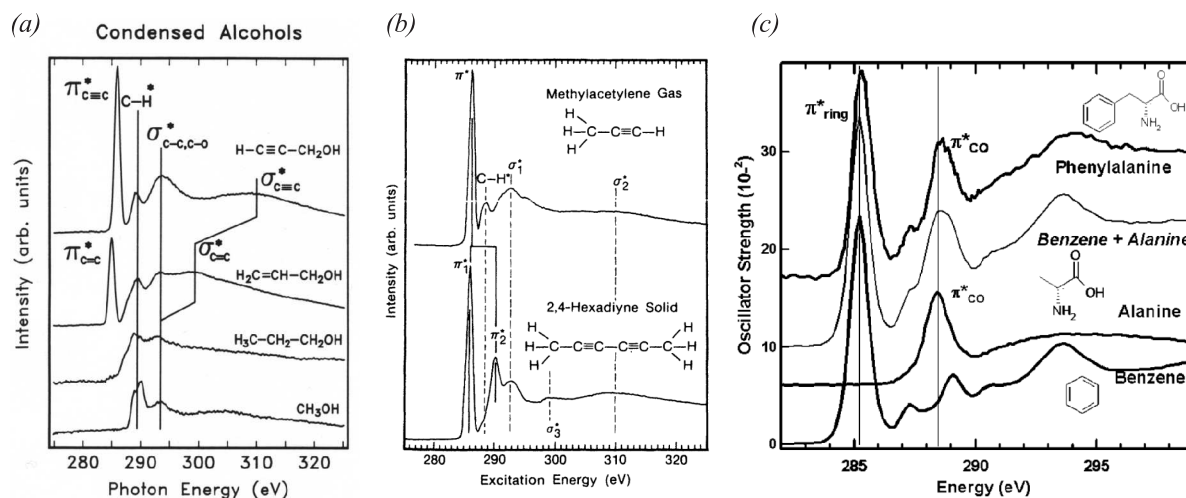
Figure 2.9: (a) Using the "building blocks" approach the spectrum of propargyl alcohol (HC≡C-CH₂OH) can be explained as a combination of features of individual bonds comprised in the molecule by its successive building-up starting from the simplest alcohol methanol (CH₃OH) [21]. (b) The simple "building blocks" approach comes to its limitations where effects of electron conjugation become important. Here this is demonstrated at the exchange splitting of the C 1s→ π* resonance of the CH₃-C≡C-H molecule when assembling two of them to the CH₃-C≡C-C≡C-CH₃ molecule which features a higher symmetry [22]. (c) Effects of electron conjugations can often be accounted for by including them into the building blocks. Here the example of a complex amino acid is shown the NEXAFS spectrum of which can be successfully decomposed by analyzing the spectra of the more simple benzene and alanine molecule separately [23].

molecule XAS spectra. However, reliable MO calculations require to calculate eigenfunctions for the whole electron system. Restriction to only valence electrons is not possible. This results in large efforts even for comparatively small molecules.

Therefore, an alternative, empirical approach, the "building blocks" method, has been established which in many cases yields satisfactory results. It relies on the assumption, that a molecule can be seen as an assembly of smaller molecules, in the extreme case only diatomic molecules, that are coupled to each other by rather weak forces so that the effects of these interactions on the electronic structure of the "building blocks" may be neglected. For small molecules with only few bonds the resonances can often be directly linked to the π* and σ* orbitals in the molecule. Based on that, one can try to reconstruct spectra and, thus, the electronic structure of larger molecules using suitable molecules as building blocks. This is demonstrated in *Figure 2.9a* at the example of alcohols with increasing complexity. Starting from the simple methanol molecule all resonances of a propargyl alcohol (HC≡C-CH₂OH) NEXAFS spectrum could be assigned by successive structural assembly with suitable building blocks.

Naturally, this approach must reach its limitations when delocalized bonds have to be considered. Spectra of conjugated systems, i.e. systems were bond-bond interactions

become significant, do no longer resemble the spectral sum of their constituents because of the strong interactions between these building blocks. This affects both σ and π^* bond-bond interactions and in particular aromatic rings reveal both types of interactions. Also, when building blocks join to a molecule with enhanced or decreased symmetry some molecular orbitals may respectively split or degenerate due to the Pauli principle, resulting in very different NEXAFS spectra. This can be seen in *Figure 2.9a* where the splitting of a C $1s \rightarrow \pi^*$ resonance is shown when two CH_3-C≡C-H building blocks are assembled to a CH_3-C≡C-C≡C-CH_3 molecule which has a higher symmetry (D_2).

However, the discussed limitations of the building blocks approach can often be overcome by appropriate choice of the building blocks. Decomposing large polyfunctional molecules into weakly interacting functional subgroups, that include possible effects of conjugation from the beginning, can enable to treat even spectra of huge molecules still as a superposition of the spectral characteristics of the respective subgroups. In that manner, the building blocks method can be satisfactorily applied also to macromolecules like proteins and polymers with a large number of delocalized bonds. One example is given in *Figure 2.9c*. There the NEXAFS spectrum of phenylalanine, an amino acid with highly conjugated aromatic and carboxyl groups, is successfully decomposed by assembly from two individual subspectra using a benzene and a alanine building block [23].

Line shapes and curve fitting

A quantitative discussion of XAS spectra in the framework of a curve fit analysis requires modeling of the individual spectral parts with mathematical components of suitable line shape. For spectra of low-Z molecules, as they are relevant for the present work, this namely involves the π^* and σ^* resonance peaks as well as the continuum steps of $1s$ X-ray absorption edges. In this section, the line shapes of these spectral features shall be considered in more detail.

The intrinsic line shape encountering in spectroscopic studies is the Lorentzian. If the experimental resolution is small against natural, life-time related line widths it will describe a measured profile well. If, on the other hand, the experimental resolution given by the spectrometer performance dominates a Gaussian line shape will be observed for the peaks. However, both Gaussian and Lorentzian cannot model a peak convincingly if life-time and experimental broadening are of comparable size. In this case, the Lorentzian describing the life-time broadening must be convoluted with a Gaussian to account for the limited experimental resolution. This yields a so-called Voigt profile. Thus, in practice, it can be easily estimated whether a simple Lorentzian or Gaussian is sufficient to model the line shape of an isolated peak, or a Voigt function is needed, by comparing its width with the spectrometer resolution.

Though working well for π^* resonances, in many cases neither of the three profiles can satisfactorily describe σ^* structures which often exhibit a pronounced asymmetry. This is
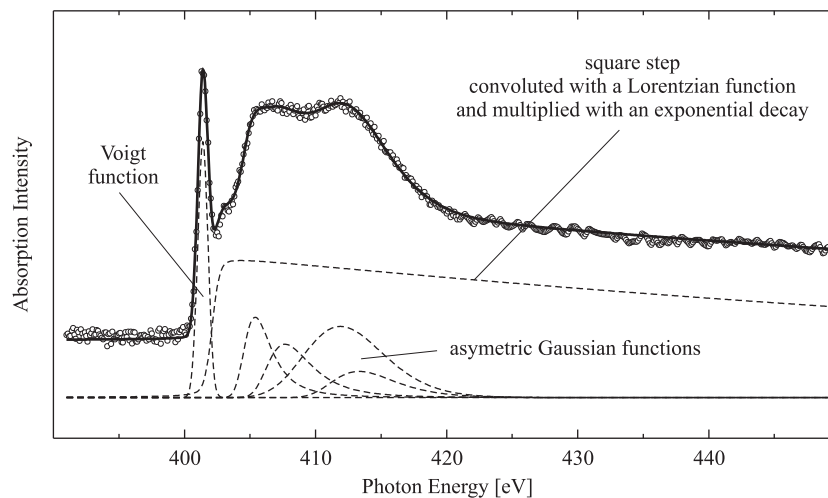
Figure 2.10: Curve fitting of an N 1s NEXAFS spectrum taken from a protein physisorbed to a SiO$_x$/Si substrate. Utilization of the in the text discussed line profiles for the π* and σ* resonances and the continuum step yields very good agreement with the experimental spectral shape over the entire probed photon energy range.

possibly related to intramolecular vibrations changing the bond lengths which could affect both energy position and life-time of the shape resonances of the quasibound σ* states [24]. Outka and Stöhr proposed the use of Lorentzian or Gaussian functions modified in such a way that their widths depend linearly on energy, i.e. $\Gamma = E \times a + b$ [25], which often yields excellent results.

It should be remembered, that the general appearance of the continuum steps is due to insetting transitions into a continuum of free states. For the isolated molecule it therefore falls at the IP. However, its position might be changed or there might be even multiple continuum steps for a single threshold as a consequence of many different factors. If we consider for example molecules adsorbed to a conducting substrate there might be a red-shift of the step because of the continuum of states between E_F and the IP offered by the metal conduction band. It is difficult to examine the shape and position of a continuum step experimentally, because they are almost always superimposed by other spectral features. However, already several eV above a threshold the continuum absorption always shows similar, monotonically descending progression irregardless of the concrete position and shape of the step itself.

The most common approach to mathematically model the step is in the form of a square step (also denoted as Heaviside function Θ) at the energy position P convoluted with Lorentzian or Gaussian, depending on whether its shape is assumed to be more life-time or more resolution-determined. This corresponds to a simple integral over a Lorentzian or Gaussian and thus yields either an arctan function or an error function. The width Γ of the step can be estimated from either the core-hole life time or the experimental resolution again. In order to account for the descending progression further above the threshold,

which is due to decreasing overlap between initial and final state (see above), the step function I_{step} can be additionally multiplied with an exponential decay [25]

$$I_{step}^{exp} = I_{step} \times \exp\left[-d(E - P - \Gamma)\,\Theta(E - P - \Gamma)\right] \qquad (2.20)$$

In most cases, very good agreement with experimentally observed spectral shapes can be achieved with the discussed mathematical modeling of π^*, σ^* and continuum step profiles in XAS spectra. One example for this is the fitting of a protein spectrum depicted in Figure 2.10.

2.2.3 Detection of X-ray absorption signals

Naturally, precondition to measure X-ray absorption as a function of photon energy is a monochromatic light source with continuously tunable photon energy and sufficiently high intensity over a wide energy range. This requirement can only be met by the use of synchrotron radiation.

There are two different conceivable methods to determine the strength of X-ray absorption by a sample. The most direct way is to measure the transmittance and reflectivity of a sample in the photon energy region of interest. This, however, would require exceedingly high experimental efforts concerning, for instance, detectors and is therefore in practice usually not applied. The other way is to detect an X-ray absorption process indirectly by measuring a yield signal generated during decay of the excited core-hole. This can either involve charge-neutral decay via fluorescence or ionizing decay via Auger processes. Depending on which of both processes is aimed for the mode of detection is either called fluorescence or electron yield mode.

Each of them comes with intrinsic advantages and disadvantages. Fluorescence yield detection is a photon-in-photon-out technique and hence bulk-sensitive. The photons generated during the decay can penetrate through the sample over several hundred nm without any interaction. One the other hand, the probability of fluorescent decay is only few percent for low-Z elements [26] and the generated yield signals are disproportionately low when related to the photon flux input. Electron yield detection, on the other hand, will give a by far higher signal. Moreover, in the simplest experimental approach it is extraordinarily easy realized with no need for any dedicated electron detector. These advantages, however, are achieved on the cost of the now lost bulk sensitivity. Because of intense electron-electron scattering the mean escape depth of the generated Auger electrons, determining the probing depth, is only in the order of few tens of Å (cf. 2.1.3). But in the particular case of surface adsorbates, like they are considered in the presented work, this can even be advantageous, because the signal(surface)-to-background(substrate) ratio becomes much enhanced (*Figure 2.11a*). For all these merits the electron yield detection mode was always chosen in the here presented studies for recording XAS spectra. It shall therefore be considered in some more details here.

In practice, one can distinguish three different types of electron yield detection modes characterized by which fraction of the emitted electrons is measured (*Figure 2.11b*). The most specific of them is the Auger electron yield (AEY) mode where on constrains detection to a small electron kinetic energy window around a particular Auger line. In this way one can pronounce the signal of a certain elemental species and partly suppress other contributions. Because only primary, unscattered electrons contribute to the Auger line, this mode is highly surface sensitive. Experimentally, detection of an only narrow kinetic energy range can be accomplished with the help of an electron energy analyzer like it is used in photoemission spectroscopy (cf. 2.1.4).

The second mode is denoted as partial electron yield (PEY) mode. Here the spectrum of emitted electrons is cut off at a certain kinetic energy and only electrons lying above are counted. By varying the cut-off energy one can tune the probing depth within certain boundaries because more and more multiply scattered low-energy electrons from deeper layers will be blocked, in particular those in the low-energy inelastic tail. Only contributions above the cut-off, be it Auger, PE or inelastically scattered electrons are detected. PEY detection can be realized using an electron detector, e.g. a microchannel plate detector, with an upstream electrostatic retarding field. The kinetic energy cut-off is then simply given by the applied retarding voltage.

The simplest detection mode is the total electron yield (TEY) detection where all electrons emitted from the X-ray irradiation sample are detected. It essentially corresponds to the PEY mode with the retarding potential set to zero. Accordingly, both detection modes can be used with the same experimental setup. However, another much simpler setup without any electron detector becomes possible, too, which is the main advantage of the TEY mode. The general scheme of this setup is shown in *Figure 2.11c*. If a sample is mounted such that it is electrically isolated from the experimental chamber and has its own earthing, a drain current into the sample will be measured when the sample is irradiated by X-rays. This drain current exactly corresponds to the total electron flux emitted from the sample, i.e. the desired TEY signal. Naturally, the TEY mode does not offer any possibility of chemical selectivity or tunable probing depth, but comprises the entire spectrum of electrons generated during the decay of X-ray excited core-holes, i.e. Auger, photoemitted and secondary electrons.

The signal intensities J measured in the TEY detection mode of X-ray absorption are dependent on a number of parameters which can be summarized in the following phenomenological equation

$$J = M(E_{kin}) \times Y \times \rho \times \eta \times \sigma(h\nu) \times \Phi(h\nu) \qquad (2.21)$$

Therein, Φ denotes the incoming photon flux, σ is the energy dependent total X-ray absorption cross section, η gives the probability that the induced core-hole decays via an ionization process and is very close to unity for all light elements with $Z \leq 10$ [26], ρ denotes the number of accessible absorption centers per irradiated sample area unit, Y characterizes the yield efficiency, i.e. the probability that an autoionization event can
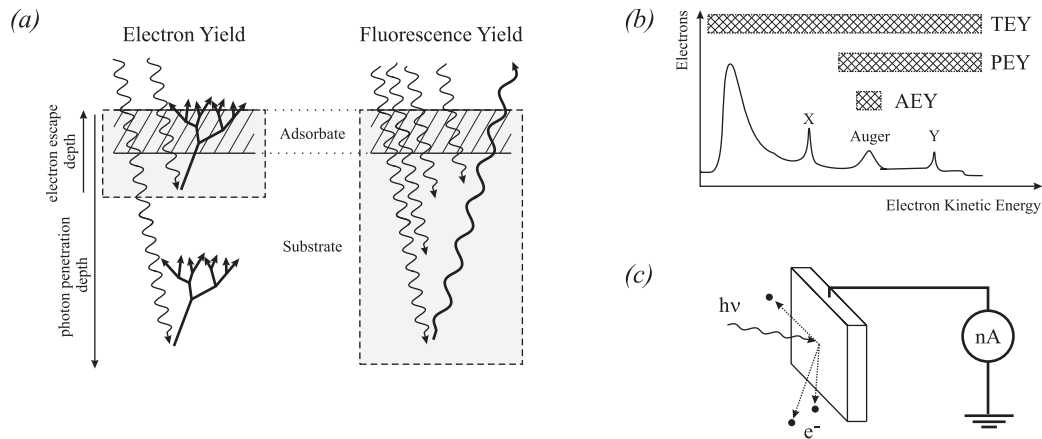
Figure 2.11: *(a) While for electron yield detection the probing depth is limited to few nm because of the low electron escape depth, the fluorescence yield is basically a bulk signal probing the whole photon penetration depth down to several hundreds of nm, however at considerably lower signal intensities in the case of light elements. (b) Comparison of the different electron kinetic energy ranges probed in the Auger, partial and total electron yield detection mode. (c) Principal design of a TEY spectrometer.*

contribute to the detected signal. That can involve for example effects like the limited electron escape depth and if necessary also detector properties like the acceptance angle, etc. Finally, the factor M characterizes multiplication effects that are related to the generation of secondary electrons due to inelastic scattering of the primary electrons. Generally, M must be assumed to be dependent on the kinetic energy E_{kin} of the primary electron. However, for the energy range accessible with soft X-rays, which is relevant for the present study, there arose some evidence that the efficiency of electron multiplication is in good approximation energy-independent [27]. Therefore, for a given sample and experimental setup J probably depends in good approximation only on the incident photon flux and the X-ray absorption cross section of the sample.

3 Monitoring and tuning structural properties in DNA microarrays: A look into self-assembled structures of biomolecules on the mesoscopic scale

3.1 Introduction

About 25 years ago Nuzzo *et al.* published the first report on monolayers assemblies of alkanethiols on nobel metal surfaces [28]. They found that alkanethiols are capable to form highly ordered monolayers on zerovalent gold surfaces via self-assembly. At that, the strong sulfur-gold interaction guaranties specific anchoring of the thiol group (-SH) functionalized ends of the alkanethiols to the clean gold surface, whereas weaker intermolecular forces cause the spontaneous self-organization of the alkanethiol films [29]. Since that first report on self-assembled monolayers (SAMs) many studies have been focused on the understanding of the properties and detailed mechanisms underlying the structure formation of these organic layers. In particular, the ability to control the properties of a surface by coating it with a SAM has motivated a high research interest in SAMs [29, 30, 31, 32].

Nowadays, the increasing feasibility to anchor various kinds of biomolecules, e.g. proteins oder DNA-strands, to gold surfaces via alkanethiol linkers allows to gather highly specific functionality on small substrate areas. These systems are widely known under the popular term "biochips". In particular, tethering of thiol-modified DNA probes on gold surfaces has found wide application ranging from DNA microarrays via DNA-based protein sensors up to first attempts in DNA-based nanoelectronics [33, 34, 35, 36, 37, 38], at which DNA microarrays have already evolved into a standard tool in modern life sciences [39, 40].

The general structure of a DNA microarray is schematically shown in *Figure 3.1*. It consists of more or less densely packed thiolized single-strand DNA molecules, so-called oligonucleotides, which are surface-anchored via their thiol end group, while free surface regions between the DNA probes are backfilled with an alkanethiol SAM. The probe oligonucleotids are each designed in their base-pair sequence. Because the base-pair sequence of the
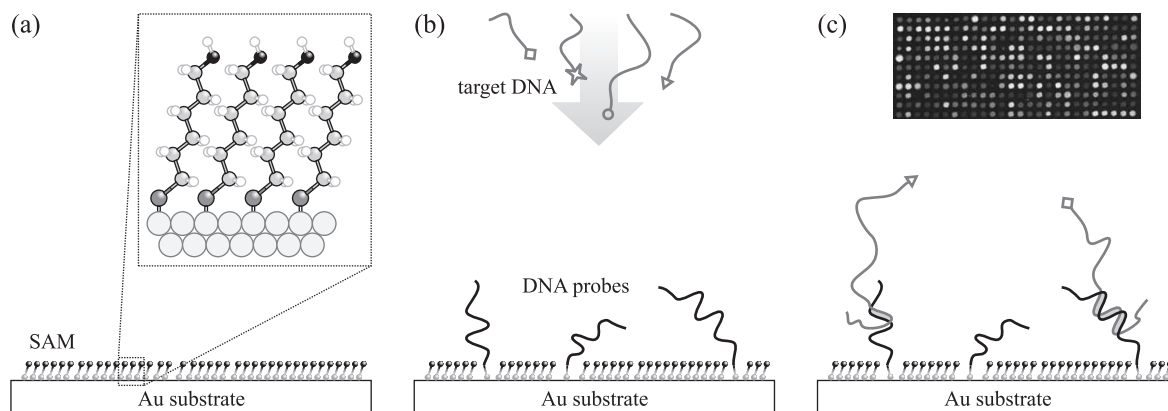
Figure 3.1: DNA microarrays are mixed DNA-alkanethiol layers (middle). Thiolated single-strand HS-DNA probes are adsorbed to a gold substrate by making use of the strong sulfur interaction and vacant surface regions are backfilled with a alkanethiol self-assembled monolayer (SAM, left). When exposed to fluorescent-labeled target DNA, probe strands with a complementary base-pair sequence can hybridize with the respective target strands, which can be later on detected in fluorescence measurements.

two strands in double-stand DNA has to be always complementary, the sequence-designed DNA probes hybridize with the target DNA only when the latter contains a respective complementary base-pair sequence. These hybridized DNA double-strands can be later on detected. Thus, by purposefully arranging oligonucleotides in a microarray with a multitude of characteristic base-pair sequences, one can build sensors which probe entire genoms. The function of the SAM backfill is twofold: First, oligonucleotides end-specifically functionalized with thiol groups tend to interact with the gold surface not exclusively via their anchoring sulfur-gold bond, but to establish also non-specific interactions between their nucleobases and the metal surface [41, 42, 43, 44, 45, 46, 47, 48, 49]. To avoid such unwanted adsorption of DNA bases, the functionalized gold surface must be passivated. This is usually done by exposure to the alkanethiol mercaptohexanol (MCH, HS-$(CH_2)_6$-OH) which forms a passivating self-assembled monolayer in the free surface regions. In addition, deposition of MCH is expected to improve the accessibility of target DNA to the probe DNA during hybridization.

Though in wide use, many aspects of DNA microarrays can be still considered as undiscovered terrain. For instance, probe density and layer quality are known to be decisive factors for the control of the hybridization efficiency and kinetics, and therewith the performance of a DNA microarray [50, 51, 52, 53, 54, 55]. However, some of the underlying questions are still not satisfactorily clarified: (i) How can the density of DNA probes in the post-deposited MCH SAMs be controlled and increased? (ii) How should the sample preparation be set up in order to achieve the highest-possible structural quality? And (iii) is there an interplay between MCH molecules and the thiol-modified oligonucleotids during the layer formation?

In this chapter, these questions shall be addressed using high-resolution XPS which can provide qualitative as well as quantitative information on self-assembled alkanethiol monolayers containing DNA [50, 56, 57, 58, 59]. Compared to other sample characterization techniques like scanning tunneling microscopy (STM), which has delivered much of today's knowledge about structural properties of SAMs [60], XPS comes along with several advantages as regards investigation of above raised issues. By nature, STM works on a local scale monitoring a small section of maximum tens by tens nanometers at a time. However, reliable determination of the mean DNA probe density in the layer requires averaging over a sufficiently large sample area, which renders STM inefficient for this task. In XPS, on the other hand, one covers a mesoscopic region of typically $80 \times 20 \,\mu\text{m}^2$ at a time [15], given by the beam spot size at the sample position. In addition, XPS provides with element specific information, enabling to separately and in more details characterize the different parts in the oligonucleotide-MCH layer, as for instance the sulfur-gold interface. Moreover, it does not require special sample pretreatment like metal-coating which could possibly affect the sample structure.

On the other hand, interpretation of XPS spectra obtained from such complex biological samples is often not straight-forward. Therefore, in the following two sections of this chapter both constituents of DNA microarrays, the MCH self-assembled monolayer and the DNA probes are XPS characterized separately, in order to ease the subsequent spectroscopic investigation of the mixed oligonucleotide-MCH layers. In the next section, it is discussed to which extend the DNA probe surface density in post-deposited MCH SAMs can be controlled by varying the ionic strength of the DNA probe immobilization buffer. High structural quality for alkanethiol SAMs and for thiol-tethered DNA probe assemblies for themselves is usually accomplished by conflicting preparation protocols. In the fifth section, it is studied which of both protocols provides with the better structural quality in hybrid DNA-MCH films. In particular, the properties of films prepared by post deposition of MCH from ethanolic and aqueous solution, respectively, are compared. Finally, in the sixth section, the interplay between the MCH and the oligonucleotids during the film formation is investigated. More precisely, the relative time-scales for surface absorption of MCH and thiol-modified DNA molecules are analyzed, leading to the indication that both steps, DNA-anchoring and MCH backfill should be realized subsequently.

3.2 XPS characterization of mercaptohexanol self-assembled monolayers

Let me first turn to the question of how XPS can help to characterize the structure and quality of pristine MCH self-assembled monolayers. This involves both the SAM as a whole as well as its individual components, the MCH molecules. To this end, pristine MCH self-assembled monolayers, prepared according to the protocol given in A.2.1, were investigated by means of XPS at the Russian-German beamline (cf. A.1.1).
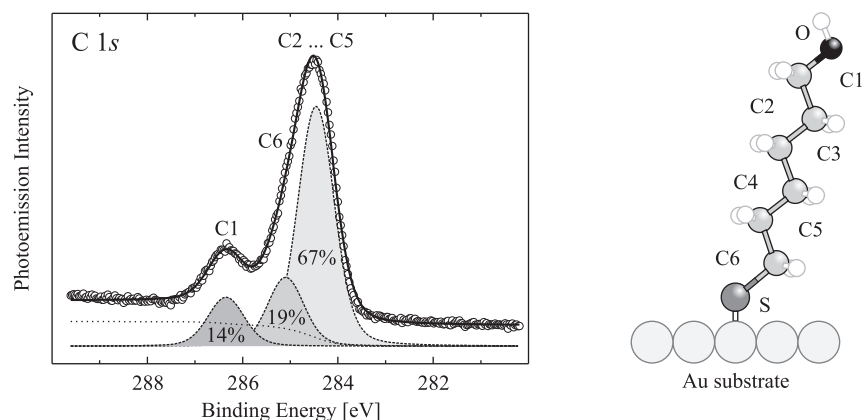
Figure 3.2: C 1s photoemission spectrum of an MCH self-assembled monolayer together with results of a least-squares fit analysis. The found intensity of the different components agrees well with the stoichiometry of the MCH molecule.

Beside a large Au $4f$ signal originating from the underlying gold film, overview spectra taken at 600 eV photon energy (not shown), feature three distinct peaks at circa 162 eV, 285 eV, and 532 eV BE that can be assigned to the S $2p$, C $1s$ and O $1s$ PE signals of the MCH layer, respectively. Because core-level BEs sensitively depend on the chemical binding (see 2.1.2), the substructures of the individual element spectra contain detailed information on the chemical nature of these elements within the MCH molecule. Therefore, they were acquired separately with a high density of data points. Moreover, all three spectra were recorded in the same kinetic energy range–that is, for the same escape depth of outcoming photoelectrons (see 2.1.3)–by using a photon energy of $h\nu = 250$ eV, 370 eV and 620 eV for the measurement of the S $2p$, the C $1s$ and the O $1s$ spectrum, respectively. The spectra were aligned on the BE scale using the well-known position of the Au $4f_{7/2}$ peak (84.0 eV BE).

The C $1s$ PE spectrum should carry information on the chemistry of the single MCH molecules, because the carbon atoms are linked to all other atoms within the molecules, whereas the S $2p$ spectrum should mainly grant insight into the interaction between the thiol groups and the gold surface. The O $1s$ core-level XPS spectrum should show only one singlet component, because oxygen is found in only one chemical environment, namely the hydroxyl group, and the latter is not expected to interact with the gold surface. Indeed, this assumption is confirmed by our experimental data [61]. Because, the O $1s$ spectrum does not help to answer the above risen questions, its discussion will be skipped here. Instead I will concentrate on the C $1s$ and S $2p$ PE.

The C $1s$ spectrum is shown in *Figure 3.2* and reveals two maxima, a main feature at 284.5 eV and a second feature at a binding energy of about 286.6 eV. In addition, the line shape of the main feature appears to be broadened at the high energy side. Indeed, a fit analysis of the recorded spectrum, the result of which is also included in *Figure 3.2*, confirms that at least three individual singlet components are necessary to reproduce the

observed spectral shape, assuming that all components reveal the same spectral width. The same result has also been obtained in previous PE studies of alkanethiol monolayers [62]. One can, therefore, assume that carbon atoms are found in at least three different chemical states within the MCH molecules. Following the initial state interpretation of chemical shifts in 2.1.2, the detected deviation in the C $1s$ BEs of the three PE components points to differently electronegative binding partners of the probed carbon atoms in each chemical state. Looking at its stoichiometry, also shown in *Figure 3.2*, the MCH molecule indeed exhibits three differently bound type of carbon atoms. Atoms C2 to C5 are of entirely hydrocarbonic nature, whereas atoms C1 and C6 experience the influence of the neighboring oxygen and sulfur atom, respectively.

Due to the high electronegativity of oxygen and the expected large charge transfer from C to O, the C $1s$ PE component with the highest binding energy can be assigned to atom C1 with its adjacent hydroxyl group. The main PE line around 284.5 eV BE shows a two-component substructure which has been observed in previous high-resolution measurements of alkanethiolate films, too [63]. Qualitative comparison of the intensities of the two subcomponents at 284.5 eV and 285.0 eV already suggests that the latter subcomponent originates from C6 type atoms, whereas the most intense 284.5 eV component is related to PE from purely hydrocarbonic atoms, i.e. C2 to C5, the number of which is four times that of C6 type atoms according to the molecule stoichiometry. Beyond that, there are two more reasons for the above assignment of the 285.0 eV peak to C6 type atoms: (i) Considering initial state arguments a shift to higher BE with respect to the hydrocarbon signal is expected by the reason of the slightly higher Pauling electronegativity of sulfur as compared to carbon [64, 65]. (ii) Measurements and calculations done for C-C and C-S bound carbon atoms in polymers indicate a shift of the latter by circa 0.5 eV to higher BE, too [66].

The relative occurrence of C1, C2..C5, and C6 carbon atoms within the prepared SAM can be directly determined from the intensities of the corresponding C $1s$ PE component and compared to numbers calculated from the stoichiometry of the MCH molecule. Assuming fully intact MCH molecules a PE intensity ratio of 1 : 1 : 4 or 16.7% : 16.7% : 66.6% between the 286.6 eV, the 285.0 eV and the 284.5 eV component is theoretically predicted, which is in pretty good agreement to the measured ratio of 14% : 19% : 67%. This proves wide integrity of the single MCH molecules inside the layer.

However, the desired excellent sample quality requires not only integrity of the single MCH molecules, but additionally their well-defined anchoring to the gold surface via the thiol group, leading to high structural order in the form of a SAM. It is therefore necessary to spectroscopically characterize the sulfur-gold interface, too. As the mentioned above, the S $2p$ PE spectrum appears to be predestined for this purpose. It is shown in *Figure 3.3* together with results of a least-squares fit analysis. The fit analysis was carried out, assuming a spin-orbit split of 1.1 eV between the $2p_{3/2}$ and the $2p_{1/2}$ fine-structure level. The PE intensity ratio of the two signals was set to 2 : 1, according to their respective m_j degeneracy. These values are valid for atomic sulfur [67] and shall represent a good
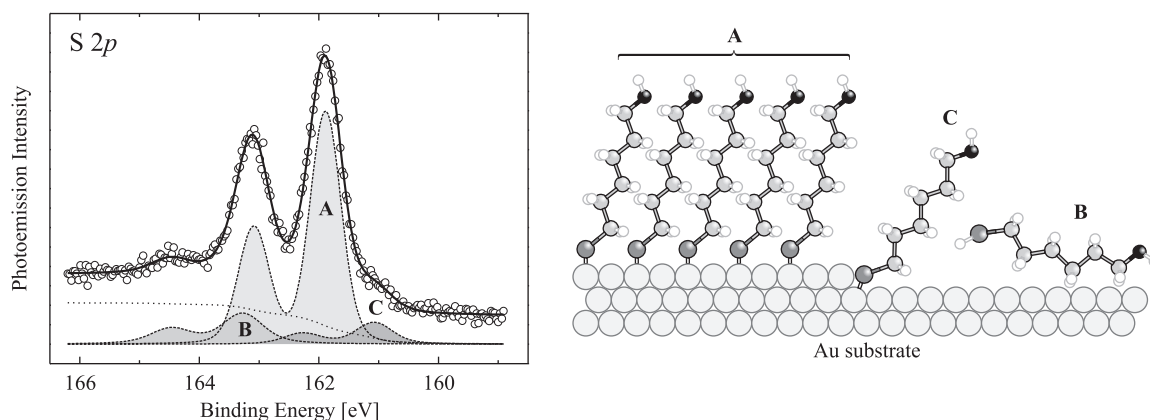
*Figure 3.3: (S 2p PE spectrum of an MCH SAM. Least-squares fit analysis reveals three under-lying components with the $2p_{3/2}$ at 161.9 eV (**A**), 163.2 eV (**B**) and 161.1 eV (**C**). The intense component **A** reflects molecules well-ordered in the SAM, **C** is related to molecules adsorbed at kinks, steps and hollow sites, whereas **B** derives from unbound molecules.*

approximation for core levels of bound sulfur, too. As a result the fit analysis of the S $2p$ spectrum reveals a structure of three distinct $2p$ doublets: A dominant doublet with the $2p_{3/2}$ peak at a BE of 161.9 eV (denoted as **A**), a second doublet (**B**) shifted to higher BE ($2p_{3/2}$ peak at 163.2 eV) and a third doublet (**C**) which has the lowest intensity and is shifted to lower BE ($2p_{3/2}$ peak at 161.1 eV).

In agreement with experimental and theoretical data for other thiolates on gold surfaces, the S $2p$ PE doublets **A** and **B** at 161.9 eV and 163.2 eV can be assigned to bound and unbound sulfur groups, respectively [62, 68, 69, 70, 71]. Note, that the binding energy of a MCH molecule attached to the gold surface via the sulfur atom is expected to be lower than that of an unbound molecule, because the formation of a "covalent" S-Au bond is accompanied with charge transfer from the gold film to the sulfur atom. Following this line of argumentation, the fact that the third doublet **C** is shifted to even lower BE than that of the bound thiol group, suggests a stronger interaction or higher coordination between that sulfur species and the gold substrate than for normal coordinated thiol groups. This can either stem from thiol groups adsorbed on steps, kinks and hollow sites, or from a reconstruction of the gold surface [72, 73, 74].

The relative spectral weights of the three doublets **A**, **B**, and **C** amount to 76%, 15%, 9%. This indicates that after 120 min of assembly and subsequent rinsing with ethanol, 85% of the MCH molecules deposited onto the gold layer are bound to the surface via their thiol groups, which can be calculated as the sum of the relative weights of the contributions A and C. Only 15% of the sulfur atoms remain unbound, that is, they do not self-assemble into an ordered monolayer. One can, therefore, conclude that, beside wide integrity of the single MCH molecules, the researched SAMs feature high structural order, both together confirming excellent sample quality. In general, core-level PES appears to be well-suited for characterization of alkanethiol SAMs, at which in particular the S $2p$ spectrum carries

valuable information on the structural order and, therewith, the SAM quality.

3.3   Core-level electronic structure of DNA

Single-stranded DNA (ssDNA) probes are the second constituent of DNA microarrays. In this section, the core-level electronic structure of DNA will be studied by means of XPS. More precisely, an assignment of the spectroscopic features at all relevant core-levels, i.e. the C, N, and O $1s$ and the P $2p$ core-level, will be given. This will allow to later on distinguish the characteristic imprints of on the one hand DNA probes and on the other hand the alkanethiol SAM in XPS spectra of DNA microarrays. In order to increase the signal-to-noise ratio, the measurements were done on large molecules of genomic DNA nonspecifically adsorbed onto a gold surface according to the protocol given in A.2.2. In doing so, a much higher DNA density is achieved, though, at the cost of any structural order or specific binding to the gold surface, when compared to the case of thiol-bound DNA probes. However, as discussed for the alkanethiol SAMs (3.2) that is not to notably affect to DNA-relevant core levels, but only the S $2p$ core level of the thiol-linkers. Therefore, one can expect to obtain all desired spectroscopic information on DNA probes from these samples, but at considerably higher XPS signal intensities.

The general chemical structure of DNA is sketched in *Figure 3.4a*. DNA consists of a chain of phosphate-sugar monomers, the DNA backbone, at which each monomer binds one of the four nucleobases adenine (A), thymine (T), guanine (G), or cytosine (C), building a so-called nucleotide. All genetic information carried by the DNA molecule is encoded in the sequence in which the nucleic-acid are incorporated in the strand. The well-known double-helical structure of DNA [75, 76, 77] shows up when two single-strands mate to a double-strand structure (dsDNA). Then, the two sugar-phosphate backbones built the outer part of the molecule, surrounding a stack of base pairs. Due to spatial requirements base pairs can only been established between complementary nucleobases, i.e. A and T or G and C basepairs, hold together by either two or three hydrogen bonds. In consequence, the two strands in dsDNA possess a complementary sequence of nucleotides, thus encoding the same genetic information.

Due to the chemical shift of core-level BEs, this chemical structure ought to be reflected in XPS spectra taken from the prepared samples. An overview spectrum recorded at a photon energy of 600 eV is shown in *Figure 3.5a*. This photon energy enables to probe a wide range in binding energy (BE) containing all significant core-levels. In addition to the Au $4f$ signal of the underlying gold substrate four intense PE lines arouse in the overview spectra which were identified as the signals from the C $1s$, N $1s$, O $1s$, and P $2p$ core-levels, respectively. Apart from hydrogen, which cannot be detected via XPS, these are the four elements contained in DNA molecules. Subsequently, detailed PE spectra of these four core-levels were recorded with a higher density of points and exploited for a chemical analysis of the samples. All spectra were aligned thoroughly in binding energy
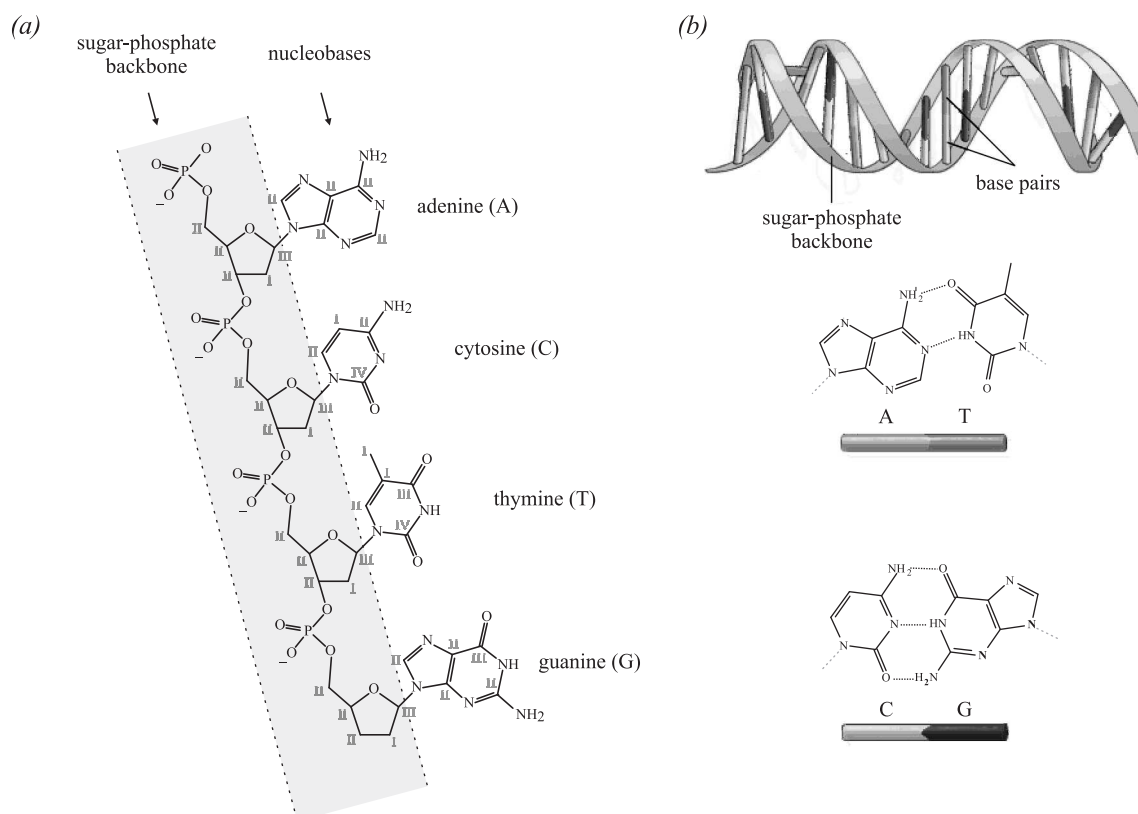
Figure 3.4: (a) Chemical structure of DNA. Carbon atoms are marked with the same roman number as the PE component in Figure 3.5b to which they contribute (cf. also Table 3.1). (b) The well-known double-helical structure forms when two complementary single-strands mate to a double-strand. Then the sugar-phosphate backbones wind around the stack of AT and GC base pairs.

by referencing them to the Au $4f_{7/2}$ peak of the gold substrate which was set to 84.0 eV.

The C $1s$ core-level PE spectrum (*Figure 3.5b*) reveals a manifold structure which consists of several, distinguishable PE components. This reflects the complex chemical structure of DNA molecules where carbon atoms are found in a variety of bonds. Least-squares fit analysis grants insight into the detailed structure of the C $1s$ PE spectrum. Its contour is reproducible with the help of four individual peaks (**I-IV**), in agreement with previous reports on nucleobases and DNA [57, 78, 79]. Following the initial state picture based only on electronegativities I propose the assignment summarized in *Table 3.1*, which is also supported by previously published data. Component **I** at 285.0 eV BE corresponds to pure carbon and hydrocarbon environments, denoted as C̲-C and C̲=C. When a more electronegative oxygen or nitrogen atom binds to a carbon atom, the latter contributes to component **II**. Of course, one cannot expect fully identical BE for, for instance, C̲-N and C̲-O type carbon atoms, but they are supposed to differ slightly in BE. Nonetheless, due to the only small difference I regard it as justified to gather all the mentioned chemical
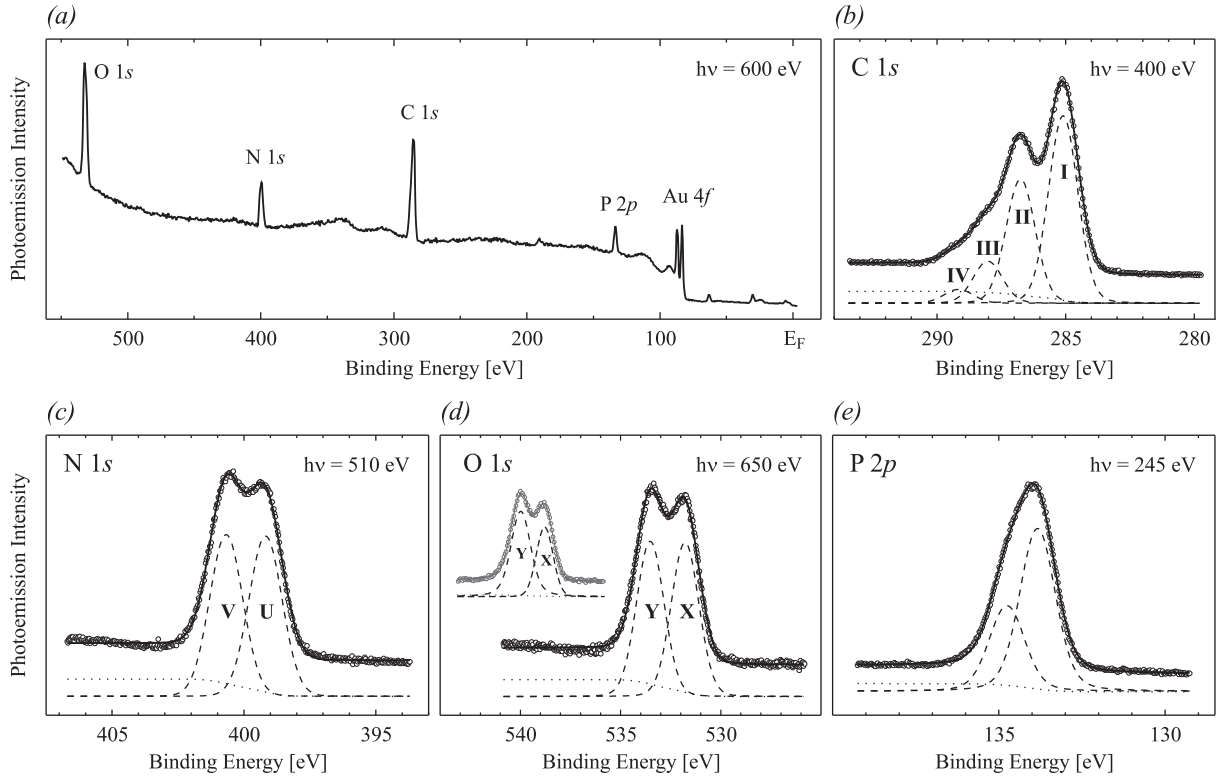
*Figure 3.5: Overview and high-resolution core-level PE spectra together with results of a fit analysis. Assignment of the PE components **I-IV**, **U-V** and **X-Y** is discussed in the text and summarized in Table 3.1. The inset in (d) shows an example of the occasionally observed enhancement of PE component Y which might indicate that in these cases only part of the backbone charge is compensated by Na$^+$ ions (for details see text).*

environments in component **II**. Additionally, using different peaks for each of them in the fit analysis would be far beyond the scope of our experimental resolution and hence not conclusive. If both oxygen and nitrogen are bound to a carbon atom the latter will either contribute to the PE component **III** or **IV** [59, 78, 79, 80].

Fit analysis of the N 1*s* PE signals (*Figure 3.5c*) reveals two components **U** and **V** at BEs of 399.1 eV and 400.7 eV. The O 1*s* spectrum (*Figure 3.5d*) is well described assuming two components **X** and **Y** at 531.4 eV and 533.1 eV BE. Again, the proposed electronegativity-based assignment (*Table 3.1*) is in good agreement with experimental results and calculations published previously [59, 80, 81, 82, 83]. Since, in DNA, phosphorus is found in only one chemical environment, namely the phosphate groups (PO$_4^-$) of the backbone, the P 2*p* PE line shows a simple doublet lineshape (*Figure 3.5e*). It was best fitted assuming a spin-orbit split of 0.92 eV between the 2$p_{3/2}$ and the 2$p_{1/2}$ component with the former located at a BE of 133.8 eV. These values do not only resemble tabular but also experimental values reported previously for DNA layers [57] and indicate intact structure of the phosphate groups. The experimentally found intensity ratio between the

core-level		BE [eV]	chemical group	relative PE intensity	relative occurrence
C 1s	**I**	285.0	$\underline{C}$-C, $\underline{C}$=C	51.0	18.3
	II	286.6	$\underline{C}$-O, $\underline{C}$-N, $\underline{C}$-NH$_2$, N-$\underline{C}$-N, N=$\underline{C}$-N	33.8	61.3
	III	288.0	N-$\underline{C}$-O, N-$\underline{C}$(=O)-C	11.4	15.3
	IV	289.2	N-$\underline{C}$(=O)-N	3.8	5.1
N 1s	**U**	399.1	C-$\underline{N}$H$_2$, C=$\underline{N}$-C	49.8	54.0
	V	400.7	$\underline{N}$-C-O, $\underline{N}$-C=O	50.2	46.0
O 1s	**X**	531.6	C=$\underline{O}$, P=$\underline{O}$, P-$\underline{O}^-\cdots$Na$^+$	49.8	50.0
	Y	533.3	C-$\underline{O}$-P, C-$\underline{O}$-C	50.2	50.0
P 2$p_{3/2}$		133.8	$\underline{P}$O$_4^-$	-	-

Table 3.1: Binding energies of the PE components in Figure 3.5 together with the assigned chemical structures. In the last two columns the relative PE intensity of each component is compared with the relative occurrence of the assigned atom type in salmon testes DNA.

$2p_{3/2}$ and the $2p_{1/2}$ component amounts to 1.9 : 1, which is close to the 2 : 1, expected from the respective m_j degeneracy of both fine-structure levels.

I will now turn to a quantitative analysis at which the relative occurrence of the chemical environments will be compared with the relative intensity of the respective PE component. In order to calculate the relative occurrence of a certain chemical group an *averaged* base-pair block was built by weighting the AT and the GC base pairs with their relative share in the DNA molecules, i.e. 41.2% for GC and 58.8% for AT. Then, this averaged block contains, for instance, 19.6 carbon atoms of which 3.6, 12, 3, and 1 contribute to C 1s PE component **I**, **II**, **III**, and **IV**, respectively.

For the N 1s and O 1s spectra both DNA stoichiometry and PE intensity are in excellent agreement. For the O 1s spectrum I occasionally observed a notable deviation from usually observed shape. Then the intensity of component **X** was reduced down to 45%, in one case even down to 37% (cf. inset in *Figure 3.5d*). One possible reason could be the adsorption of atmospheric oxygen or oxides to the surface. However, the corresponding O 1s PE signals are usually detected at lower BEs [84, 85] which would cause an relative enhancement rather than a reduction of **X** or even the appearance of a third spectral component below 531 eV. Also, the presence of carbon oxides would also cause a change in the C 1s line shape which was not detected. Moreover, extensive oxidation of the gold surface at room temperature is, in general, not observed. I, therefore, propose that causes related to the sample preparation process could be responsible for the above observation. Under the given preparation protocol one can assume that the negative charge of the DNA backbone is usually entirely compensated by sodium ions. Indeed, respective Na 2s and $2p$ PE lines at $\sim$64 eV and $\sim$32 eV BE, respectively, show up in the overview spectrum

(*Figure 3.5*a). Moreover, given their low cross section at hν=600 eV–approximately 5 times lower than the P $2p$ cross section and 9 times lower that the Cl $2p$ cross section [6]–the Na concentration seems comparable to that of the phosphate groups and, in light of the low Cl $2p$ PE intensity at 193 eV, only to a small part explained by traces of remaining sodium chloride.

I assume that the occasional redistribution of PE intensity from component **X** to **Y** is observed when, in the dried sample, the backbone charge is not entirely compensated by Na+ ions, but instead in parts by H$^+$ ions stemming from the aqueous solution, too. In this case, the claim of the counter ion to the surplus electron of the P-O$^-$ segment would be probably much larger[1] which could possibly affect the O $1s$ BE in the ground state or the core hole screening in the PE final state or both, thus leading to the observed enhancement of the high-BE component **Y**. Within that scenario, the relative intensity of PE component **X** could be lowered down to 33%, corresponding to a situation where H$^+$ counter ions compensate the entire backbone charge. Our experimental data varies within this range and may indicate that occasionally the backbone charge is not entirely neutralized by sodium but partly by H$^+$ ions, too.

The found general consistency of DNA stoichiometry and N $1s$ as well as O $1s$ PE intensity distribution is a good proof for intact molecular structures. Another probe for the sample quality is the P/N ratio. Since phosphorus is found in the DNA backbone, exclusively, whereas only the nucleobases contain nitrogen, the P/N ratio can also be exploited as a probe for the integrity of the DNA molecules [57]. However, comparison of intensities of different core-levels is not straight forward. In the case of crystalline solids core-level spectra are usually measured in the same kinetic energy range in order to obtain roughly similar electron mean free paths. Subsequently, they have to be normalized to incident photon flux and the respective subshell photoionization cross sections. However, in doing so I experienced sincere difficulties to estimate the photon flux of the RGBL accurately. This was most probably due to contaminations on the gold mesh and Si diode which are usually used for this purpose. Hence, in order to overcome these difficulties I decided to record the P $2p$ and N $1s$ spectra with the same photon energy of 510 eV, assuming that the mean escape depth of P $2p$ and N $1s$ electrons is basically the same within the DNA layer. After normalization to the respective subshell photoionization cross section and storage ring current one obtains an experimental P/N ratio of 0.29 which is in excellent agreement with the calculated 0.27.

While N $1s$, O $1s$ and P $2p$ PE signal as well as the P/N ratio are in convincing agreement with calculations based on the DNA molecule stoichiometry, there is a remarkably high discrepancy in case of the C $1s$ PE. Considering the reasonable accordance between the intensity ratio of the PE components **IV** : **III** : **II** amounting to 1 : 3 : 10 with the calculated 1 : 3 : 12, this discrepancy is partly repealed. Nonetheless, the fact remains that PE

---

[1]This is, for instance, indicated by the considerably enhanced ionization energy of hydrogen (1312 kJ/mol) when compared to sodium (496 kJ/mol) [86, 87].

component **I** at 285.0 eV is unexpectedly intense. This effect of increased $\underline{C}$-C like content in DNA samples is also visible in previously published spectra [57]. Although, the rest of the XPS data is in good agreement with DNA stoichiometry based expectations, partial desintegration of the DNA molecules cannot be entirely ruled out. However, I believe that the presence of carbon-carbon compounds on the substrate are the actual source for this unexpected C-C signal. Blank gold substrates that have undergone all steps of the sample preparation except for the actual DNA deposition also showed a C $1s$ PE signal, in the form of a single peak at 285.0 eV BE.

In summary, all features in DNA core-level PE spectra could be assigned to their respective chemical environment. Good agreement between the experimental data and the DNA stoichiometry indicates both intact structure of the deposited molecules as well as plausibility of the proposed spectral assignment. The separate XPS studies of alkanethiol SAMs and DNA molecules in this and in the previous section enables reliable interpretation of DNA microarrays where both are mate to obtain the desired functionality. This will be used in the next sections where the in 3.1 raised questions will be addressed.

3.4 Tuning the probe density in mixed DNA-MCH monolayers

Intermolecular interactions are both driving force and precondition for the formation of alkanethiol SAMs on gold surfaces [29]. It is the presence of *weak* neighbor-neighbor forces that allows for a closely packed and ordered structure on a large scale with the highest possible density of molecules reachable in a monolayer. In contrast to that there are *strong* intermolecular interactions between thiol-functionalized single- or double-strand oligonucleotides, because DNA molecules are negatively charged polyelectrolytes. Looking at the chemical structure in Figure 3.4 again, one recognizes that each phosphate group in the backbone carries a surplus negative charge. This leads to strong electrostatic repulsions between individual oligonucleotides and, in consequence, thiol-functionalized DNA probes usually anchor to the gold surface only at large intermolecular distances. The DNA probe density is accordingly small. But, naturally, higher densities are widely desired in order to gather full functionality of for example a sensor application on a considerably smaller area (cf. 3.1).

To this end, the repulsive forces between individual oligonucleotides must be highly suppressed which is commonly done by addition of salt cations to the solution from which the oligonucleotides are adsorbed. Then the phosphate groups can masking their negative charge by association with cations. Depending on the concentration and type of cations, conformational changes of the DNA strands take place [49, 88, 89, 90], leading to a decrease of the radius of gyration R_g of a coiled single-stranded DNA. This allows for a much higher probe density, which is proportional to $1/R_g^2$ [91, 92]. Previous studies demonstrate that,
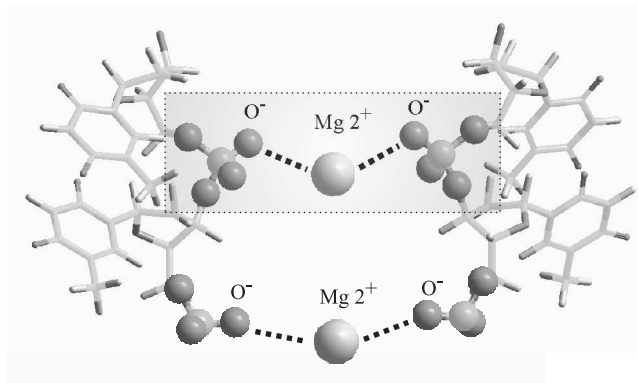
Figure 3.6: A possible scenario how divalent cations could neutralize the charge of two PO_4^- groups of different strands at the same time by linking both to a joint complex. This is expected to result in a very high DNA probe density within the DNA SAM.

indeed, the presence of monovalent cations like Na^+ and K^+ leads to an increase in probe density as well as immobilization and hybridization rate [50, 53]. The effect of divalent cations like Ca^{2+} or Mg^{2+} is even larger and already millimolar concentrations are sufficient to prepare highly dense DNA SAMs [56, 93, 94, 95, 96].

A possible explanation why divalent cations allow to achieve a superior probe density when compared to monovalent cations might be given with the following scenario. As discussed, monovalent cations with a single positive charge can associate with a negatively charged PO_4^- phosphate groups thus forming a charge neutral state. In that manner electrostatic repulsion between different backbones can be largely supressed. In the case of divalent cations, e.g. when using $MgCl_2$ salt, *two* phosphate groups from different strands can share a single Mg^{2+} ion in order to form an electrically neutral state. Then, beyond mere charge neutralization the divalent cation would fulfill the additional task to link the backbones of two DNA strands as visualized in *Figure 3.6*. This would decrease the average interstrand distance considerably and, therewith, lead to a much higher probe density.

It seems natural to assume that the effect of charge neutralization and the probability to form Coulomb-mediated $PO_4^- \cdots Mg^{2+} \cdots PO_4^-$ links between DNA strands has to be somehow sensitive to the amount of Mg^{2+} cations available. Since both effects are expected to increase the DNA package density, the latter might be directly controlled by varying the $MgCl_2$ concentration offered to a fixed concentration of DNA. However, systematic data on the dependence of the surface coverage on the Mg^{2+} concentration of the immobilization buffer is not available so far. Here this important issue will be investigated in more details. To this end, layers were prepared from aqueous solutions of 1 μM ssDNA (O1-SH) with $MgCl_2$ concentrations of 0, 2, 20 and 120 mM in the immobilization buffer, followed by MCH deposition to passivate the gold surface (for details see A.2.3. These samples were subsequently analyzed by means of XPS. Particular focus was put on how the ratio of MCH to DNA probe molecules on the gold substrate evolves as a function of $MgCl_2$ concentration.
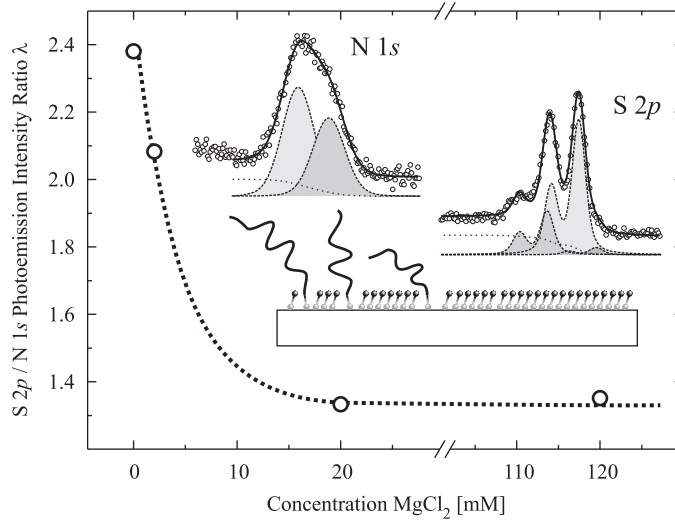
Figure 3.7: Ratio λ of the S 2p and N 1s PE intensity as a function of MgCl$_2$ concentration. The nitrogen signal originates from the DNA probes exclusively, whereas the sulfur signal reflects the MCH layer. The dotted line was added to guide the eye along the four measured points. The inset shows results of a least-squares fit analysis, used to estimate the intensity of both signals, for spectra obtained from a 20 mM MgCl$_2$ sample.

With growing package density of the oligonucleotides this number is expected to shrink and vice versa.

As a first approach, I determined the intensity ratio λ between the S 2p and the N 1s PE signal at a fixed photon energy of $h\nu$=510 eV. While the nitrogen signal originates solely from the DNA bases, the sulfur signal arises from both thiol-modified DNA probe molecules and MCH. However, assuming that the number of immobilized MCH molecules is always considerably larger than the number of DNA probe molecules, and taking into account that there is only one sulfur atom per 119 nitrogen atoms in O1-SH, the derived intensity ratio λ can be taken as a direct measure of the MCH-to-DNA molecule ratio.

In *Figure 3.7* I show the experimentally determined values of λ as a function of MgCl$_2$ concentration. In order to determine the intensity of the S 2p and N 1s derived PE a least-squares fit analysis was performed on each spectrum. Following the results in 3.2 the S 2p PE signal was deconvoluted using three doublets, each with a spin-orbit split of 1.1 eV and an intensity ratio of 2:1 between the $2p_{3/2}$ and the $2p_{1/2}$ component. In agreement with what has been found for pure DNA samples (3.3) the N 1s signal can be modeled using two singlet Voigt peaks at 400.7 and 399.1 eV BE. Results of the fitting procedure are shown in the inset of Figure 3.7 at the example of the 20 mM MgCl$_2$ sample.

Obviously, there is a drastic descent in λ when the MgCl$_2$ is increased from 0 mM via 2 mM to 20 mM. Above 20 mM λ settles down at a constant level. Accordingly, one can conclude that DNA probe density drastically increases between 0 mM and 20 mM MgCl$_2$

concentration, whereas higher concentrations do not lead to a further improvement.

It should be noted that although the PE intensity ratio λ is related to the relative number of sulfur and nitrogen atoms within the probe sample region, it is not necessarily a one-to-one representative for two reasons. First, at $h\nu = 510$ eV the PE cross sections differ significantly for the N $1s$ and S $2p$ core level [6]. Secondly, the photoexcited N $1s$ and S $2p$ electrons end up at very different kinetic energies and may differ significantly in their inelastic mean free path [97]. Of course, one could overcome these two obstacles by on the one hand normalizing the measure PE intensities to the well-known photon energy dependent ionization cross sections [6] and on the other hand probing both core-levels in the same kinetic energy window. Meanwhile the former can be done easily, the latter bears a severe problem. It requires a change in photon energy comparable to the energy separation of both core-levels, i.e. by $\sim$240 eV. For this, the beamline monochromator must be moved which, in practice, causes wandering of the beam focus across the sample, meaning that the probed sample region is changed. Because the researched samples cannot be assumed to be homogeneous, quantitative comparison of data taken at very different photon energies might not be conclusive. Therefore, I finally decided to probe both core levels at the same photon energy. Although, in this case quantitative information on the S/N ratio cannot be expected, the obtained λ values and their comparison for different MgCl$_2$ concentrations becomes reliable. In this way, the evolution of the probe density with the offered MgCl$_2$ concentration could be unraveled here.

However, an estimate of the absolute number of MCH molecules per DNA probe would be surely more valuable, because then one cannot only follow its relative evolution with growing MgCl$_2$ concentration, but may also give an absolute probe density which is of high relevance for practical applications. Aiming for that absolute number I propose a second approach where one tries to extract information on both DNA probes and SAM from one and the same core level, more precisely the C $1s$ PE signal. Although this may complicate the separation of the DNA and MCH derived signals considerably, one can avoid the above problems of differing cross sections and inelastic mean free paths.

For all four MgCl$_2$ concentrations the recorded C $1s$ PE spectra are shown in *Figure 3.8a*. Obviously, there are three different contributions to the C $1s$ PE signal: the MCH layer, the DNA probes and carbonaceous contaminations of the substrate. They were separated as follows. First, the line shape and BE of the contamination derived peak was determined by measuring a blank Au substrate which has undergone all steps of sample preparation except for the actual DNA immobilization and subsequent MCH backfill. Secondly, on the basis of the respective molecule stoichiometry I modeled line shape and BE position of the MCH and HS-ssDNA contribution using the experimental results discussed in 3.2 and 3.3. Thus for each of the three contributions its partial imprint on the C $1s$ spectrum, defined in energy position and line shape, could be obtained. These imprints then served as input for a least-squares fit analysis of the recorded C $1s$ spectra, with their intensities being the only free parameters.
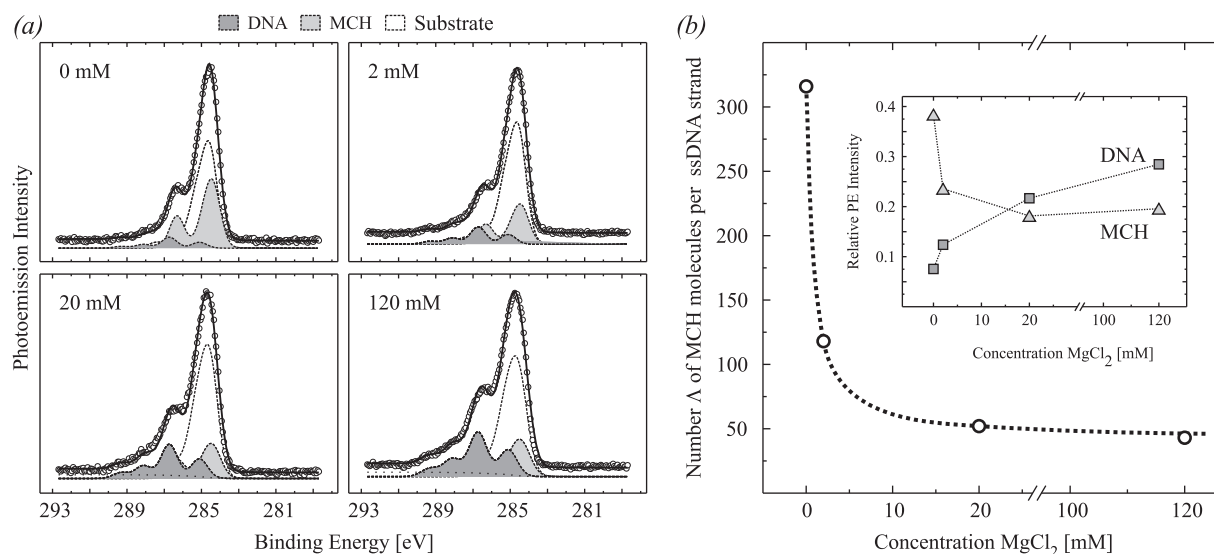
Figure 3.8: (a) Evolution of the C 1s PE spectra with growing MgCl$_2$ concentration. The spectrum contains contributions from C atoms of the DNA probes, of the MCH layer and of carbonaceous contaminations at the substrate surface. Details on their deconvolution are given in the text. (b) MgCl$_2$ concentration dependence of the ratio Λ of MCH molecules per DNA strand. Obviously, the DNA probe density increases with increasing MgCl$_2$ concentration. The inset shows the changes in relative photoemission intensity of both the MCH and the DNA contribution with growing MgCl$_2$ concentration.

Easily detectable even by eye there is a drop in MCH intensity when going from 0 mM to 20 mM MgCl$_2$ concentration. Simultaneously, the DNA signal is rising. In contrast, the substrate signal remains basically unaffected by the MgCl$_2$ concentration. Again, the ratio between MCH and DNA PE intensity can be used to characterize the probe density. This time, however, it directly reflects the number Λ of MCH molecules per HS-ssDNA probe, when weighting the PE intensity with the number of carbon atoms in the MCH and HS-ssDNA molecule. In *Figure 3.8b* I show the such obtained Λ as a function of the offered MgCl$_2$ concentration. Obviously, the found dependence strongly resembles that found with the more straight-forward approach of comparing the S 2p and N 1s PE intensity (*Figure 3.7*). Again, a drastic decline in the MCH/DNA ratio is observed when going from 0 to 20 mM in MgCl$_2$ concentration. Above 20 mM the ratio levels off at a constant value.

Note that both approaches to the dependence of DNA probe density in DNA SAMs on the concentration of MgCl$_2$ offered to a fixed DNA concentration in the immobilization buffer end up with a similar result. Hence it is justified to conclude that the density of DNA probes in DNA-alkanethiol SAMs can be widely and controllably varied with the offered concentration of MgCl$_2$. For the here used DNA concentration of 1 μM the critical range is essentially from 0 to 20 mM MgCl$_2$ concentration, i.e. the equivalent of 0 to 500 Mg^{2+} ions per phosphate group. A further increase of the MgCl$_2$ concentration does not lead to a significant improve in Λ.

The analysis presented in *Figure 3.8a* aimed particularly at an estimate for the DNA probe density on the gold surface. One can directly read from *Figure 3.8b* that Λ, i.e. the number of MCH molecules per DNA probe, drops from $\sim$325 for 0 mM MgCl$_2$ to $\sim$ 45 for 20 mM. That means in turn that the probe density can be improved by at least a factor 7 by adding a sufficient amount of divalent cations to the immobilization buffer. Furthermore, by assuming that MCH forms a nearly complete monolayer one can give estimate of the absolute surface density of DNA probes. $\Lambda = 45$ would then correspond to a density of ca. 10^{13} cm^{-2} which levels at the top-scale of the hitherto reported values [48]. Because parts of the surface were probably disabled for DNA-SAM formation by the detected contaminations I expect that these densities were realized only in some regions of the studied samples. However, this is not a principal obstacle and can easily be overcome by improving of the substrate preparation procedure.

3.5 Influence of the solvent type on the DNA-SAM

The choice from which type of solvent, aqueous or ethanolic, a DNA-SAM is prepared might be crucial. The situation is somehow ambivalent because densely packed alkanethiol SAMs are usually achieved by assembly from ethanolic solutions [32]. On the other hand, ethanol is known to cause condensation of DNA [98] and commonly used to precipitate solved DNA [99]. This poses the question whether an MCH backfill from ethanolic solution might corrupt the quality the mixed DNA-MCH layer. To date this is an unsolved puzzle, which will be addressed in more detail in this section. To this end, layers prepared from both ethanolic and aqueous solution were investigated by means of XPS and compared in their structural quality. The detailed sample preparation protocol is given in A.2.4). For the data analysis I will make use of the experimental findings discussed in 3.2, where the spectral shape of the S $2p$ PE was established as a benchmark for the structural quality of alkanethiol SAMs. Beside the type of solvent the MCH concentration in the solution, from which the MCH backfill is accomplished, might be of additional impact on the achieved structural quality. In order to shine some light on this point, too, the MCH concentration was additionally enhanced in the ethanolic solution.

The S $2p$ spectra for different kinds of layers prepared from both ethanolic and aqueous solution are jointly shown in *Figure 3.9*. Going from the bottom to the top I show spectra obtained from pure MCH layers and from mixed layers where dsGC DNA molecules with a length of 30 and 60 base pairs, respectively, were immobilized prior to MCH deposition. In accordance with the results presented in 3.2 one finds a dominant doublet with the $2p_{3/2}$ peak at 161.9 eV BE in each spectrum, accompanied by two less intense doublets with the $2p_{3/2}$ at 163.2 eV and 161.1 eV BE, respectively. As discussed, the low BE doublet originates from bound thiol groups with a higher coordination to the gold surface and basically reflects surface defects. In contrast, the doublet at 163.2 eV BE corresponds to unbound sulfur and, thus, its relative intensity is a direct measure of the structural order
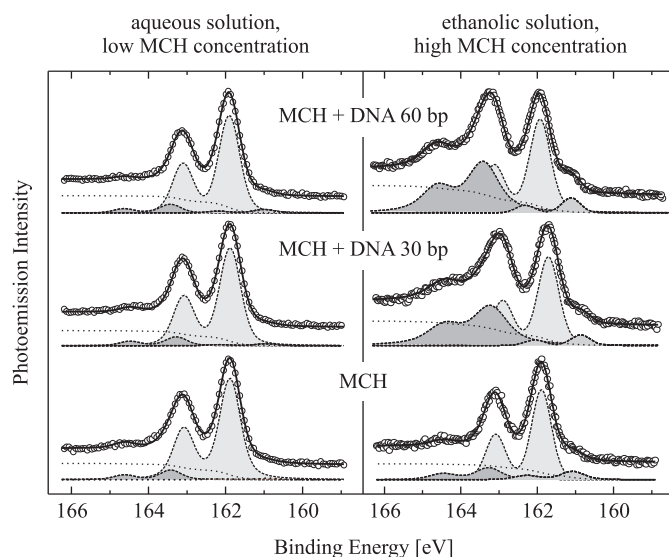
Figure 3.9: S 2p PE spectrum for a pure MCH layer and mixed MCH-DNA layers prepared from either a 1 mM aqueous solution or a 117 mM ethanolic solution. Drastic enhancement of the high-BE doublet for the mixed DNA-MCH self-assembled monolayers indicates severe corruption of the structural order in the ethanolic case. Using an aqueous type of solvent, densely packed SAMs were routinely achieved for both pure MCH and mixed DNA-MCH layers.

of the MCH layer, where high intensity indicates a strongly disorder layer.

In case MCH was post-deposited from the aqueous solution (left panel of *Figure 3.9*), a high structural order was constantly observed for all three types of sample. The related relative intensity of the 163.2 eV component was always as low as ∼8%. In contrast, when the MCH backfill was done from the ethnolic solution (right panel), the relative intensity of the high-BE component increased to ∼40% and more for the mixed DNA-MCH layers, indicating extensive corruption of the structural order. For the pure MCH layer structural order is similar to that found for the layers prepared from aqueous solution.

Additional to the presented S 2p spectra the N 1s and P 2p PE spectra were recorded for each sample (not shown). They are 100% related to the DNA content of the layers and can be used to monitor the intactness of the deposited DNA strands (cf. 3.3). Comparing with spectra taken from pure dsDC samples without any MCH treatment, they always showed similar line shapes equal to those of the reference samples, no matter the solvent type or DNA-strand length. Obviously, the type of solvent does not seem to affect intactness of the deposited DNA strands themselves.

In conclusion, the use of aqueous, 1 mM MCH solutions seems highly advisable to achieve a high structural order in mixed DNA-MCH SAMs on gold surfaces. Several factors might be responsible here. First, in ethanolic solution MCH molecules could easily adhere to the DNA strands by hydrogen bonds and might be retained there during the final rinsing with ethanol [61]. In contrast, such hydrogen bonds cannot be established in

aqueous solution because of the strongly polar character of the H_2O molecule. Secondly, in an ethanolic solvent the DNA strands could condense to a polymer and adhere non-specifically to the gold surface [98], thus disturbing the structural order of the MCH layer. Also, such non-specifically bound DNA could not be as easily removed as in aqueous solution, because water is a much better solvent for nucleic acids that ethanol. An third possible factor might be the much higher MCH concentration in the ethanolic solution (117 mM compared to 1 mM in case of the aqueous solution). An exceedingly high thiol concentration is also suspected to result in a high number of unbound thiols deposited within or above the SAM [68]. However, there is some evidence here that an overdosed MCH concentration in itself does not categorically result in a disordered film. Note, that for the pure MCH layers a constantly high order was routinely achieved independent on the type of solvent. Only when DNA strands are present on the gold surface during the MCH deposition, a significant disturbance in the structural order shows up. It may be conceivable that intensified MCH-DNA interaction in the overdosed case, for instance via hydrogen bonds, could be mainly responsible for that observation, and that DNA condensation plays only a subordinate role. Then a higher structural order might also be obtained even for the ethanolic solvent type by reducing the MCH concentration to a more moderate level. This question, however, can be ultimately answered only after additional experimental efforts.

3.6 Indication of a competitive interplay between MCH and thiolized DNA when simultaneously absorbed to gold surfaces

Usually, the preparation of mixed DNA-MCH SAMs is accomplished in two consecutive steps, first immobilization of the thiolized DNA strands on the gold surface followed by the alkanethiol backfill to passivate the remaining free gold surface by a self-assembled monolayer. It is generally thought that a temporal separation of these two steps is required because DNA immobilization and SAM formation run on very distinct time scales. Note that in order to achieve high probe densities the gold substrates are usually immersed for hours in the immobilization buffer whereas alkanethiol SAM formation on gold can be accomplished within few minutes [29]. Therefore, it appears reasonable to don't let both processes, anchoring of DNA and passivating of the metal surface, interfere with each other by performing them consecutively. In fact, all DNA-SAM samples discussed so far were prepared in this manner.

In contrast to this common approach it was proposed only recently that when exposing a gold surface to both thiolized DNA and MCH *simultaneously* one can achieve high package densities, too [94]. Moreover, applying impedance measurements to respective samples the authors argue that by variation of the relative concentrations of DNA and
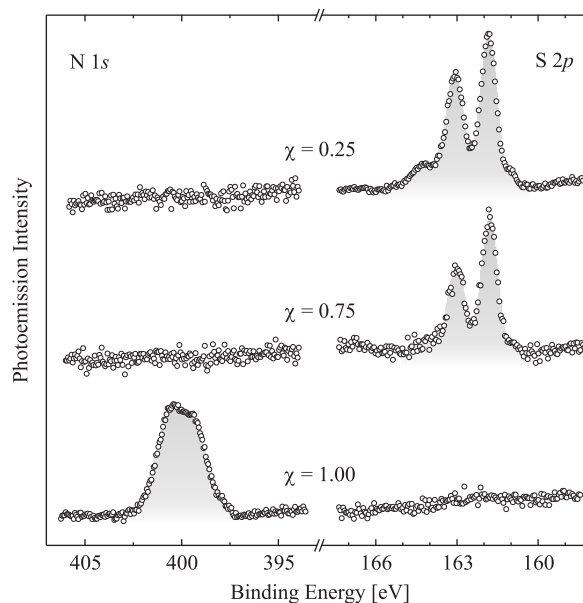
Figure 3.10: N 1s and S 2p PE spectra taken from samples where the relative concentration of thiolized DNA χ had been gradually raised to 1 on the cost of relative MCH concentration. Absence of N 1s PE intensity for $\chi = 0.75$ and below shows that no noteworthy number of dsDNA probes had adsorbed to the gold surface.

MCH in the solution one might even tune the DNA probe density. Considering that in doing so one potentially favors one of the two rivaling processes, i.e. DNA immobilization or MCH surface passivation, over the other, this appears to be a possible scenario. However, interpretation of impedance measurements is complicated by the fact that there is no chemical selectivity allowing to reliably separate MCH and DNA contributions to the measured impedance and further experimental studies are surely needed. For example, it is somehow puzzling that the highest DNA probe densities were not found when the DNA concentration was raised on the cost of MCH concentration, but instead when MCH and DNA concentration were set comparably.

Here I want to study in more detail the competitive interplay between thiolized DNA and MCH when allowed to simultaneously adsorb to a gold surface. To this end, gold substrates immersed into aqueous, mixed dsDNA-MCH solutions were analyzed by means of the chemical selective XPS. While the total thiol concentration had been kept constant at 1 μM, the relative concentration χ of the thiol groups of the DNA linkers had been gradually raised from $\chi = 0.25$ to $\chi = 1.00$ in steps of 0.25. Accordingly, the relative concentration of MCH thiol groups had been 0.75, 0.50, 0.25 and 0.00, respectively (for details on sample preparation see A.2.5).

In *Figure 3.10* I present the S 2p and N 1s PE spectra obtained from samples with growing χ. Spectra found for $\chi = 0.50$ are not included but were similar to those observed for $\chi = 0.25$ and $\chi = 0.75$. It should be noted again that N 1s intensity is related to
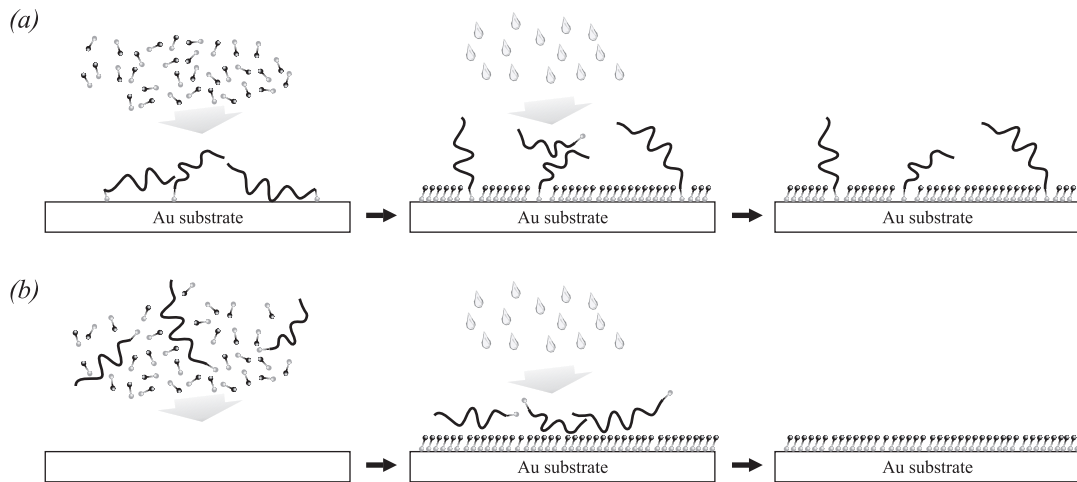
Figure 3.11: (a) Consecutive run of the slow-running DNA immobilization and the fast-running alkanethiol SAM formation: The desired mixed DNA-MCH layers are routinely achieved. (b) Simultaneous run: The thiolized DNA is blocked from any anchoring site on the surface by the rapidly constructed SAM and washed away during the final rinse cycle.

DNA presence in the sample, whereas the S $2p$ signal reflects primarily the MCH content of the film (cf. 3.4). Accordingly, for $\chi = 1.00$, i.e. no MCH present in the solution, an intense N $1s$ signal showed up whereas at best only tiniest S $2p$ features were monitored. Surprisingly, no nitrogen was found for $\chi = 0.75$ samples and below, where only the SAM related S $2p$ signal is clearly visible.

The absence of an N $1s$ PE signal is quite remarkable because this seems to clearly conflict with the results obtained with impedance measurements. Apparently, there is no noteworthy number of immobilized DNA probes on the gold surface for $\chi <\sim 1$, and, surely, $\chi = 0.5$ did not breed maximum probe density. It is natural, to link the absence of DNA probes in our samples to the introduced competition with MCH molecules for unpopulated surface regions, because under absence of MCH in the solution ($\chi = 1.00$) DNA immobilization is readily achieved. Two aspects should be considered for a possible explanation of this experimental finding. First, dense population of the gold surface with an MCH SAM would surely frustrate the surface immobilization of DNA probes. Secondly, due to the high mobility of the short alkanethiols a closed monolayer, holding already circa 90% of the highest possible molecule density, is established within few minutes [29, 100]. The thiolized dsDNA, on the other hand, with its large molecular weight and size possesses a drastically lower mobility. Moreover, steric hindrance may severely impede quick contact between its thiol linker and the substrate surface.

Both aspects can be cooked down to a scenario as visualized in *Figure 3.11*. If DNA anchoring and alkanethiol monolayer formation are performed consecutively, the oligonucleotides will be given a sufficiently long time to diffuse to the Au surface and establish contact. Upon subsequent immersion into the alkanethiol solution vacant areas of the

substrate are populated with a SAM. Subsequent rinsing leaves behind a mixed layer of anchored DNA probes and self-assembled alkanethiol monolayers (*Figure 3.11a*). When enabling competition between DNA anchoring and SAM formation by performing both simultaneously the alkanethiols benefit from their significantly higher mobility. If available in sufficiently high concentration they rapidly populate the entire surface with a SAM, thus blocking the oligonucleotides. Having no anchoring contact the latter are simply removed during the rinse cycle (*Figure 3.11b*).

Summarizing, it seems advisable to avoid any competition for free gold surface between thiolized DNA and alkanethiols by performing DNA immobilization and MCH backfilling consecutively. Both processes appear to run on distinct time scales because of the very different mobility of DNA and MCH molecules. It should be mentioned that in the present study this difference in mobility was even enhanced in comparison to the impedance study, because instead of single-strand DNA almost two times longer double-strand DNA probes were used. However, this cannot explain the general difference in the experimental findings.

3.7   Summary

It was demonstrated that synchrotron-based high-resolution X-ray photoemission spectroscopy allows to characterize structural properties of mixed DNA-alkanethiol self-assembled monolayers which found application as e.g. DNA microarrays. Starting from investigations of pristine alkanethiol SAMs and genomic DNA a number of unsolved puzzles related to these mixed layers could be successfully addressed. The probe density, determining the functional density and efficiency of a DNA microarray, can be controllable tuned by offering divalent cations in a well-dosed concentration in the solution from which DNA immobilization is accomplished. The critical range in which a variation of $MgCl_2$ concentration affects the probe density was determined. At $\sim$500 Mg^{2+} ions per phosphate group the maximum density was reached which is more than 7 times higher than densities achieved under absence of divalent cations. Furthermore, preparing from aqueous instead of ethanolic solution prevents severe corruption of the structural order in the DNA-MCH SAMs. Finally, when exposed simultaneously to the gold surface there appears to be a strong competition between DNA immobilization and MCH layer formation, where the latter is highly favored. Therefore, application of preparation methods where both steps are performed consecutively seems advisable.

In general, the obtained results verify the capability of high-resolution XPS to probe and characterize structural properties of self-organized systems, which are defined by the interaction of a huge number of molecules. In contrast to many other experimental techniques, including electron or tunneling microscopy, synchrotron-based PE spectroscopy can access the in such systems relevant mesoscopic scale easily and with chemically selectivity. As demonstrated with the above studies this allows very specific and reliable insight into a variety of problems, which are hard to obtain by other means.

4 Modification of the peptide bond by atomic and ionic calcium: Metal binding mechanism in protein structures

4.1 Introduction

In many biological processes calcium and calcium ions play an essential role, be it on the cellular and subcellular level, e.g. in membrane channels [101, 102, 103, 104, 105, 106], on the level of the neuronal system as the fuel that drives neurotransmitters [107, 108], or on the level of structural support and skeletons where hardness and stability is widely achieved by incorporation of calcium compounds [109]. Essentially, on every scale living nature uses calcium, in different functions and chemical states.

In the recent two decades biological systems have been discovered for revolutionary new approaches to future technologies. That applies in particular to the nanoscopic scale where the unique self-organizing capabilities and well-defined structural properties of biomolecules like proteins or DNA become fully apparent. One example is the class of bacterial surface layer (S layer) proteins [110, 111, 112] which self-assemble in well-defined, highly structured two-dimensional sheets (*Figure 4.1*). They thus represent ideal biomolecular templates for growing regularly arranged inorganic cluster arrays, as has already been demonstrated for a couple of materials [113, 114, 115, 116, 117, 118, 119]. Furthermore, a wide gap semiconductor-like electronic behavior has been observed for these proteins [120] which, if accompanied by a principal potentiality of doping, may possibly allow their technological application in organic or mixed organic-inorganic electronics.

Both their structural and electronic properties–for themselves or in combination–make the S layer proteins a highly promising material for the future development of nanoscopic devices. However, its systematic utilization for fabrication of hybrid nanostructures as well as for biomolecular templating requires detailed knowledge about all kinds of interaction between the S layer and additionally employed materials. Given its involvement in many essential biological processes, often hand in hand with proteins [105, 106], calcium (and
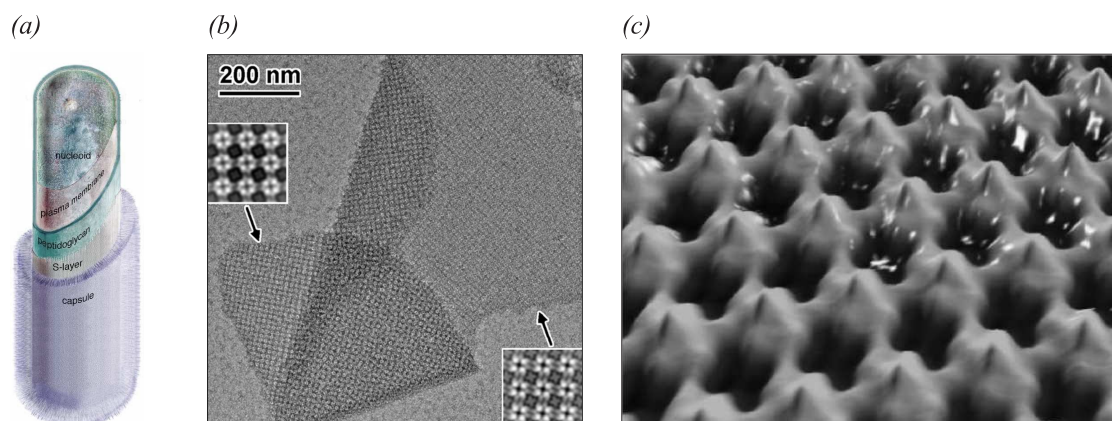
(a) *(b)* *(c)*

Figure 4.1: *(a) The S layer, a regular, 2D-crystalline protein layer, is part of the cell envelope of many bacteria. When isolated from the bacterium the S layer is able to reconstruct in aqueous solution via self-assembly. The reconstructed 2D crystalline sheets can easily be deposited onto various substrates by physisorption. (b) TEM micrograph of a deposited S-layer sheet. (c) Highly spatial-resolved TEM image of a deposited S layer clearly showing the 2D crystal structure with 4-fold symmetry (U. Sleytr, University of Viena).*

other alkine earth metals) could play an important role as S layer partner material in technological applications. Especially with regard to a potential exploitation as electron donors for doping of this biological semiconductor future employments might seem imaginable.

In order to characterize the interaction between the 2D crystalline S layer and calcium or other metals, in particular with regard to how and where the individual metal atoms are incorporated into the protein structure, experimental methods that can probe all the way down to the atomic level are required. Unfortunately, even in today's most advanced microscopy facilities atomic resolution in proteins is missed by orders of magnitude (cf. *Figure 4.1c*). Also classical diffraction techniques as routinely applied to solids fail because they require a 3D rather than a 2D crystal structure. Recently, successful 2D crystallography using a X-ray free electron laser (FEL) source has been demonstrated [121]. However, resolution did not exceed ∼50 nm and Å resolutions will be available only with the hard X-ray FEL facilities currently under construction.

Therefore, spectroscopic techniques must currently be the means of choice to study protein-metal structures on the level of individual atoms. In classical semiconductor physics, for instance, Raman spectroscopy is well-established to study the incorporation of few donor atoms into the crystal structure. However, in case of proteins the unit cell does not contain only few atoms but rather thousands of atoms, and the number of resonances in Raman spectra becomes accordingly high [122]. Hence, even spectra of very small proteins or peptide chains of only few amino acids are hard to interpret [123, 124]. Moreover, to date there is no Raman reference data available for pristine S layers or comparable protein structures. Therefore, application of Raman spectroscopy seems not very promising for

studying the considered protein-metal hybrid systems either.

Here, I studied the interaction between the bacterial surface protein layer of bacillus sphaericus NCTC 9602 and individual calcium atoms using the methodically mature and powerful techniques of high-resolution PE and NEXAFS spectroscopy. The synchrotron experiments where accompanied by *ab initio* calculations helping to gain comprehensive insight into calcium-protein interactions from both experimental and theoretical point of view and for different ionization states of calcium, i.e. Ca^{0+}, Ca^{1+} and Ca^{2+}.

4.2   Binding site of calcium in the protein structure

4.2.1   Experimental results

Bacterial surface protein layers were isolated from the bacterium *Bacillus sphaericus* NCTC 9602 and deposited *ex situ* onto naturally oxidized silicon wafers by physisorption. Details on the sample preparation protocol are given in A.2.6. Part of the samples had been checked by means of transmission electron microscopy (TEM) (*Figure 4.1b*) and atomic force microscopy (AFM, not shown) to verify successful deposition of the desired, 2D-crystalline sheets. In order to study the interaction between the protein layer and individual calcium atoms, XPS and NEXAFS spectroscopy were applied to S layer samples prior and after deposition of increasing amounts of calcium. Calcium deposition onto the S layer was done *in situ* by electron beam evaporation from a crucible and monitored with a carefully calibrated quartz microbalance.

X-ray photoemission spectroscopy

Core-level PE spectra taken from the native S layer and after deposition of gradually increased amounts of Ca are shown in *Figure 4.2*. Clearly, the spectral shape of the protein derived C 1*s*, N 1*s* and O 1*s* spectra is significantly altered with increasing Ca deposition. To give an interpretation of the observed changes an understanding of the native protein spectra prior to calcium deposition is needed first. To this end, I performed a least-squares fit analysis. Its results are shown together with the respective spectra. Because electron correlation effects in low-Z molecules are only minor, assignment of the different, chemically shifted components within a simplified, initial state picture is justified (cf. 2.1.2). Even though a simplification this picture has been successfully used in the interpretation of protein core-level PE spectra before [120].

The shapes of the native protein spectra in *Figure 4.2* resemble those previously reported for the S layer [125]. The C 1*s* spectrum features a pronounced structure which was well reproduced in a fit with three individual Voigt peaks of identical line width. The
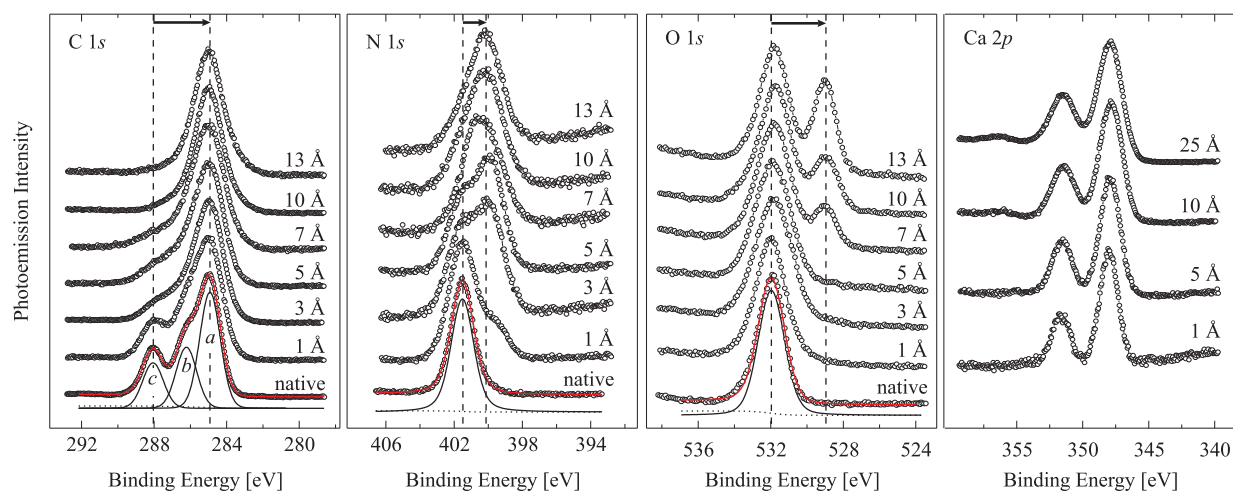
Figure 4.2: Core-level PE spectra of the native S layer and after deposition of different thicknesses of calcium, together with the corresponding Ca 2p spectra. For the native S layer results of a fit analysis are included. The black arrows indicate the shift of the peptide bond originated PE features upon Ca deposition. Up to 25 Å the Ca 2p spectra exhibit identical shape, indicating similar chemical bonding of all Ca atoms.

three components **a**, **b** and **c** show up at 285.0 eV, 286.5 eV and 288.1 eV binding energy, respectively. Following the initial state interpretation of the chemical shift, carbon atoms contributing to **a**, **b** and **c**, respectively, have an increasingly electronegative chemical environment. More precisely, **a** is commonly assigned to C atoms in hydrocarbonic or aromatic structures, **b** to atoms bound to nitrogen or oxygen, and **c** to atoms incorporated in the peptide units. In the latter case one can expect considerable charge transfer from the probed carbon atom to the more electronegative binding partners oxygen and nitrogen, resulting in an increased C 1s BE. In contrast, in the case of hydrocarbonic structures (component **a**) the valence electron density will concentrate mainly around the carbon sites.

Upon analysis of the S layer protein stoichiometry [126] one finds that according to the above assignment 49% of the protein C atoms should contribute to **a**, 32% to **b** and 21% to **c**. This is in very good agreement with the measured relative intensities of 52%, 27.5% and 20.5%, respectively. Occasionally carbon atoms in carbonyl groups are proposed to contribute to **c**, too. Then, one would expect relative intensities of 46%, 28% and 26% for peaks **a**, **b** and **c**, respectively, which is also close to our measured data. It should be stressed, that in either case, it is justified to assume that **c** reflects in the main (or entirely) carbon atoms in peptide bonds.

For the N 1s spectrum, the fit-analysis reveals a single-peak structure, indicating a rather uniform chemical shift of all N 1s core-levels. Indeed, the vast majority of nitrogen atoms are found in comparable chemical environments. In detail, 83% participate in peptide bonds and 8% in the chemically closely related amide groups of the protein side chains,

wheras only ∼9% are involved in other, carbon-nitridic structures. However, chemical shift of the latter should be close to that of the other nitrogens, since additional to the 401.6 eV BE peak no other features show up in the spectrum.

Though a single Voigt peak at 531.8 eV BE generally describes the O $1s$ spectrum well there are also some smaller deviations which points to an underlying structure with several components very close in binding energy. In parts, this might be because of the different chemical states of oxygen in the protein. While 86 at.% are incoporated in peptide units and similar carbonyl groups, another 14 at.% take part in the unalike hydroxyl groups. However, it should be noted, that the SiO_x substrate should make strong contribution to the O $1s$ photoemission signal, too. In order to characterize this contribution, I additionally measured blank SiO_x wafers and found a single O $1s$ peak at virtually the same BE as detected for the S layer sample. Therefore, I conclude that contributons of both S layer and substrate merge in the 531.8 eV peak.

Now, with growing calcium deposition, more and more pronounced deviations from the spectra of the native S layers become apparent. This demonstrates that the deposited calcium atoms induce severe modifications of the chemical bonding within the S layer. In detail, the following changes in the $1s$ spectra are observed.

1. While component *a* of the C $1s$ spectrum remains widely unaffected, *c*, and in large part also *b*, vanish. Please be reminded that *a* mainly represents the protein side chains with their primarily aromatic and hydrocarbonic structures, whereas particularly *c* is related to the peptide backbone. With that in mind it seems that the main impact of the calcium deposit is on the peptide units. But what precisely causes *b* and *c* to vanish from the spectrum? A study of radiation damage effects in proteins shows that even upon massive energy transfer into the protein structure, leading to its desintegration, no carbon desorption from the sample takes place [127]. Therefore, it is more plausible that the components *b* and *c* are chemically shifted to lower BE such that they now merge with the main component *a*, rather than to assume that both vanished because of desorption of the corresponding carbon atoms. In this scenario, the maximum red shift amounts to ∼3 eV as indicated by the black arrow in *Figure 4.2*.

2. With growing calcium deposition a second component at 400.0 eV BE component rises in the N $1s$ spectrum and becomes dominating soon. Again, the Ca atoms appear to mainly affect the protein backbone, because the 401.3 eV peak basically reflects the peptide bond nitrogens. Note, that even beyond 7Å Ca deposition a constant rest intensity remains at the original peak position at 401.3 eV. This might indicate missing interaction of nitrogen atoms in carbon-nitride structures (9 at.%) with the deposited Ca atoms.

3. Similar to what was found for the N $1s$ spectrum, calcium deposition gives rise to a second, well-separated peak in the O $1s$ spectrum at 528.8 eV, i.e. shifted by 3 eV

to lower BE. This time, however, the original peak keeps considerable intensity even beyond 7 Å Ca deposition. Obviously, a part of the probed oxygen atoms does not notably interact with the Ca atoms. It is reasonable to assume that this is the SiO_x fraction, because analysis of the C $1s$ and N $1s$ PE already revealed strong effects on the protein layer and in particular the peptide backbones. Therefore, I assign the shifted low BE peak to the S layer, in particular to Ca-affected oxygen atoms of the peptide backbone while the unaffected high BE peak is representative for the SiO_x substrate.

4. At least up to 25 Å calcium deposition only a single Ca $2p$ doublet is observed. Obviously, all Ca atoms interact very similarly with the protein. The energy separation of 3.6 eV and the intensity ratio of 1.8 : 4 between the $3p_{1/2}$ and the $3p_{3/2}$ fine-structure level agrees well with previously found values [128] and the corresponding m_j degenerations (2 : 4), respectively.

To summarize, all PE features of the peptide backbone are clearly shifted towards lower BE. Considering only initial state effects of the chemical shift, this indicates that the valence electron density around the respective C, N, and O sites was considerably enhanced upon calcium deposition because of an improved screening of the corresponding core potentials. This effect can be consistently explained in the following scenario: Deposited Ca atoms transfer part of their $4s$ charge into the peptide backbone, thus increasing the valence electron density in the latter. The largest impact is on the O $1s$ and C $1s$ core level ($\sim$3 eV each) and smaller for N $1s$ electrons ($\sim$1.3 eV), which implies, that the transfered charge is concentrated around the C=O site of the peptide bond.

I propose that the Ca atoms bind to the oxygen sites of the peptide bonds and transfer their $4s$ electrons into the newly formed molecular orbitals. In the native protein, the oxygen atoms are the most electronegative site in the peptide backbone and detract much of the original valence electron density from the adjacent C site and to a smaller extent also from the N site. This is, for example, reflected by the massive blue shift ($\sim$ 3 eV) of the C $1s$ core-level when compared to purely carbonic groups (peaks **c** and **a**, respectively). Now, when Ca binds to oxygen, it readily donates its $4s$ electrons to the O site, forming a new bond of highly ionic character. In turn, the adjacent carbon and nitrogen atom must donate much less of their valence electrons to the already "saturated" oxygen and thus regain much of their valence density. Accordingly, the C $1s$ and to a smaller extend the N $1s$ BE would decrease when the Ca docks to oxygen because of better core potential screening. Indeed, corresponding $1s$ redshifts of 3 eV and 1.3 eV were observed supporting the proposed scenario.

I want to stress, that a similar charge transfer from the Ca deposit to the SiO_x substrate can be excluded because the wide-band semiconductor SiO_x features no states close to the Fermi energy. Calcium atoms deposited onto the substrate would be still in full possession of their $4s$ electrons and thus be able to screen their $2p$ electrons better from the core potential. Because Ca $2p$ PE spectra for up to $\sim$25 Å show only a single doublet line
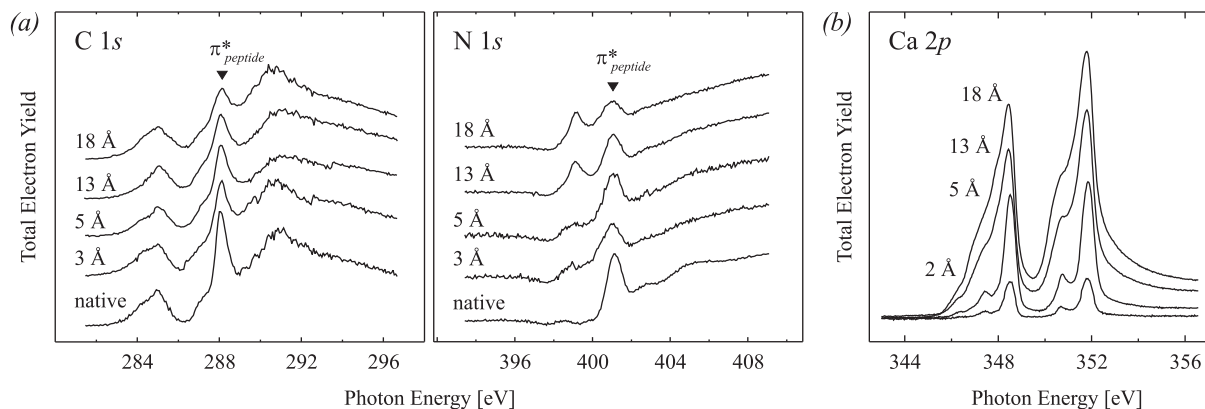
Figure 4.3: (a) NEXAFS spectra taken at the C 1s and N 1s absorption threshold for the native protein layer and after deposition of Ca. The clear decline of the $1s \rightarrow \pi^*_{peptide}$ resonances proves strong impact of the deposited Ca atoms on the peptide bonds within the protein layer. (b) Ca 2p NEXAFS spectra for different amounts of deposited calcium. Though growing in intensity the spectra preserve their shape indicating similar chemical bonding of Ca throughout the different amounts of deposition.

with no additional low energy features, one can conclude that the vast majority of Ca is deposited onto and binds to S layer sheets which points to high surface coverage.

NEXAFS spectroscopy

Comparison of core-level PE spectra before and after deposition of calcium suggested that the oxygen sites of the peptide backbone bind calcium atoms. If that is true the character of the former peptide bonds, meaning its molecular orbitals, should become drastically altered. Such changes should be detectable by means of NEXAFS spectroscopy because this techniques probes transitions into unoccupied molecular states close to a specific X-ray absorption threshold (see 2.2.2).

For the two most relevant absorption thresholds, i.e. the C 1s and N 1s edges, NEXAFS spectra of the protein layer without and with deposited calcium are shown in *Figure 4.3a*. All spectra were normalized in a way that they coincide in the pre-edge and far-edge region. Due to their sharp and distinct structures I will only consult the π^* region of NEXAFS spectra for analysis. As will be discussed in very detail in 5.4 photoabsorption-induced transitions of C 1s and N 1s electrons into unoccupied π^* orbitals of the peptide bond ($\pi^*_{peptide}$) give rise to two intense absorption peaks at 288.1 eV and 401.3 eV photon energy, respectively. Both peaks are clearly visible in the spectra of the native S layer presented in *Figure 4.3a* where they are marked with black triangles.

At the C 1s absorption edge, a decline in intensity is detected for the $1s \rightarrow \pi^*_{peptide}$ resonance with increasing Ca deposition. On the other hand no new sharp resonances

shape up in the π^* region of the spectrum which suggests that the lost intensity was transfered to the σ^* region. Obviously, the symmetry of the $\pi^*_{peptide}$ molecular orbital is changed significantly when calcium binds to the backbone oxygen sites. This does not come unexpected since with formation of a calcium-oxygen bond (N-C-O-Ca), the former N-C=O group loses its partial double bond character.

Intensity loss of the $1s \rightarrow \pi^*_{peptide}$ resonance is also observed at the N $1s$ threshold. Here, however, it is accompanied by the uprising of a new π^* resonance at 1.9 eV lower photon energy. Obviously, the bonding of nitrogen is not significantly altered with regard to its symmetry character but mainly affected in energy. Now, transitions from the $1s$ core level to the π^* orbital require much less energy in case calcium is attached to the peptide unit. The conserved symmetry may be reasoned by the fact that the nitrogen atom is not directly involved in the newly formed C-O-Ca bond. The downshift of the π^* absorption peak in photon energy mainly reflects the lowered N $1s$ BE also detected in PE. There, however, the downshift amounted to only 1.3 eV. The difference of 0.6 eV is most likely due to final state effects. Note, that the PE and NEXAFS final states differ significantly, because in the former process the excited electron is ejected out of the system, whereas in the latter process in remains in the system and can, for instance, help to screen the generated core hole.

In general, the changes in the NEXAFS spectra did not set in as drastically as in the PE spectra for low Ca deposition rates. For instance, at 13 Å the PE spectra bear no resemblance anymore to the respective spectra taken from the native protein, whereas the C $1s$ and N $1s$ NEXAFS spectra still show significant traces of the characteristic $\pi^*_{peptide}$ resonances. This, however, does not come unexpected. Because of the larger probing depth in NEXAFS spectroscopy deeper lying unaffected regions of the protein layer, which are not probed in PE, will still contribute to the NEXAFS spectrum.

In *Figure 4.3b* Ca $2p$ NEXAFS spectra for different amounts of deposited calcium are compared. The spectra are shown after normalization to the incoming photon flux. Though growing in intensity with increasing Ca deposition the near edge fine structures look very similar for thicknesses up to 18 Å and resemble that of CaO [129]. This supports the finding obtained from Ca $2p$ PE spectra, that all Ca atoms are in a similar chemical state for deposition rates up to 20-25 Å.

In short, NEXAFS spectroscopy confirmed significant alteration of the π^* peptide bond orbitals upon interaction of the protein layer with deposited calcium atoms. At that, the larger impact was on the C $1s \rightarrow \pi^*$ transitions. These observations are consistent with the scenario developed on the basis of the PE data.
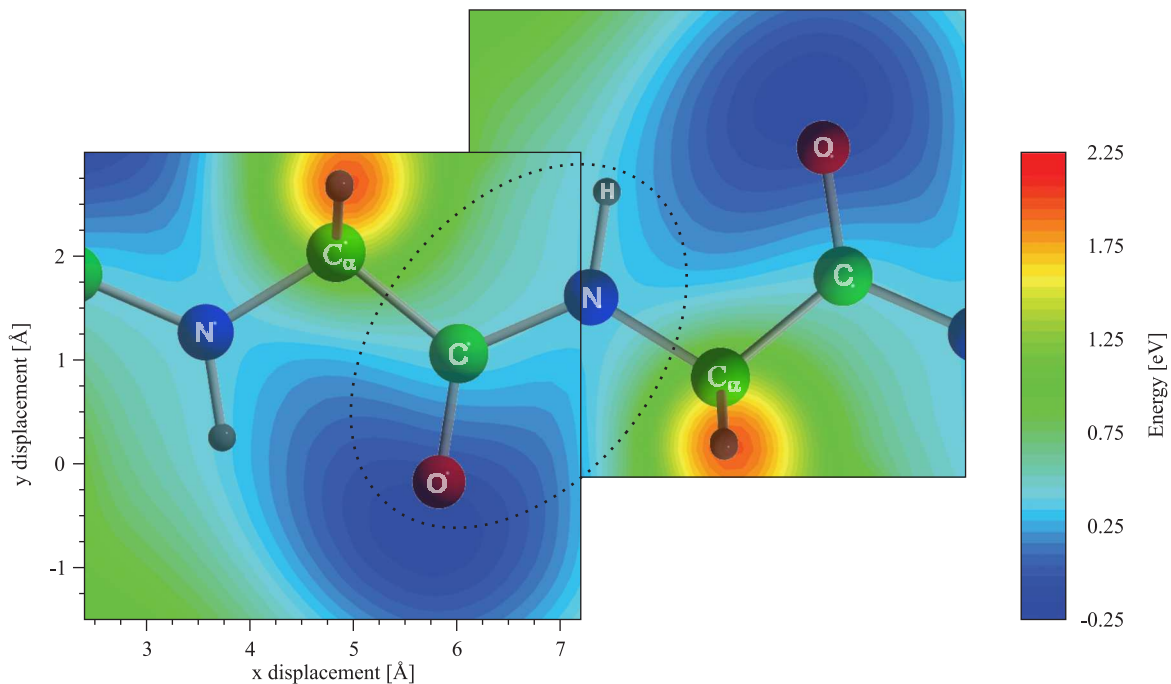
Figure 4.4: *Energy landscape of a* Ca^{0+} *atom moved across a polyglycine* β-*sheet obtained by super ab initio calculations. There is a pronounced energy minima at each oxygen atom of the peptide backbone, clearly identifying them as the binding sites of the Ca atoms.*

4.2.2   *Ab initio* calculations

To unequivocally answer the question to which particular atomic site in the peptide group the calcium atom adheres is not straight-forward. Although, core-level PE indicates that the Ca atoms bind to the oxygen site of the peptide groups and NEXAFS spectroscopy supports this scenario, there is still some speculation involved. In order to countercheck this interpretation of the experimental findings, additional supercell *ab initio* calculations were performed.

To this end, the protein was modeled assuming a poly-glycine chain in the β-sheet configuration [130, 131]. The corresponding molecular structure is shown in *Figure 4.4*. The electron system was described with the Gaussian-type all electron basis set 6-311G** [132]. Then a Ca^{0+} metal atom was moved at $z = 2.5$ Å above the beta-sheet in the x-y plane and the resulting energy landscape was calculated with the CRYSTAL code [133] using the hybrid B3LYP exchange correlation potential [134] to correct for the self-interaction error inherent in local density and generalised gradient approximations. The Ca atom was described with the TZVP basis set [135]. The grid size was 16x15 points with a step size of 0.3 eV. The results are shown in *Figure 4.4* as color-coded background. The energy scale gives the calculated energy required to dissociate the protein-Ca system
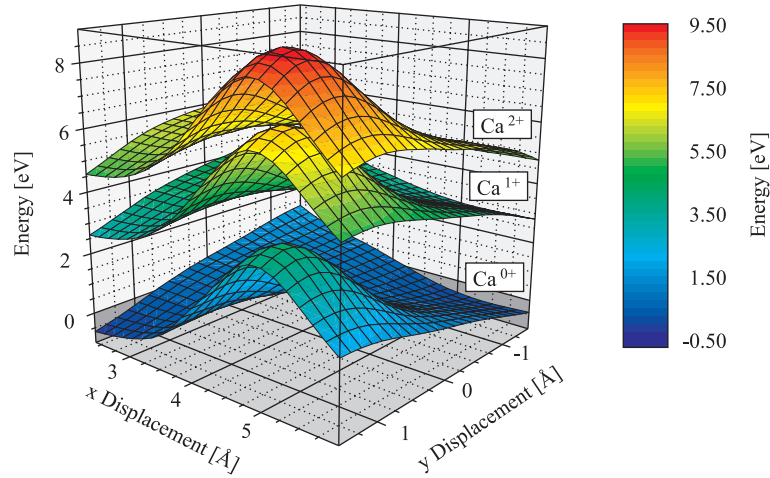
Figure 4.5: Energy landscapes for different charging states of Ca. The results for Ca^{1+} and Ca^{2+} are similar to those obtained for the neutral calcium with the energy minima at oxygen site. In contrast however, no absolute energy gain was observed for both charging states. This is in agreement with what is found in living species where any spontaneous chemical interaction between proteins and the numerously present Ca^{2+} ions would cause immediate break-down of vital biological functions.

into an individual Ca atom and the polyglycine chain:

$$E = E_{protein+Ca} - E_{protein} - E_{Ca} \qquad (4.1)$$

Calculations assuming configurations other than the β-sheet showed similar results.

Clearly visible there are pronounced energy minima at the oxygen sites of the peptide backbone. More than that, there is an absolute energy gain for the Ca-peptide system when calcium atoms bind to the oxygen atom. Thus the calculations clearly identify the oxygen atoms as the most favorable binding sites for calcium within the peptide chain. This is in agreement with what was suggested on the basis of the experimentally obtained core-level PE and NEXAFS data. Similar energy landscapes but with no absolute energy gain were obtained when replacing the neutral neutral Ca^{0+} by Ca^{1+} or Ca^{2+} cations. This is shown in Figure 4.5 where calculational results for the different charging states of Ca, i.e. 0+, 1+ and 2+, are compared.

For single-charged Ca^{1+} and double-charged $Ca^{2}+$ ions an energy gain upon chemical calcium-protein interaction was not detected for any position in the β-sheet. Note that although the shapes of the calculated energy landscapes are similar to that obtained for the neutral charging state, the curves do not touch or fall below the 0 eV energy level. This important result supports reliability of the performed calculations. In nature, spontaneous interaction of the myriad Ca^{2+} ions with proteins would lead to immediate break down of many vital functions from the neuronal down to the subcellular level, which are driven by Ca^{2+} (cf. 4.1).
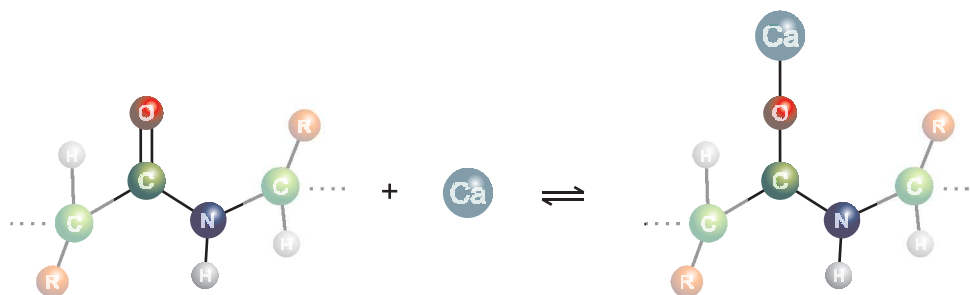
Figure 4.6: Proposed scenario of the chemical modification of the peptide bond by atomic calcium based on both experimental and theoretical data.

To conclude, both experimental as well as theoretical data revealed a strong interaction between the deposited calcium and the protein layer at which the Ca atoms attach preferably to the oxygen site of peptide units. In consequence, a significant redistribution of charge takes place. As suggested by the NEXAFS measurements the symmetry and partially double bond character of the peptide bond is broken upon Ca binding. As a consequence, the planarity of the peptide bond might be removed, too, which could cause serious modification of the protein's spatial structure. Although this cannot be concluded from the spectroscopic means applied, it would breed some serious consequence for the functionality and the unique morphology of the protein layer in particular, and any protein in contact with Ca atoms in general. The found chemical interaction between Ca atoms and the peptide backbone is summarized in the chemical equation sketched in *Figure 4.6*.

4.3 Evidence for calcium penetration into the protein layer

It is quite noteworthy, that up to 25 Å calcium deposition all recorded Ca $2p$ PE spectra showed virtually the same shape of a single spin-orbit split doublet (*Figure 4.2*). Note, that 25 Å of Ca would be sufficient to built almost five complete monolayers on a plane substrate. Hence, even taking into account the rough and crumpled surface of the protein layer with its pore structure, chemical interaction of an entire 25 Å deposit requires considerable penetration of the Ca atoms into the S layer structure. Only beyond ~ 30 Å Ca deposition the Ca $2p$ PE spectra starts to deviate from the simple doublet line shape which suggests that a critical penetration depth is reached then and no "unoccupied" oxygen sites are available in the reachable peptide units any more.

This behavior is shown in Figure 4.7 where the Ca $2p$ PE spectra for 5 Å, 38 Å and 500 Å Ca deposition are compared with each other. To this end, a least-squares fit analysis was performed on each of the three spectra the results of which are depicted along with the respective spectrum. The 5 Å spectrum is an example for the single doublet line shape
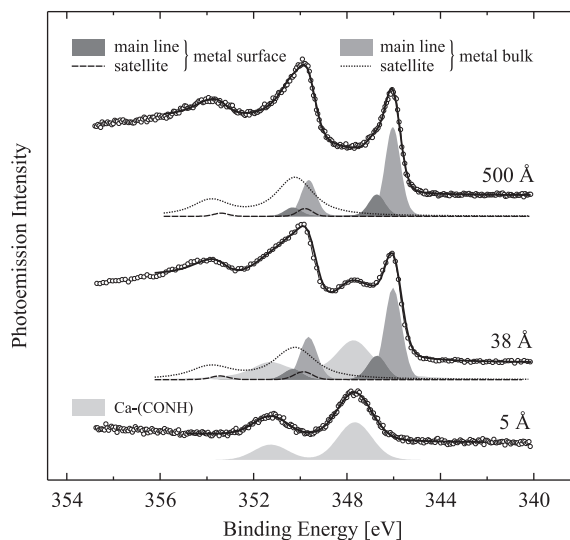
Figure 4.7: Ca 2p PE spectra observed after 5 Å, 38 Å and 500 Å Ca deposition onto the S layer. The 38 Å spectrum appears to be a mere superposition of Ca-(CONH) and Ca metal photoemission. For details see text.

observed from the lowest up to ∼30 Å Ca deposition onto the protein. This spectral shape can be readily identified with the situation that the entire deposit is bond to the individual peptide bonds according to the scenario developed above. This component is, therefore, denoted as Ca-(CONH) in the figure.

The 500 Å spectrum, on the other hand, surely contains only contributions by metallic Ca because of the high surface sensitivity of soft X-ray PE spectroscopy [97]. It exhibits a rich structure, very different from the lone doublet. Using the same $2p_{3/2}$ - $2p_{1/2}$ energy separation and intensity ratio as obtained from the least-squares fit of the 5 Å spectrum I needed at least four doublet components to achieve a convincing reproduction of the 500 Å spectrum. In detail, they can be assigned to the following characteristics of metal PE spectra: a bulk PE line at 346.0 eV BE and a narrower surface PE line at 346.7 eV, both accompanied by their corresponding metallic satellite. The energy shift of the surface PE line with respect to the bulk PE line is due to the lower coordination number of the surface Ca atoms, and is widely known as the surface core-level shift. The satellite lines are likely due to inelastic plasmon scattering of emerging photoelectrons. Since the scattering probability is much lower for surface PE, the relative intensity of the corresponding plasmon-scattered line is strongly reduced compared to the bulk PE satellite. Also, the energy separation between main and satellite line amounts to 3.1 eV for surface PE, but is 4.1 eV for bulk PE. The ratio of both agrees well with the ratio $\sqrt{2} : \sqrt{3}$ expected from the 2 and 3 degrees of freedom for collective oscillations of a 2D and 3D Fermi liquid, respectively.

In the 38 Å Ca spectrum the spectral features from both peptide-bound and metallic calcium seem to coexist. For the fit, I used the same set of components as in the 500 Å case

plus the doublet from the 5 Å case. All components were fixed in energy and line width. Also the intensity ratios between the individual metallic components was held constant. T he only free parameters were the intensity of the Ca-(CONH) doublet and the overall intensity of the set of metallic components. The obtained least-squares fit followed the experimental spectrum very well. So, obviously, the 38 Å Ca is a mere superposition of the 5 Å spectrum and the Ca metal spectrum. This suggests, that metal growth sets in abruptly at ~30 Å Ca deposition following the phase of Ca-protein interaction. At 45 Å Ca deposition (not shown) the Ca-(CONH) line is already largely suppressed and the spectrum is basically that observed for Ca metal, with only a tiny bump left at ~348 eV photon energy.

In conclusion, the deposited calcium atoms seem to penetrate deep into the protein layer to establish Ca-(CONH) bonds. Only after 30 Å Ca were deposited the protein is either "calcium saturated" and, thus, cannot provide with additional binding sites or a critical penetration depth was reached. The driving force for this directed diffusion of calcium atoms into the protein layer may be interpreted as a chemical gradient between calcium-modified and native parts of the layer.

4.4 Chemical kinetics of the metal binding reaction

Both experimental and theoretical data so far revealed a strong chemical interaction between atomic calcium and the protein layer. However, a comprehensive characterization of a chemical reaction does not merely require identification of the chemical reactants, the underlying reaction equation and the driving energetics as it was done until here. The key information on the mechanism, progression and rapidness of a reaction is given only with the description of its chemical kinetics [136]. In this section, I want to access this information using time-dependent PE spectroscopy. In particular, I concentrated on the valence band (VB) photoemission because in contrast to core-level PE it is not element-selective but allows to monitor contributions from all chemical species simultaneously.

In *Figure 4.8a* I show the temporal evolution of the VB PE spectrum recorded at $h\nu = 100$ eV photon energy from a proteine layer after 20 Å Ca had been deposited. Note that in contrast to *Figure 4.2*, where respective Ca coverages were reached by a stepwise deposition of small amounts of Ca and deposition had been interrupted after every step in order to monitor changes in the core-level spectra, the whole amount of Ca was deposited at once here within a deposition time of 1.5 minutes. At 20 Å every deposited Ca atoms reacts with peptide bond oxygen according to what was found in 4.3. Therefore, one can expect that any observations in the recorded spectra are basically a reflection of this reaction. The presented dataset comprises the time range between 3 and 30 minutes after Ca deposition. Beyond 30 minutes no further changes were detected in the spectra. The time between 0 and 3 minutes was needed to transfer the sample from the preparation to the analysis chamber of the experimental station.
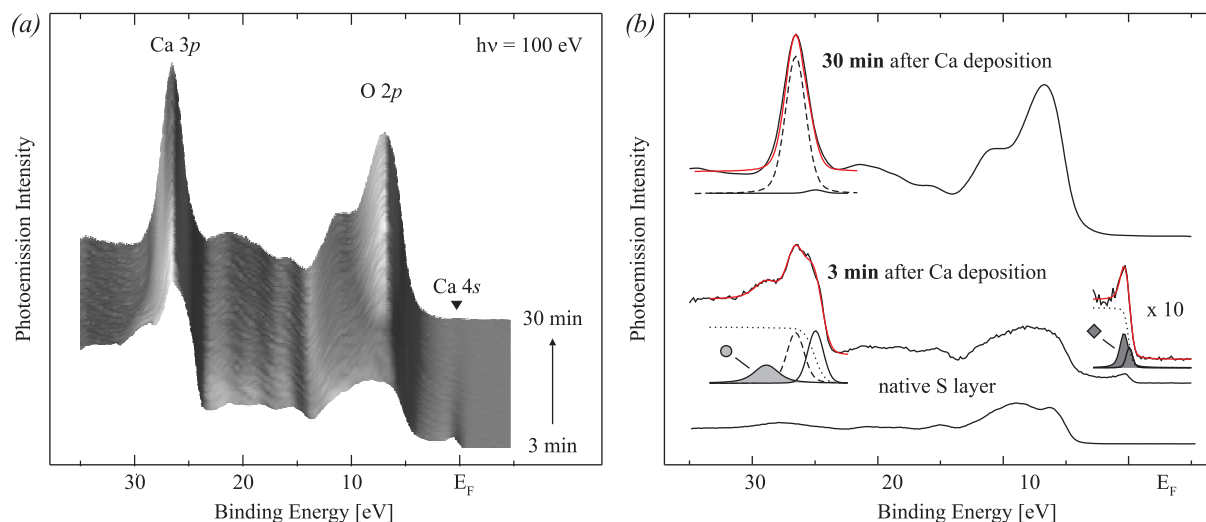
Figure 4.8: (a) Temporal evolution of the valence band PE spectrum between 3 and 30 minutes after deposition of 20 Å Ca. The most striking changes concern the Fermi energy region, the Ca 3p signal and the uprising O 2p signal. (b) Valence-band PE spectra for native S layer and 3 and 30 min after 20 Å Ca had been deposited, together with results of a fit analysis of the Ca 3p and Fermi level features. Ca-metal and Ca-(CONH) derived components are plotted with solid and dashed lines, respectively.

Having a closer look at the recorded data there are three energy regions where striking changes take place. First, shortly after Ca deposition distinct metal states show up at the Fermi level E_F which by and by vanish completely. Secondly, the shape of the Ca 3p PE line at about 27 eV BE undergoes considerable evolution. The changes are comparable to what had been observed previously when going from calcium metal to calcium oxide [128]. And thirdly, between 5 and 12 eV BE the spectrum evolves from a contour close to the native S layer spectrum [120] to a shape similar to what was found for CaO [137]. In particular, an intense component grows up around ~6.5 eV BE where commonly O 2p bonding state contributions are observed [128, 138].

Interpretation of these effects is straight-forward. Before reaction with the protein layer the unaffected Ca deposit possesses a metal electronic structure as revealed by the finite density of states at the Fermi level which derives from quasi-free Ca 4s electrons. Note, that the native protein layer exhibits a large band gap of circa 3 eV with no states at the Fermi level (bottom spectrum in *Figure 4.8b*). Upon binding to the peptide oxygens the Ca 4s electronic hybridize with the O 2p states to joint molecular orbitals, partly gaining O 2p character. Accordingly, considerable spectral weight is transfered from E_F into the region of O 2p bonding states. Because at hν = 100 eV the PE cross section of O 2p states is ~30 times larger than that of Ca 4s states [6], the growth of the ~6.5 eV feature appears disproportionally pronounced compared to the simultaneous decline in PE intensity at E_F.

As mentioned above, the transition from Ca metal to CaO-like PE can also be moni-

tored at the Ca $3p$ core-level. This becomes more apparent in *Figure 4.8b* where the 3 min and 30 min spectra are depicted along with results of a least-squares fit analysis of the Ca $3p$ peak. 30 min after Ca deposition the peak derives basically from Ca-(CONH) type calcium and can be described with a single Voigt function. In contrast, its proper fit in the 3 min spectrum requires the introduction of two additional Voigt components which must be related to metal-like Ca content. In agreement with previous studies the peak at lower BEs and the broadened peak at higher BEs than the Ca-(CONH) component can be identified with the $3p$ main line and plasmon satellite line characteristic for Ca metal, respectively [139].

Quantitative, time-dependent analysis of the intensity of the Ca-metal derived spectral fractions can grant the desired insight into the chemical kinetics of the calcium-protein interaction. To this end, the region around E_F was modeled using a room-temperature Fermi step function and two additional Voigt peaks as shown in *Figure 4.8b*. Only the intensity of the two Voigt peaks and the height of the Fermi step function served as free fitting parameters. The cumulative intensity of the two Voigt peaks was taken as a measure for Ca-metal content in the sample. In order to model the Ca $3p$ shape along the entire time the three Voigt peaks reflecting Ca-(CONH) and the Ca metal main and satellite line were fixed in linewidth and energy. Again only their intensities were allowed to vary during the fit. Intensity of the satellite line, which is well-separated from the other two lines in binding energy, was used to quantify the metallic Ca fraction.

The obtained evolutions of the Fermi signal and the Ca $3p$ satellite intensity as a function of time are shown in *Figure 4.9*. In both cases, the intensities at $t = 3$ min were set to unity. Though obtained from completely different spectral features, both curves exhibit virtually the same progression, which proves the reliability of the obtained results. Also, monitoring the height of the Fermi step or the Ca metal $3p$ main line instead, I found similar time-dependences only with slightly worse statistics.

For a proper interpretation of these curves, sufficient modeling of the chemical reaction is needed first. To this end, I assumed a one-step reaction at which the peptide bond unit and calcium react to a joint product

$$\text{CONH} + \text{Ca} \rightleftharpoons (\text{CONH+Ca})$$
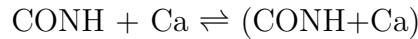
with the reaction equilibrium on the product side. Furthermore, the deposited Ca amount of 20 Å grants that all Ca atoms will undergo this reaction and at the same time a large number of unoccupied peptide bonds is still available. Please be reminded again that stable Ca metal growth sets in only beyond 30 Å. In good approximation one can therefore assume, that the generation rate r of the product (CONH+CA) depends only on the quantity of available metallic calcium [Ca], whereas the number of available peptide bonds [CONH] is no limiting factor.

$$r = \frac{d}{dt}[\text{CONH+Ca}] = k\,[\text{Ca}]$$

At that k is commonly denoted as the rate constant and the decisive factor that charac-
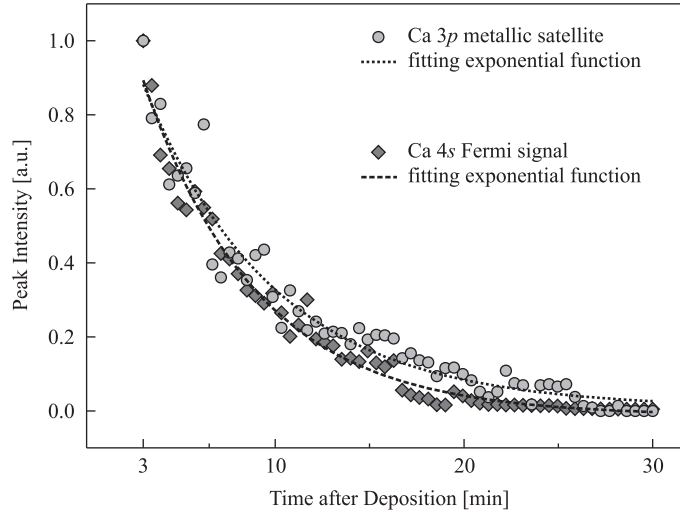
Figure 4.9: Evolution of the PE intensity of the Ca 3p satellite line and the 4s Fermi signal with time, as it was derived from a least-squares fit analysis of the spectrum in Figure 4.8. The exponential curves best fitting the data are included as thick dotted and dashed lines.

terizes the reaction kinetics. Because of the law of conservation of mass

$$r = -\frac{d}{dt}[\text{CONH}] = -\frac{d}{dt}[\text{Ca}] = \frac{d}{dt}[\text{CONH+Ca}]$$

one can rewrite this equation as

$$r = -\frac{d}{dt}[\text{Ca}] = k\,[\text{Ca}]$$

which is the general rate equation for a first order reaction. Naturally, the solution of this differential equation is an exponential function.

$$[Ca](t) = [Ca](0)\,\mathrm{e}^{-kt} + [Ca](t \rightarrow \infty) \tag{4.2}$$

Now [Ca](t) is directly correlated with the measured PE intensities curves $I(t)$ in *Figure 4.9*. Therefore, one can replace [Ca] in (4.2) with the experimentally accessible quantity, i.e. the PE intensity I, and thus obtains the following ansatz for a fit function for the $I(t)$ curves

$$I(t) = I(0)\,\mathrm{e}^{-kt} + I(t \rightarrow \infty) \tag{4.3}$$

where k is still the desired rate constant. The fit should yield $I(t \rightarrow \infty)$ close to zero if the equilibrium of the reaction lies on the product side, i.e. all Ca atoms are indeed bound by the protein in the end.

Using this equation the best fits of the experimental $I(t)$ curves in *Figure 4.9* were found with the parameters summarized in Tab. 4.1. For both curves the obtained values for the rate constant k are in convincing agreement and point to a reaction half life $T_{1/2} =$

	Fermi level	Ca $3p$ satellite
k [1/min]	0.165 ± 0.008	0.144 ± 0.012
$I(0)$	1.490 ± 0.051	1.346 ± 0.068
$I(t \to \infty)$	-0.013 ± 0.010	0.008 ± 0.018

Table 4.1: *Optimum fitting parameters for the curves in Figure 4.9b obtained with Equation (4.2).*

$\ln 2/k$ of approximately 4.5 min. Comparable to many reactions in liquids $T_{1/2}$ could be predominantly determined by the mobility of the Ca atoms which dictates how fast the Ca atoms can diffuse to the reaction centers within the protein layer. It should be stressed that rate constants are generally temperature dependent and that the given values were determined from room temperature measurements. Also, in both cases $I(t \to \infty)$ was close to zero which confirms the expectation that the reaction equilibrium and therewith the free energy minimum lie on the product side of the reaction equation.

4.5 Conclusions

In conclusion, combination of synchrotron-based PE and NEXAFS spectroscopy with *ab initio* calculations allowed to gain comprehensive inside into the interaction between individual calcium atoms and protein molecules. In particular, it was possible to identify the oxygen sites of the peptide backbones as the reaction sites where calcium binds within the protein molecule and thus severely modifies the original peptide bonds with respect to their symmetry and energetics. At that, Ca $4s$ states hybridize with O $2p$ states to joint molecular orbitals with lower overall energy. Probably driven by diffusion in a chemical gradient between already Ca-modified and still native parts of the S-layer Ca atoms penetrate deep into the protein layer until either a critical penetration depth is reached or the protein layer is entirely calcium saturated. Based on time-dependent valence band photoemission an approach to experimental determination of the kinetics of a chemical reaction was elaborated and successfully applied to determine the rate constant of the reaction between the protein-calcium reaction.

Altogether, I was able to monitor a chemical process in a complex biological systems down to the atomic scale and to obtain the relevant informations for a systematic characterization of this process.

5 Oscillator strength of the $1s \to \pi^*$ X-ray absorption resonances of the peptide bond: An approach to mapping of individual molecular orbitals

5.1 Introduction

In the preceding two chapters high-resolution X-ray photoemission and X-ray absorption spectroscopy were used to study systems composed of biomolecules on two very distinct length scales. These were on the one hand the mesoscopic scale where effects of self-organization were studied and on the other hand the scale of individual molecules and molecule moieties where interactions with single metal atoms were investigated. In both cases, the applied methods were basically employed as tools for chemical analysis for which they offer an intrinsic strength because of their elemental selectivity. This strength derives from the fact both techniques directly address the electronic states of matter, which ultimately govern chemical properties. In particular, X-ray absorption spectroscopy can often provide with fundamental insight into a molecules chemistry and structure. Numerous studies elucidated the impact of chemical bonding [21, 140, 141], bond lengths [142, 143], and collective molecule orientation [144, 20, 145, 146] on X-ray absorption properties.

Unfortunately, for most experiments only the energy position and relative weight of spectral features can be concluded from data analysis. This is because except for few experiments, which can be conducted in gas cells or on thin solid films, fundamental experimental obstacles usually prevent reliable disclosure of absolute absorption intensities. Surface adsorbed molecules, such as graphene and the here discussed biomolecule layers, or bulk materials must be studied using electron or fluorescence yield detection modes and to relate the detected yield signal to X-ray absorption cross sections is not straight-forward. But naturally, experimental determination of absolute X-ray absorption cross sections also in yield measurements is highly desirable. As will become apparent in this chapter, this would enable to advance into the most fundamental, electronic orbital scale of such systems

and to obtain, for instance, information on the topology of single molecular orbitals.

In this chapter, an approach to experimental determination of absolute X-ray absorption cross sections will be elaborated and tested at the example of a crystalline protein surface layer adsorbed to a solid state surface. In doing so, the X-ray absorption properties of proteins are going to be described quantitatively, for the first time. In particular, oscillator strengths of the $1s \rightarrow \pi^*$ transitions within the peptide group could be measured and used to draw a rough map of the $\pi^*_{peptide}$ orbital topology. This experimentally deduced orbital topology will be compared with results of *ab initio* calculations.

The investigated protein layer was an ideal candidate to test the elaborated approach, because it comes along with all the fundamental problems which one has to face in yield measurements of surface-adsorbed molecules. A complex molecule structure and arbitrary absorption of the crystalline sheets prevent an estimation of the number of probed absorption centers. It is, furthermore, not known to which extend the locally generated electron yield will be detectable and to which extend it has already been attenuated within the sample. Finally, the yield derived from the molecule top-layer must somehow be separated from the signal of the substrate underneath.

5.2 Characterization and refinement of the beamline photon flux

5.2.1 Beam monochromatization

In XAS the absorption of X-rays by a sample is measured as function of the energy of the incident photons. For this purpose, tunable photon energy is required. At the Russian-German beamline (RGBL) where the here presented XAS spectra were recorded this is achieved by means of plane-grating monochromator (PGM) [147] which allows for a resolving power of $E/\Delta E \geq 10\,000$ in the photon energy range between 100 and 600 eV. This energy range covers the relevant C $1s$ ($\sim$290 eV), N $1s$ ($\sim$400 eV) and O $1s$ ($\sim$535 eV) absorption edges making the RGBL highly suitable for measurements of organic molecules.

In spite of a very high degree of monochromatization, X-ray radiation delivered by the RGBL still contains non-monochromatic contributions, i.e. wavelengths deviating from that given by the monochromator settings. This is mainly due to parasitic light passing the plane-grating monochromator in higher diffraction orders, i.e. essentially 2nd order light, and to a minor, commonly negligible extent also by scattered light of long wavelengths (stray radiation):

$$\Phi = \Phi_{h\nu} + \Phi_{2h\nu} + \Phi_{3h\nu} + \ldots + \Phi_{stray} \approx \Phi_{h\nu} + \Phi_{2h\nu} \qquad (5.1)$$

where $h\nu$ denotes the first-order photon energy set with the monochromator. In *Figure*
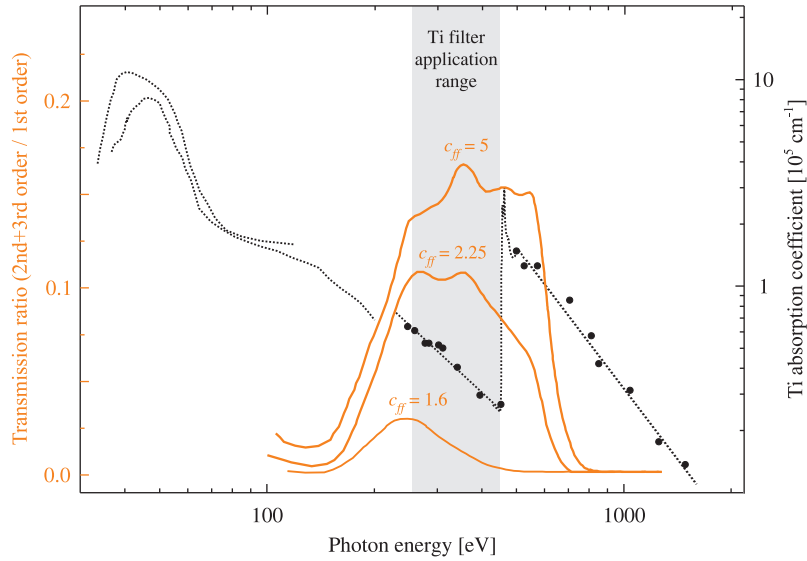
Figure 5.1: *Calculated transmission ratio of higher-order to first-order light at the RGBL as a function of photon energy and for different fixed-focus values c_{ff} (orange lines). The black dotted line shows the absorption coefficient of titanium (data taken from [149, 10, 150, 151]).*

5.1 the calculated transmission ratio, i.e. the ratio between high-order and first-order light, of the RGBL is shown as a function of photon energy and for different fixed-focus constants c_{ff}. Although, at $c_{ff} = 1.6$ non-monochromatic fractions of the photon beam are suppressed best, working in this setting is often disadvantageous because c_{ff} does not only define the transmission ratio but also photon flux and resolving power of the beamline. While the former increases for lower c_{ff} values the latter significantly drops [148]. The best trade-off is in most cases achieved at $c_{ff} = 2.25$ which was also chosen for the present study.

In this setting, however, the percentage of high-order light easily reaches more than 10% in the relevant photon energy range of 200-600 eV. Therefore, XAS spectra taken in this energy window would always include undesired non-monochromatic contributions which are difficult to specify and almost impossible to separate from the desired signal. The easiest and most reliable way to suppress these contributions is to remove 2nd-order light right from the start. To this end, an appropriate filter could be mounted between beamline and experimental chamber that highly transmits the desired wave-lengths but blocks undesired 2nd and higher order light. After traversing the filter the photon beam would be much refined in terms of monochromatisity as compared to (5.1):

$$\Phi_{filter} \quad = \Phi_{h\nu} \cdot \mathrm{e}^{-\lambda(h\nu)\,d} + \Phi_{2h\nu} \cdot \mathrm{e}^{-\lambda(2h\nu)\,d} \underbrace{\quad\cong\quad}_{\lambda(2h\nu)\gg\lambda(h\nu),\ \Phi_{2h\nu}\ll\Phi_{h\nu}} \Phi_{h\nu} \cdot \mathrm{e}^{-\lambda(h\nu)\,d} \qquad (5.2)$$

with λ the energy-dependent absorption coefficient and d the thickness of the filter material.

For large parts of the desired photon energy window the condition $\lambda(2h\nu) \gg \lambda(h\nu)$ can
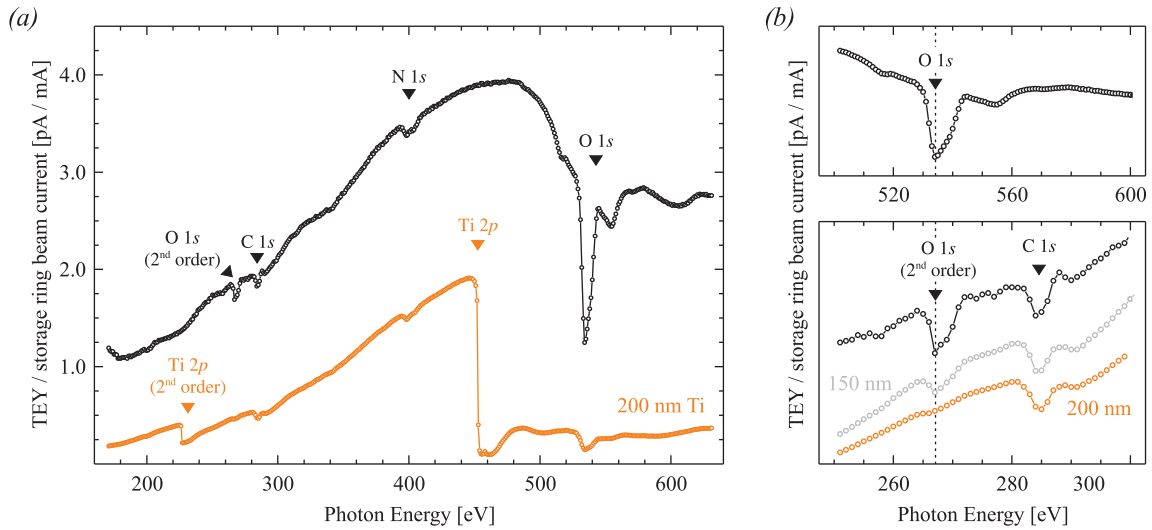
Figure 5.2: (a) X-ray absorption curves taken from a clean gold plate in total electron yield mode after normalization to the storage ring beam current. The black and orange curve were recorded without and with the 200 nm Ti filter, respectively. C, N and O 1s derived dips show up in the spectra which are due to contamination of the optical elements of the beamline. (b) Without Ti filter a pronounced second-order copy of the O 1s feature at 267 eV photon energy is detected. It disappears when the 200 nm filter is introduced into the optical path, indicating the the filter effectively removes non-monochromatic fractions of the beam within its working range between 225 and 450 eV. A 150 nm filter, however, was not effectually thick.

be fulfilled by application of a titanium filter. This is easily seen in *Figure 5.1* where the energy dependent absorption coefficient λ is included as a black, dotted lines. Evidently, Ti shows high absorption in the photon energy ranges 10-100 eV and 450-900 eV and at the same time good transmission between 225 and 450 eV [149, 10, 150, 151]. Therefore, by application of a Ti filter of appropriate thickness one may obtain an almost perfectly monochromatic photon beam in the energy range of the C 1s and N 1s absorption edges between 250 and 450 eV. Moreover, long-wavelength stray radiation could also be suppressed by virtue of the high absorption at very low photon energies.

For the present measurements a removable Ti filter, prepared in the form of a free-standing, 200 nm thin film, was mounted between the RGBL and the experimental end-station. The importance of this experimental measure becomes clear when looking at *Figure 5.2*: In panel *(a)* the total electron yield (TEY) signal of a pristine Au film is hsown which had been thoroughly cleaned by Ar sputtering. The black XAS curve was recorded when the filter was removed from the optical path and the orange curve with applied filter. Both curves reveal dips around the C 1s, N 1s, and O 1s absorption edge due to respective contaminations on the optical elements of the beamline which absorb part of the passing photon flux. This effect is particularly pronounced at the oxygen edge where intensity partly drops by almost 50%. In case that the Ti filter is applied the TEY signal additionally exhibits the expected massive break-down in intensity when the Ti 2p

absorption edge is crossed at 450 eV photon energy, plus a less intense 2nd-order copy at 225 eV.

Closely below the C $1s$ absorption edge another dip is observed for the black curve at ~267 eV. This feature represents the 2nd order replica of the pronounced O $1s$ structure at 2×267 eV=534 eV. It is shown again in *Figure 5.2b* together with the respective, first-order region. Note, that the photon energies in the upper scale are twice as large as in the lower scale, aligning both first and second order structures to each other. After the 200 nm Ti filter had been introduced into the optical path (orange curve) the second-order imprint of the O $1s$ region basically vanished from the spectrum. This shows that the filter is sufficiently thick to block large parts of the 2nd order light. In contrast, when changing to an likewise prepared, but only 150 nm thick Ti filter part of the 2nd order feature still remained.

The pronounced 2nd-order imprints of the O $1s$ and Ti $2p$ absorption edge structures in the XAS curves of the Au film give already an impression why suppression of non-monochromatic fractions in the photon beam is essential. Note that in samples other than Au where intense absorption edges fall into the energy range of the 2nd order radiation the corrupting effect on the XAS spectrum would be disproportionately higher. In the case of proteins, this particularly applies to 2nd-order O $1s$ excitations (260-295 eV photon energy) which partly interfere with the first-order C $1s$ excitation energy range (280-330 eV). The presented Au spectra unambiguously show that the produced 200 nm Ti filter can reliably prevent those effects in the energy range between 225 and 450 eV. All further presented XAS spectra had been recorded with the filter applied ensuring an almost perfectly monochromatic photon beam.

5.2.2 Photon flux

In the total electron yield detection mode, the X-ray absorption induced total photoionization of a sample is measured by detecting the number of electrons emitted by the sample. According to 2.2.3 the TEY J is given by

$$J(h\nu) = MY\rho\eta \times \sigma(h\nu) \times \Phi(h\nu) \quad \propto \quad \sigma(h\nu) \times \Phi(h\nu) \tag{5.3}$$

with σ the X-ray absorption cross section, Φ the incident photon flux and $MY\rho\eta$ approximately constant for a given sample (cf. 2.2.3). Therefore, in order to relate a detected TEY signal to the X-ray absorption cross section of a sample Φ must be characterized properly as a function of photon energy $h\nu$.

The photon flux of the RGBL upgraded with the Ti filter was determined using the TEY signal recorded from the clean Au film and has already been shown in Figure 5.2. On the basis of this curve the photon flux $\Phi(h\nu)$ can be estimated using (5.3) and calculated
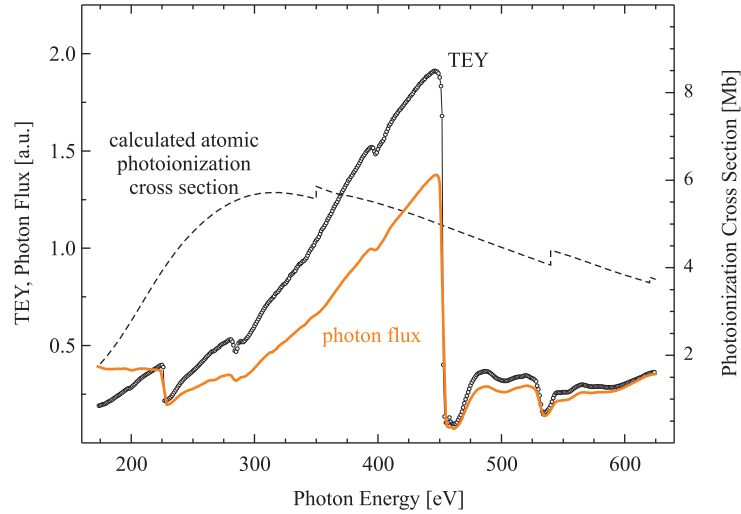
Figure 5.3: Photon-energy dependent TEY signal taken from a gold plate (circles) along with the calculated atomic photoionization cross section σ^* of gold (dashed line). The orange line shows the resulting photon flux curve of the RGBL derived with the help of (5.4).

values of the atomic photoionization cross sections $\sigma^*_{Au}(h\nu)$ [6]:

$$\Phi(h\nu) \propto \frac{J_{Au}(h\nu)}{\sigma^*_{Au}(h\nu)} \tag{5.4}$$

However, the calculated σ^* values describe the actual cross sections σ reliably only for photon energies far away from pronounced absorption edges because they do not consider transitions into localized final states that are responsible for the near-edge fine structures. Instead absorption thresholds are simply described by step functions [14, 6]. In the photon energy range of interest for this study, i.e. between 200 and 600 eV, Au has no intense absorption edges and the total cross section σ_{Au} basically derives from $4f$ excitations with the $4f$ threshold far below at ∼90 eV photon energy.

Figure 5.3 shows the TEY curve obtained from the gold plate (circles) along with σ^*_{Au} (dashed line) and the resulting quotient of both (orange line). As discussed, both the measured curve as well as the calculated cross sections do not reveal intense absorption edges and run rather smoothly in the probed photon energy range. Hence, application of (5.4) is possible and the orange curve directly characterizes the energy-dependent photon flux delivered by the RGBL.

Having characterized the photon beam properties of the RGBL and removed its non-monochromatic fractions one can now start to analyze the X-ray absorption spectra obtained from the protein sample.
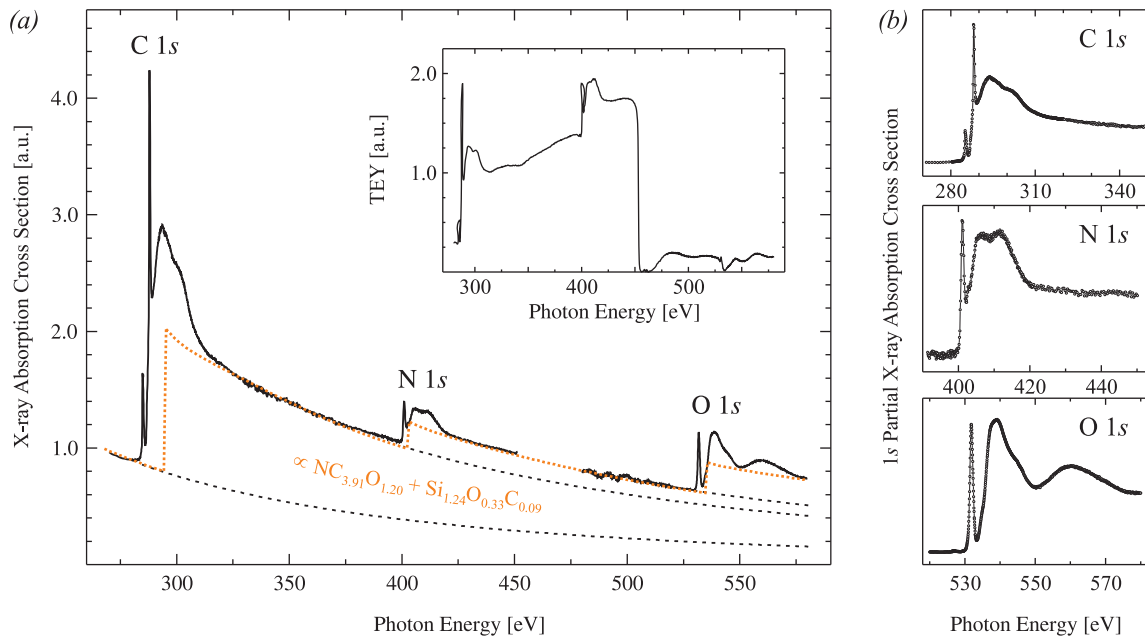
Figure 5.4: (a) Photon-energy dependent X-ray absorption of the protein layer adsorbed to a SiO$_x$ substrate obtained by TEY detection and subsequent normalization to the incident photon flux. The inset shows the raw TEY signal. Dashed lines denote the extrapolated tails of lower lying absorption edges. Note that the positions of the continuum steps are taken from the atomic calculations and can differ to those found experimentally. This, however, is of no relevance for further data analysis. (b) C, N and O 1s edge partial absorption spectra obtained after subtraction of contributions by lower lying absorption edges.

5.3 Spectral dependence of the X-ray absorption of proteins

The spectral dependence of the X-ray absorption by the joint system of protein layer and underlying SiO$_x$ substrate is shown in *Figure 5.4a*. It was obtained by weighting the measured TEY signal, which is shown in the inset, with the incident photon flux delivered by the beamline. The curve reveals distinct step-like jumps in intensity when the photon energy is tuned across the C, N and O 1s edges. Each jump is accompanied by a pronounced near-edge fine structure which transforms into a monotonically descending tail when moving in photon energy further away from the edge. As discussed in 2.2.2 the fine structure is due to numerous transitions of 1s electrons into unoccupied molecular electronic states, whereas the structureless tail reflects excitations into continuum states far above the vacuum level. The partial cross section of each absorption edge can be extracted by subtracting tails originating from lower lying absorption edges. This is shown in *Figure 5.4b* for the relevant C, N and O 1s absorption edges.

Strictly speaking the displayed, TEY-derived curves can be considered as a replica of

the X-ray absorption cross section σ only if the assumed direct proportionality between flux-normalized TEY and σ in (5.3) is correct. Although there is some evidence for a close similarity between electron yield and X-ray absorption [27], this cannot be taken as granted from the beginning, particularly since comprehensive studies on this point are still lacking. Inelastic scattering of X-ray absorption derived primary electrons, for instance, might generate a considerable fraction of secondary electrons to an extent defined by scattering probabilities. Since the probability for scattering processes grows monotonically with the kinetic energies of the electrons involved, this could lead to a energy dependent multiplication of the electron yield [27]. As a result, a considerable, photon-energy dependent deviation between electron yield and X-ray absorption could possibly arise in some cases.

Such effects, however, do not seem to occur for the present sample. Instead, the data indicate a direct scaling between the curve in *Figure 5.4a* and the total X-ray absorption cross section of the sample. It was possible to reproduce all steps and continuum tails of the experimental spectrum over the entire photon energy window probed, by using again the calculated atomic photoionization cross sections σ^* [6]. In detail, I set up the following function to describe the experimentally obtained X-ray absorption cross section σ

$$\sigma^* = C \times \sigma_N^* \times x\,\sigma_C^* \times y\,\sigma_O \times z\,\sigma_{Si}^* \tag{5.5}$$

with x, y, z the relative weights of the calculated carbon, oxygen and silicon cross sections, respectively, setting the weight of σ_N^* to unity. C is a scaling constant that adopts the unnormalized experimental data to the absolute scale of the cross sections. Note, that the above function σ^* corresponds to the calculated atomic cross section of a compound $N\,C_x O_y Si_z$, as which the protein layer on the SiO_x substrate can be considered.

The best agreement between the experimental σ and the calculated σ^* was found when weighting the cross sections with an average atomic composition of $NC_{4.0}O_{1.53}Si_{1.24}$. The resulting σ^* is included in *Figure 5.4a* as a dotted, orange line. In the region of the continuum tails where the atomic calculations are expected to hold validity it follows strictly the experimental curve. This finding allows two important conclusions:

1. First and foremost, it rules out a noticeable energy dependence of electron multiplication effects in the considered soft X-ray range, which might have broken the strict proportionality between X-ray absorption and electron yield. Otherwise the slope of the continuum tails would have become flatter with growing photon energies, because of the interference of a monotonically increasing background [27]. As a consequence, the curve could not be reproduced by atomic cross sections, at least not in the entire energy range.

2. The obtained average atomic composition $NC_{4.0}O_{1.53}Si_{1.24}$ is in astonishing agreement with the chemical composition of the S layer protein ($NC_{3.9}O_{1.2}$), assuming that the remaining $C_{0.1}O_{0.33}Si_{1.24}$ reflects the contributions of the SiO_x substrate. The small contribution of carbon to the substrate signal may derive from the uncertainty

accompanied to the adjustment of σ^* to σ. However, I assume that it is due to a real substrate contribution. Repeating measurements on the blank SiO_x substrates I found a tiny signal at the C 1s edge with an intensity less than 4% compared to that after protein deposition.

Both items confirm that the experimental curve in Figure 5.4, which was derived as the flux-normalized TEY signal, shows indeed the true spectral dependence of the X-ray absorption of the protein layer on the SiO_x surface in the considered soft X-ray energy range. It should be emphasized that a fully monochromatized beam, and therewith the Ti filter beamline upgrade, were an absolutely necessary precondition to this achievement.

One should also mention that so-called saturation effects, which are observed when the effective X-ray penetration depth becomes comparable to the electron escape depth, can also preclude quantitative analysis of electron yield spectra [152]. In the present case where 1s absorption by light elements is considered these effects are negligible. They can, however, become severe when 2p edges of transition metals are involved.

5.4 Fine structure of the 1s X-ray absorption edges in proteins

Until here, analysis of the XAS spectrum was focused on its continuum tails and distinct steps, i.e. the atomic properties of X-ray absorption. This part of the spectrum would have been virtually the same for any given compound of equal chemical composition $NC_{4.0}O_{1.53}Si_{1.24}$. The part of the spectrum which will notably differ for different compounds is the near-edge fine structure. It is caused by transitions into unoccupied bound and quasi-bound electronic states and, therefore, reflects the molecular properties of X-ray absorption. Since I seek for the spectral features explicitly related to proteins these fine-structures are of particular importance for this study. In this section I will discuss the relevant C, N and O 1s NEXAFS regions of the spectrum in detail and try to identify those features which are characteristic for proteins.

5.4.1 N 1s absorption edge

The NEXAFS region of the N 1s absorption edge is shown in Figure 5.5. Since no traces of nitrogen were found on the blank SiO_x it fully originates from N 1s photoexcitations within the protein layer. In order to gain deeper insight into the spectral shape I analyzed it by means of a least-squares fit analysis. The spectrum reveals an intense, rather narrow resonance at 401.3 eV photon energy which can be assigned to a 1s$\rightarrow \pi^*$ excitation by virtue of the long final-state life time. Additionally, there is broad structure in the σ^* region at
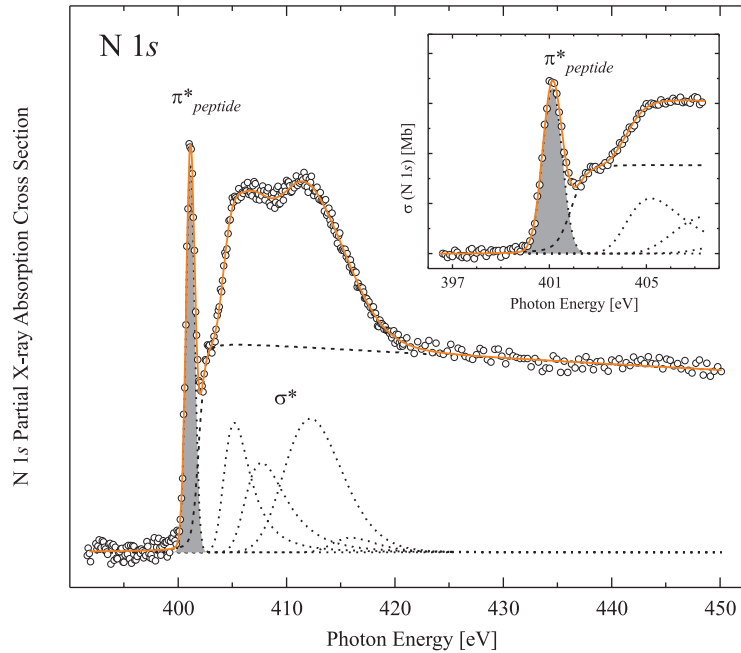
Figure 5.5: N 1s partial X-ray absorption cross section in the NEXAFS region until ∼420 eV and beyond. The spectrum reveals a sharp resonance at 401.3 eV, which reflects transitions into the peptide bond $\pi^*_{peptide}$ orbital, plus additional structure in the σ^* region. Spectral deconvolution in the framework of a least-squares fit analysis enables to determine the relative intensity of the $\pi^*_{peptide}$ peak.

higher photon energies. Similar spectral shapes have been observed in a number of previous studies of this particular protein layer [125, 153] and also other proteins [23, 154, 155, 156].

A comprehensive experimental and theoretical study of Glycine (Gly), Diglycine and Triglycine unambiguously demonstrated that the observed intense π^* resonance appears only after two or more amino acids mate to a polypeptide chain [155] and is therefore an intrinsic spectral feature of the newly formed peptide bond. When considering N 1s NEXAFS spectra of isolated amino acids [157], only few of them show intensity in the π^* region. Amide groups ($CONH_2$) in Asparagine (Asn) and Glutamine (Gln) give rise to a π^* peak at 400.7 eV. Furthermore, Histidine (His), Tryptophan (Trp) and Arginine (Arg) feature π^* resonances which were attributed to the presence of either planar aromatic structures (His, Trp) or guanidine groups (Arg) in the side chains. However, the number of these amino acids in the S layer molecule is ∼10 times smaller than the number of peptide bonds [126]. Also, the energy positions of these amino acid resonances differ from that observed here, which in turn agrees well with that in previous reports on N 1s spectra of proteins [156, 23, 154, 158]. Hence it is reasonable to assume that the π^* resonance in *Figure 5.5* reflects in largest part N 1s → $\pi^*_{peptide}$ transitions within the peptide group.

In order to get a quantitative estimate of the $\pi^*_{peptide}$ intensity, which is needed further below, I performed a least-squares fit analysis. At this, the π^* line shape was modeled with
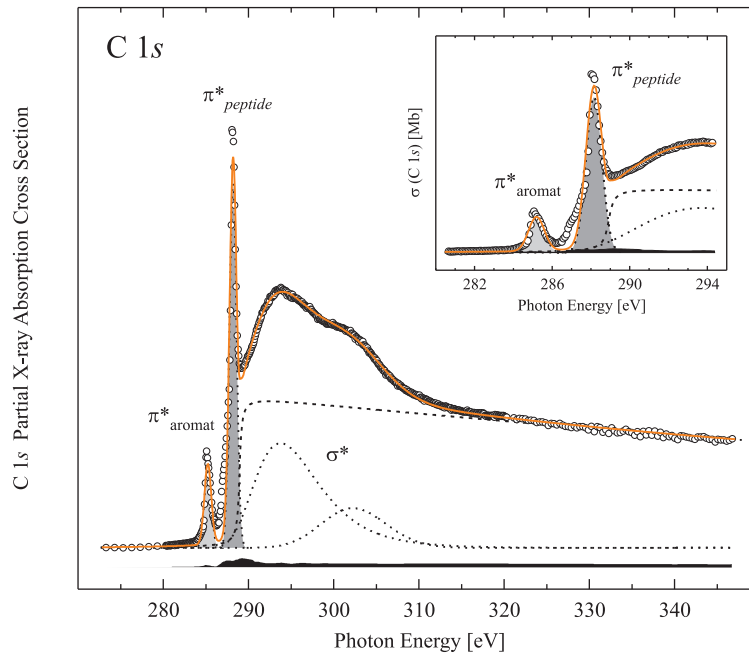
Figure 5.6: *C 1s derived part of the protein absorption spectrum covering the entire NEXAFS region and results of a least-squares fit analysis. The two sharp π^* resonances at 288.1 eV and 285.0 eV reflect $1s\to\pi^*$ transitions within the peptide backbone and aromatic protein side chains, respectively. The tiny black-shaded area at the bottom shows the respective C 1s absorption caused by substrate contaminations.*

a Voigt function, i.e. a Lorentz function convoluted with a Gaussian accounting for the finite energy resolution of the beamline. The σ^* region was described using four asymmetric Gaussian lineshapes. For the step an inverse tangents function was applied assuming a rather life-time than resolution limited shape [14]. The results of the analysis are included into *Figure 5.5*. Obviously, π^* and σ^* resonances do not interfere significantly, which could have possibly complicated the fit analysis. Therefore, the relative spectral intensity of the $\pi^*_{peptide}$ peak could be readily determined as the area below the fitting Voigt function.

5.4.2 C 1s absorption edge

Figure 5.6 depicts the fine structure of the C 1s absorption edge of the sample. The black-shaded area at the bottom of the panel shows the expected substrate contributions to the spectrum which were estimated by taking the spectrum from a blank SiO_x wafer. Because of their extremely low relative intensity (less than 4%) the measured sample spectrum can be entirely ascribed to the substrate-covering protein layer.

The spectrum reveals manifold structure in the NEXAFS region which comprises two narrow π^* resonances at 285.0 eV and 288.1 eV and additional resonances in the range

of $1s \rightarrow \sigma^*$ excitations. For assignment of the two striking resonances in the π^* range I can refer to the comprehensive experimental and theoretical studies published previously [23, 153, 154, 155, 157, 159, 160, 161].

Surely, the 285.0 eV π^* resonance can be ascribed to aromatic structures because it is observed only for amino acids characterized by an aromatic side chain, i.e. Phe, Trp, and Tyr [157]. A spectral feature, which is in contrast found for all amino acids when measured as isolated molecules, is an intense π^* peak at $\sim$288.5 eV. Hence it must reflect excitations within their common structural element, the carboxyl group COO^-. When amino acids join to form a protein these groups are transformed into part of the peptide backbone which comes along with a well-documented red shift of their C $1s \rightarrow \pi^*$ resonance by $\sim$0.4 eV [141, 155, 23]. Accordingly, the experimental spectrum features the expected intense C $1s \rightarrow \pi^*_{peptide}$ excitation peak at 288.1 eV photon energy.

It should be mentioned, that beyond the discussed spectral features isolated amino acids can feature additional π^* resonances depending on their particular side chains. For instance, those amino acids with COO^- or $CONH_2$ groups in their side chains show an enhanced 288.5 eV peak as compared to those amino acids without. Also, some other side chains show up π^* resonances at excitation energies between 286 and 287.5 eV [157]. However, in all these cases the energy position of the respective π^* resonances should stay fixed when the amino acids join to a protein, because the structure of the side chains remains unaffected during the formation of the peptide backbone. Therefore, possible side chain π^* resonances would not contribute to the 288.1 eV peak, but should appear at other photon energies.

Similar to the N 1s spectrum, a least-squares fit analysis was performed on the C 1s spectrum in order to extract information on the relative intensity of the $\pi^*_{peptide}$ resonance. The result is shown along with the experimental spectrum (*Figure 5.6*). At 286-287.5 eV and in a narrow window around 289 eV the fit notably deviates from the data points. This is most likely because, apart from the π^*_{aromat} excitations, the discussed π^* excitations in the protein side chains were not included into the fit, in order to keep the set of fitting parameters small. Absorption in the photon energy window of these resonances must hence be underestimated.

5.4.3   O 1s absorption edge

The O $1s$ NEXAFS spectrum is depicted in Figure 5.7. It shows a rather broad, though intense π^* peak at 531.8 eV which is typical for protein spectra [154, 23]. Above the ionization threshold there is additional structure due to intense $1s \rightarrow \sigma^*$ contributions. While analysis of the N 1s and C 1s NEXAFS regions were straight-forward, interpretation of the O $1s$ derived part of the XAS spectrum is complicated by several reasons.

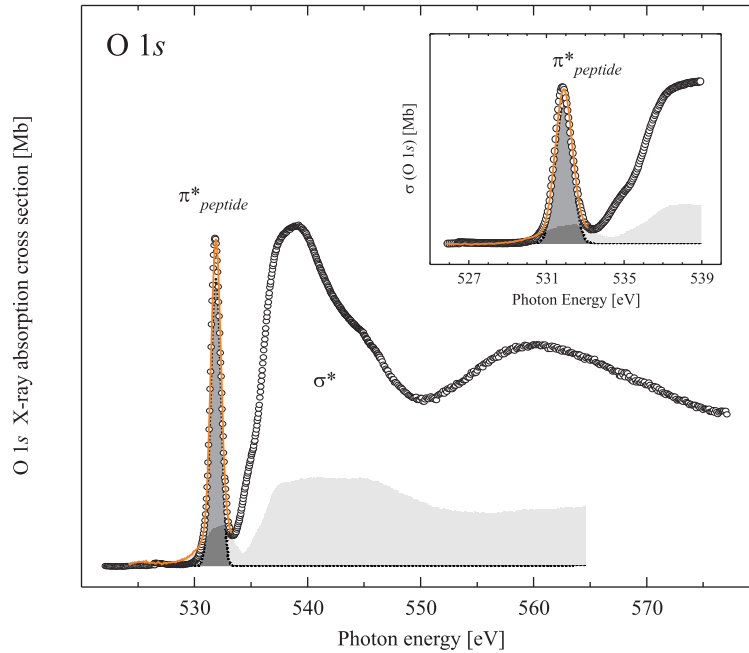First, the spectrum contains significant contributions by the SiO_x substrate which must

Figure 5.7: O 1s excitation derived part of the sample XAS spectrum. The spectrum contains contributions of both the protein overlayer and the SiO_x substrate. The latter has been estimated by scaling the signal from a blank SiO_x wafer to the expected intensity of 22% relative to the sample spectrum (light-grey area). The difference spectrum was used for fit analysis of the $\pi^*_{peptide}$ feature.

not be neglected. According to the analysis in 5.3 the substrate signal $(C_{0.1}O_{0.33}Si_{1.24})$ holds 22% of the overall oxygen intensity $(NC_{4.0}O_{1.53}Si_{1.24})$, corresponding to $y = 0.33/y = 1.53$. In order to separate substrate contributions and extract the O 1s signal of the pristine protein layer I took the O 1s spectrum from a blank SiO_x wafer and downscaled it until it corresponded to 22% intensity of the sample signal in the continuum tail region. The resulting background spectrum is shown in Figure 5.7 as the light-grey area below the data points. It shows both intensity below and above the ionization potential, in particular, a very broad peak at ~532 eV interfering with the sharp $\pi^*_{peptide}$ resonance. The difference spectrum between total signal and substrate signal (not shown) should correspond well to the X-ray absorption of the pristine protein layer. There one finds that the sharp $\pi^*_{peptide}$ resonance is fully separated from the rest of the spectrum. Therefore, I restricted the fit-analysis of the spectrum to this small energy window, using only a single peak of Gaussian lineshape. The result is included into *Figure 5.7*.

Secondly, because of the limited working range of the Ti filter (225-450 eV), non-monochromatic fractions of the incident photon beam are no longer suppressed in the region of O 1s excitations. Therefore, the detected electron yield might be partly generated by second-order light. This problem could be overcome by introduction of a second filter made of a different material that works between 450 and 600 eV, e.g. chromium. This

solution, however, was not considered practical because two simultaneously applied filters would lower the only moderate photon flux of the RGBL too much, leading to unreasonably long spectrum acquisition times. After all, the impact of second-order light in this photon energy region should be rather low in the considered case: On the one hand, the sample does not possess any absorption edge in the second-order energy range, i.e. 900-1200 eV, that could interfere with the desired 450-600 eV region. Also the absorption cross section of the contained elements is generally low between 900-1200 eV [6]. Hence, maximum a tiny and structureless background could be generated by second-order light. On the other hand, as compared to the C 1s NEXAFS range the percentage of second-order light is reduced by ∼50% in the O 1s range (cf. *Figure 5.1*).

As a third point, even in their isolated form, prior to peptide bond formation, all amino acids reveal strong π^* resonances [157]. However, there is much evidence tha, after being assembled into a protein structure only the amino acid side chains of Asparagine and Glutamine further on contribute to this peak whereas the main share of about 90% is now hold by the formed peptide units [130].

In summary, although these three complications make the analysis of the O 1s NEXAFS spectrum more imprecise, they can principally be accounted for. I therefore conclude that the sought information, in particular the relative intensity of $\pi^*_{peptide}$ resonance, can be taken as reasonably reliable.

5.5 Absolute X-ray absorption cross sections and oscillator strengths

As discussed in the introduction to this chapter relating measured yield signals to absolute X-ray absorption cross sections is a main obstacle in the analysis of XAS spectra. Although the direct proportionality between the experimental total electron yield-derived spectrum and X-ray absorption cross sections has been demonstrated in the present study, the problem remains how to rescale the experimental spectrum to absolute cross sections, measured in terms of Mb. This issue shall be addressed here with the aim to determine the oscillator strength of the 1s→ $\pi^*_{peptide}$ resonances, that are the characteristics of protein NEXAFS spectra.

5.5.1 Normalization to the absolute scale

A normalization of XAS spectra in the near-edge region is almost impossible, due to the multitude of resonances with unknown excitation probability. There have been some attempts in the past to apply a shell-adapted Thomas-Reiche-Kuhn sum rule which was first introduced by Fano and Cooper [16]. Using this sum rule it would be possible to
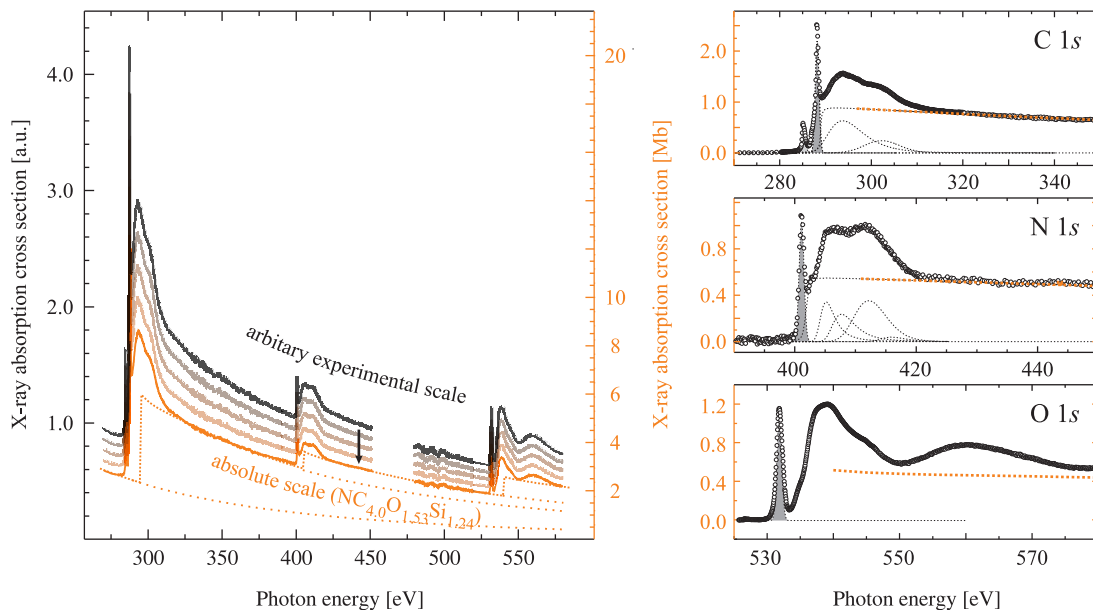
Figure 5.8: *Normalization of the XAS spectrum to absolute X-ray absorption cross sections by adapting it to calculated atomic cross sections in the region of the continuum tails. Partial 1s cross sections, which are shown in the right panels, can be obtained by either extracting them from the normalized XAS spectrum directly, or by relating the curves presented in Figures 5.4b, 5.5-5.7 to calculated partial 1s cross sections (dotted, orange lines).*

use experimental results from gas cell measurements of the simplest molecules, like N_2, O_2 or CO_2, to scale any N, O or C 1s spectrum, no matter in which detection mode it had been acquired [16, 162, 163]. However, this sum rule relies on the strict assumption that the density of unoccupied molecular states is constant regardless of the chemical bonding of the excited atom. This becomes unsustainable as soon as one accounts for the differing valence electron number for different elements, which results in a different number and filling of the molecular states. This practical inapplicability of the sum rule becomes immediately apparent upon comparing, for instance, CH_4 and CO_2 spectra derived from gas-cell measurements [163]. It seems, therefore, advisable to use the atomic rather than the molecular contributions in XAS spectra for normalization. As mentioned before in 5.3 the continuum tail as well as the step heights of the absorption edges are similar for any atom independent on its chemical bonding.

I propose to rescale the experimental spectra to absolute cross sections by using the experimentally confirmed calculations of atomic photoionization cross sections [6]. Considering once more equation (5.5) it becomes obvious that, to this end, only the scaling constant C which moderates between the absolute scale and the arbitrary scale of the experiment must be determined accurately. In doing so, I was able to relate the XAS spectrum to absolute units as shown in the left panel of *Figure 5.8*. From that, the partial 1s cross sections can be obtained by subtracting the continuum tails of lower lying

edges and subsequent division by the respective weighting factors x, y or z obtained from equation (5.5), i.e. 4.0, 1.55, and 1.24, respectively. Equally, the latter can be determined by first extracting the partial C, N and O $1s$ contributions from the XAS spectrum, like it was done for the discussion of the fine structures (cf. *Figures 5.4b, 5.5-5.7*), and then normalizing them to the calculated partial $1s$ cross sections. Both methods led to similar results, which are shown for the latter method in the right panels of *Figure 5.8*.

It should be noted, that the normalization was done with the help of calculated atomic *photoionization* cross sections. Thus, it was in principle only accounted for the ionizing decay channel of the photoexcited state via Auger or photoemission processes, whereas the competing channel of fluorescent deexcitation was neglected. Hence, strictly speaking, normalization was also only done to photoionization cross sections instead of the more general X-ray absorption cross sections. However, for light elements with $Z \leq 10$ the probability of fluorescent decay of $1s$ core holes only amounts to a few percent [26]. It is, therefore, justified to identify photoionization with the desired X-ray absorption cross sections here, though in general both should be well distinguished.

In summary, the total X-ray absorption cross section as well as the partial C, N, and O $1s$ cross sections of the protein layer plus SiO_x substrate, and of separation of the substrate signal also for the pristine protein layer, were obtained from a TEY measurement. To understand the following discussion of the $1s→ \pi^*_{peptide}$ oscillator strengths it should be clearly stated how the normalized spectra in the right panels of *Figure 5.8* must be understood. Since atomic cross sections were used for normalization, each spectrum shows the cross section of one C, N or O atom, that should be considered as the average over all probed C, N or O atoms. In other words, the C $1s$ spectrum, for instance, includes the spectral signature of all the different carbon containing chemical groups, each weighted with its respective relative occurrence of the chemical group. This should be always remembered when trying to extract cross sections or oscillator strengths for one particular chemical group, like it will be done now for the peptide group.

5.5.2   Oscillator strength of the peptide bond resonances

As stated in 5.4 one major aim of this XAS experiment on proteins was to derive a measure of the strength of the $1s→ \pi^*_{peptide}$ resonances. The choice of the $\pi^*_{peptide}$ orbital of the peptide group is motivated by the fact that it is unique to proteins and causes the most striking feature in protein NEXAFS spectra.

As briefly explained in 2.2.1 the X-ray absorption cross section σ is not appropriate to define the spectral intensity of a resonance. This is because it is defined for each particular photon energy whereas the peak of resonance ranges over a finite interval in energy defined by its line width. It is, therefore, helpful to define a new quantity, denoted as oscillator
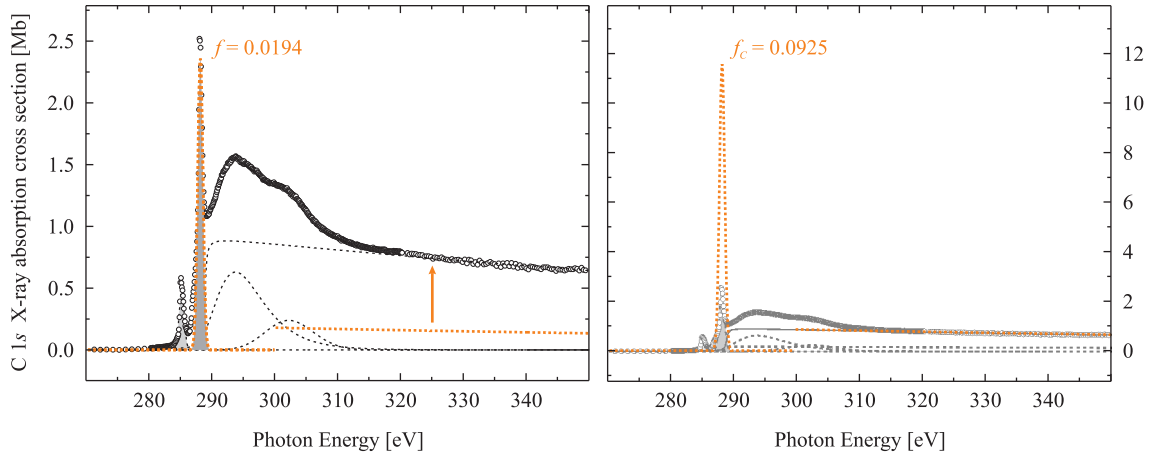
*Figure 5.9: The peptide group derived contribution to the C 1s NEXAFS spectrum was rescaled using the atomic cross section of a single carbon atom. This yields the cross section and oscillator strength for the C 1s→ π*peptide *excitation of with a single peptide group.*

strength f or f-number, related to σ via equation 2.13

$$\sigma(E) = \left(\frac{8\pi^2\alpha\hbar^2}{m}\right)\frac{df}{dE} = (109.8\,\text{Mb eV})\frac{df}{dE}$$

which can be also written in the integral form

$$f = (109.8\,\text{Mb eV})^{-1}\int_{-\infty}^{\infty}\sigma(E)\,dE \qquad (5.6)$$

From that, it becomes immediately apparent that f corresponds to the area below the considered resonance peak in a cross section spectrum, and thus represents the desired measure for the resonance intensity. This is illustrated in the left panel of *Figure 5.9* where f was determined for the $1s\to\pi^*_{peptide}$ resonance in the C 1s NEXAFS spectrum.

The obtained value $f = 0.0194$, however, does not yet give the desired objective estimate of the excitation probability for a C $1s\to\pi^*_{peptide}$ electron transition. It should be remembered here, that the shown spectrum is an average over all chemical groups found in the protein. Hence the particular spectral signature of the peptide group, or any other considered group, is surely underrepresented in the spectrum as compared to the isolated groups, and so is the derived f-number. One can overcome this obstacle by relating to the relative occurrence of peptide bond carbon atoms in the protein. For the considered S-layer protein it can be easily calculated from the known primary structure [126], that 21% of all carbon atoms within the protein are incorporated into its peptide groups. Therefore, $f = 0.0194$ can only be 21% of the real oscillator strength of the C $1s\to\pi^*_{peptide}$ resonance, too.

As indicated by the dotted orange line in the left panel of *Figure 5.9* the carbon atoms of the peptide units will contribute by only 21% to the intensity in the range of continuum

transitions. This is again, because this range is affected by atomic properties only and intensity therein must increase or decrease according to the relative chemical occurence of the considered group. The other purely peptide derived signature in the spectrum is the $\pi^*_{peptide}$ resonance. Hence when rescaling the peptide contribution in the continuum range to the full 100% C $1s$ atomic cross section the $\pi^*_{peptide}$ peak must rescale equally. This is illustrated in the right panel of *Figure 5.9* where the $\pi^*_{peptide}$ resonance now peaks at $\sim$12 MB instead of the previous 2.4 Mb. The C $1s \rightarrow \pi^*_{peptide}$ oscillator strength likewise changes to $f_C = 0.0925$. Note, that because of the rescaling f_C can now be identified with the oscillator strength of a single peptide group. It should therefore be comparable for any protein molecule independent on the actual sequence and types of protein side chains.

A similar analysis of the N $1s$ NEXAFS spectrum yields $f = 0.0108$ for the $1s \rightarrow \pi^*_{peptide}$ peak. Factoring in that only 83% of all nitrogen atoms participate in the peptide group I finally obtained $f_N = 0.0130$ for the oscillator strength of N $1s \rightarrow \pi^*_{peptide}$ excitations within the peptide group. From the oxygen spectrum one obtains $f = 0.0083$ for the $\pi^*_{peptide}$ peak. In order to derive the O $1s \rightarrow \pi^*_{peptide}$ oscillator strength of a single peptide group (f_O) this number should be rescaled again to the relative number of oxygen atoms in the peptide backbone (68%) as compared to the overall amount of oxygen in the protein. In addition, it must be remembered that the O $1s$ spectrum itself is to only 78% protein derived. The remaining 22% are SiO_x substrate contributions. Accounting for both effects one finally obtains $f_O = 0.0157$.

The experimentally obtained oscillator strength f_x (x =C, N, O) of the $1s \rightarrow \pi^*_{peptide}$ excitations within a single peptide group are highly informative quantities. In the following section, I will try to demonstrate their close correlation to the topology of the final state orbital which will eventually allow to roughly map the $\pi^*_{peptide}$ charge density.

It should be noted, that generally peptide bond oscillator strengths might depend on a couple of circumstances and can vary from protein structure to protein structure within certain boundaries. Differences in the oscillator strength of the peptide bond may arise from the fact that the latter must not to be considered as an isolated bond. Instead it could be influenced, among others, by the chain length of the polypeptide, the residues of neighboring amino acids and the conformation of the protein. For instance, previous experimental and theoretical studies on very short polypeptide chains indicate that the oscillator strength of the N $1s \rightarrow \pi^*_{peptide}$ resonance increases with increasing chain length and decreases with growing deviation of the peptide backbone from planar geometry [155]. However, in case of larger polypeptides these effects could cause if any rather minor deviations from the numbers presented here.

5.6 Correlation between $1s \rightarrow \pi^*_{peptide}$ oscillator strengths and the $\pi^*_{peptide}$ orbital topology

The close correlation between the geometry of the $\pi^*_{peptide}$ orbital into which the $1s$ electrons are excited and the oscillator strength of the respective X-ray driven transitions can be estimated from equation (2.16) when rewritten in position space representation

$$f_{ij} = \frac{2m}{\hbar^2} E_{ij} |\boldsymbol{e} \langle j | \hat{\boldsymbol{r}} | i \rangle|^2 \propto E_{ij} \left| \int d^3r \, d^3r' \, \boldsymbol{er} \, \varphi_j^*(\boldsymbol{r})\varphi_i(\boldsymbol{r}')\delta(\boldsymbol{r} - \boldsymbol{r}') \right|^2 \qquad (5.7)$$

where the transition energy E_{ij} can be approximated by the photon energy of the resonance peak maximum. Because of the statistical orientation of $\boldsymbol{e}$ with respect to the orbital geometry [153], equation (5.7) can be further simplified (cf. 2.2.2)

$$f_{ij} \propto E_{ij} \left| \int d^3r \, r \, \varphi_j^*(\boldsymbol{r})\varphi_i(\boldsymbol{r}) \right|^2 \qquad (5.8)$$

Evidently, the oscillator strengths f_x $(x = C, N, O)$ basically depend on the spatial overlap between the initial state, i.e. the respective $1s$ atomic-like, spherically symmetric orbital and the $\pi^*_{peptide}$ molecular orbital of the peptide bond as well as on the initial and final state energy separation.

While the wave function $\varphi_i(\boldsymbol{r})$ of the $1s$ initial state orbital is well modeled using atomic-like $1s$ wave functions, no reliable mathematical ansatz for $\varphi_j(\boldsymbol{r})$ can be made. Therefore, some simplifications must be assumed to further interpret (5.8). Inserting the atomic-like $1s$ wave function $\varphi_i(\boldsymbol{r}) = \pi^{-1/2}(Z/a_0)^{3/2} \exp(-Zr/a_0)$–where a_0 denotes the $1s$ orbital radius and Z the atomic number of the considered atom–(5.8) rewrites as

$$f_{ij} \propto E_{ij} \left| \left(\frac{Z}{a_0}\right)^{3/2} \int d^3r \, r \, \varphi_j^*(\boldsymbol{r}) \mathrm{e}^{-Zr/a_0} \right|^2 \qquad (5.9)$$

Because of the rapid decrease of the exponential function the integrand will vanish for larger r, i.e. $r > 3a_0$. Therefore, it is justifiable to take the integral only over a sphere with radius $r = 3a_0$ and centered at the considered atomic site. Now the main simplification is to approximate $\varphi_j(\boldsymbol{r})$ using a constant mean value $\overline{\varphi}_j$ within that sphere, i.e. to set $\varphi_j(\boldsymbol{r}) \approx \overline{\varphi}_j = const$ for $r \leq 3a_0$. At that $\overline{\varphi}_j$ should satisfy the following equation

$$\int_0^{3a_0} d^3r \varphi_j^*(\boldsymbol{r})\varphi_j(\boldsymbol{r}) = \overline{\varphi}_j^2 \int_0^{3a_0} d^3r = \frac{q_j}{e_0} \qquad (5.10)$$

with q_j the local final-state orbital charge found in the sphere $r \leq 3a_0$ centered around the respective atomic site and e_0 the electron charge. Under these assumptions (5.9) can be
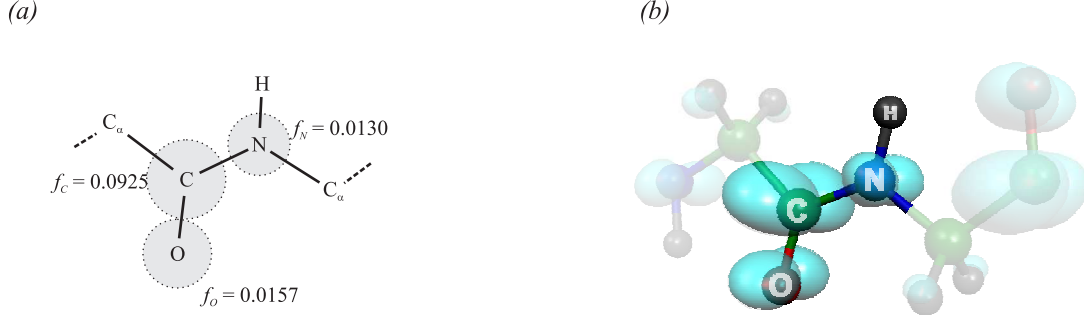
(a)

(b)

Figure 5.10: (a) $\pi^*_{peptide}$ charge distribution among the C, N and O site of the peptide group as estimated from the $1s \to \pi^*_{peptide}$ oscillator strengths. (b) Results of an ab initio calculation of the $\pi^*_{peptide}$ charge distribution.

rewritten as

$$f_{ij} \propto E_{ij} \frac{q_j}{e_0} \left| \left(\frac{Z}{a_0} \right)^{3/2} \int_0^{3a_0} dr\, 4\pi r^2\, r\, e^{-Zr/a_0} \right|^2 = E_{ij} \frac{q_j}{e_0} \left| 3 \left(\frac{a_0}{Z} \right)^{5/2} \left(2 - \underbrace{\frac{2 + 6Z + 9Z^2 + 9Z^3}{e^{3Z}}}_{\approx 0\,(Z=6,7,8)} \right) \right|^2$$

$$(5.11)$$

which finally yields the following, approximate dependence of the oscillator strength f_{ij}

$$f_{ij} \propto E_{ij} \frac{q_j}{e_0} \left(\frac{a_0}{Z} \right)^5 \qquad (5.12)$$

Looking at the experimental $1s \to \pi^*_{peptide}$ oscillator strengths f_x for the different X-ray absorption edges, they exhibit a pronounced enhancement when going from N $1s$ via O $1s$ to C $1s$ electron excitations. The different $1s$ orbital radii $(a_0)_x$ (x=C, N, O), which systematically decrease with growing atomic number Z [164], and the different transition energies E_x, which systematically increase with Z, can only partly explain the observed tendency. After weighing f_x with the well-known $1s$ orbital radii a_0 of carbon (0.091 Å), nitrogen (0.078 Å) and oxygen (0.068 Å), with the corresponding atomic number Z and with the experimental transition energies E_x, i.e. the peak position of the $\pi^*_{peptide}$ resonances, according to (5.12), a difference remains which must be due to unequal final state charge distribution q_x among the C, N, and O site of the peptide group

$$\frac{f_x}{(E\, a_0^5\, Z^{-5})_x} \propto \frac{q_x}{e_0} \qquad (x = C,\, N,\, O) \qquad (5.13)$$

which eventually allows to draw some conclusions about the final state orbital geometry.

Using this simplifying picture I found that $\sim$42% of the final state charge density should be located at the C site, $\sim$26% at the N site and $\sim$32% at the O site. This charge distribution is pictured in *Figure 5.10a* where the estimated $\pi^*_{peptide}$ charge distribution among the C, N and O atom is represented using circles with respectively scaled radii. In fact, this charge distribution derived from experimental data is in large agreement with results of supercell *ab initio* calculations performed for a polyglycine chain in β-sheet conformation [130, 131]. In *Figure 5.10b* I show the calculated charge distribution related to the unoccupied $\pi^*_{peptide}$ molecular orbital. Data calculated for other polyglycine conformations are similar to those shown for the β-sheet. Clearly, the calculated charge distribution shows a strong resemblance to the estimate derived from the measured $1s\rightarrow \pi^*_{peptide}$ oscillator strengths f_x. In both, the $\pi^*_{peptide}$ charge is mainly concentrated around the carbon site of the peptide backbone unit, whereas the oxygen and especially the nitrogen site hold much less share.

5.7 Conclusions

The presented experimental approach allows successful determination of absolute X-ray absorption cross sections. Especially, the possibility to work in the electron yield detection mode makes it a powerful tool to quantitatively study X-ray absorption properties of any type of molecule in the very detail. This was demonstrate here at the example of a layer of huge protein molecules adsorbed to a SiO_x substrate. In particular, the oscillator strengths of the C, N and O $1s\rightarrow \pi^*_{peptide}$ excitations could be obtained. They allowed to give an estimate of the charge density distribution in the $\pi^*_{peptide}$ peptide backbone orbital which was also confirmed by additionally performed *ab initio* calculations. The topology of this orbital might be of some interest with regard to future applications of protein layers because recent theoretical and experimental reports gave evidence that these orbitals are involved in electron transport along the protein chain takes place [130, 165, 166]

This is the first report of X-ray excitation oscillator strengths experimentally determined for molecules even as complex as the S layer protein. Until now respective studies were only performed for small molecules which can be studied in the gas phase. Since the here elaborated approach may readily be applied to any other system of surface adsorbed molecules, it may provide with a deeper and quantitative insight into the X-ray absorption properties of this class of materials. This involves, for instance, systems like the currently intensively discussed graphene layers on metal surfaces or copper phthalocyanine (CuPc) films. Advanced XAS studies can surely deliver valuable information on such systems. In particular, the demonstrated potential to map molecular orbitals might attract further interest in the future.

Note that surface adsorbed molecules often exhibited a preferred orientation with respect to the surface, resulting in an additional dependence of the resonance intensity on the angle between light polarization and sample (cf. 2.2.2). This must be additionally

accounted for during data analysis then, however, does not affect the applicability of the here presented approach

6 Summary

In this work three different biomolecular systems were studied with the aim to unravel structural properties by spectroscopic means using synchrotron radiation. These systems were namely mixed DNA-mercaptohexanol self-assembled monolayers, so-called DNA microarrays, for which the question was raised how their composition and structural order can be monitored and tuned in a controlled way. Secondly, two-dimensional, crystalline protein layers and their interaction with atomic and ionic calcium were investigated with the purpose to identify the preferred binding sites of the metal within the protein structure and to characterize the underlying reaction. Finally, X-ray absorption properties of huge proteins were studied and their close relation to the most-fundamental structural level, the level of single molecular orbitals, was exploited to map the topology of the $\pi^*_{peptide}$ orbital in the peptide bond unit.

The addressed issues, each with relevance to potential or existing applications, differed very much and so did the length scales characteristic to them. The entire range from the mesoscopic scale addressing a huge number of molecules simultaneously to the scale of single molecules and molecular groups to the level of single orbitals was covered. However, the three issues had the common ground that all of them cannot or can only hardly be solved with the standard tools for structure-related investigations, i.e. microscopic and diffraction techniques.

In contrast, synchrotron-based soft X-ray spectroscopies, more precisely X-ray photoemission and X-ray absorption spectroscopy, were in each case capable to deliver the information sought-after. This is due to close relation between the electronic structure of matter which these spectroscopies access and its chemical and structural properties aimed at. Of specific importance for all three studies was the chemical selectivity that is intrinsic to these core-level excitations probing spectroscopies and readily enables to distinguish the different light elements in biological specimen.

Because of the diversified specimen and issues that were subject to it, this work verifies the general capability of synchrotron-based spectroscopies in the soft X-ray range to unravel puzzles related to structural properties for systems where other, more common techniques may fail or work only unproportionally slow. This particularly applies to the class of

biomolecules and derived technological applications which have attracted much interest in the last years and certainly will become even more attractive in the years to come, also due to the perspective of bottom-up fabrication methods. Here spectroscopic methods could evolve to a future mean-of-choice providing with fast and comprehensive information on structural properties, that are required for a purposeful development and application of biotechnological systems fabricated in a bottom-up manner.

Bibliography

[1] A. Einstein. Über einen die Erzeugung und Verwandlung des Lichtes betreffenden heuristischen Gesichtspunkt. *Annalen der Physik* **1905**, 17, 132.

[2] K. Siegbahn. Electron spectroscopy for atoms, molecules, and condensed matter. *Rev. Mod. Phys.* **1982**, 54, 709.

[3] S. Hüfner. *Photoelectron Spectroscopy.* Springer Series in Solid-States Sciences. Springer, Berlin, 2nd edition 1996.

[4] S. Wilson. *Electron correlation in molecules.* Oxford University Press, USA 1984.

[5] O. Gunnarsson and K. Schönhammer. Many-Body Effects in XPS for Adsorbed Atoms and Molecules. *Phys. Scr.* **1980**, 21, 575.

[6] J. J. Yeh. *Atomic Calculation of Photoionization Cross-Sections and Asymmetry Parameters.* Gordon and Breach Science Publishers, Langhorn (USA) 1993.

[7] D. Briggs and M. P. Seah, editors. *Practical Surface Analysis Vol. 1 - Auger and X-ray Photoelectron Spectroscopy.* Wiley, Chichester, 2nd edition 1990.

[8] S. Doniach and M. Sunjic. Many-electron singularity in X-ray photoemission and X-ray line spectra from metals. *J. Phys. C* **1970**, 3, 285.

[9] M. P. Seah and W. A. Dench. Quantitative electron spectroscopy of surfaces: A standard data base for electron inelastic mean free paths in solids. *Surf. Interface Anal.* **1979**, 1, 2.

[10] D. A. Shirley. High-Resolution X-Ray Photoemission Spectrum of the Valence Bands of Gold. *Phys. Rev. B* **1972**, 5, 4709.

[11] F. R. Elder, A. M. Gurewitsch, R. V. Langmuir, and H. C. Pollock. Radiation from Electrons in a Synchrotron. *Phys. Rev.* **1947**, 71, 829.

[12] G. Margaritondo. The evolution of a dedicated synchrotron light source. *Physics Today* **2008**, 61, 37.

[13] G. Lebedev, C. Jozwiak, N. Andresen, A. Lanzara, and Z. Hussain. TOF electron energy analyzer for spin and angular resolved photoemission spectroscopy. Proceedings of the Seventh International Conference on Charged Particle Optics (CPO-7) *Physics Procedia* **2008**, 1, 413.

[14] J. Stöhr. *NEXAFS spectroscopy.* Springer Series in Surface Science. Springer, Berlin 1992.

[15] S. I. Fedoseenko, D. V. Vyalikh, I. E. Iossifov, R. Follath, S. A. Gorovikov, R. Pttner, J. S. Schmidt, S. L. Molodtsov, V. K. Adamchuk, W. Gudat, and G. Kaindl. Commissioning results and performance of the high-resolution Russian-German Beamline at BESSY II. *Nucl. Instrum. Methods Phys. Res., Sect. A* **2003**, 505, 718.

[16] U. Fano and J. W. Cooper. Spectral Distribution of Atomic Oscillator Strengths. *Rev. Mod. Phys.* **1968**, 40, 441.

[17] H. A. Bethe and E. E. Salpeter. *Quantum mechanics of one- and two-electron atoms.* Plenum Pr., New York 1977.

[18] J. L. Dehmer, D. Dill, and A. C. Parr. *Photophysics and Photochemistry in the Vacuum Ultraviolet.* Reidel, Dordrecht 1985.

[19] J. A. Sheehy, T. J. Gil, C. L. Winstead, R. E. Farren, and P. W. Langhoff. Correlation of molecular valence- and K-shell photoionization resonances with bond lengths. *J. Chem. Phys.* **1989**, 91, 1796.

[20] R. A. Rosenberg, P. J. Love, and Victor Rehn. Polarization-dependent C(K) near-edge x-ray-absorption fine structure of graphite. *Phys. Rev. B* **1986**, 33, 4034.

[21] D.A. Outka, J. Sthr, R.J. Madix, H.H. Rotermund, B. Hermsmeier, and J. Solomon. NEXAFS studies of complex alcohols and carboxylic acids on the Si(111)(77) surface. *Surf. Sci.* **1987**, 185, 53.

[22] J. Stöhr and R. J. Madix. Unpublished results.

[23] G. Cooper, M. Gordon, D. Tulumello, C. Turci, K. Kaznatcheev, and A. P. Hitchcock. Inner shell excitation of glycine, glycyl-glycine, alanine and phenylalanine. ICESS-9 Proceedings of the 9th International Conference on Electronic Spectroscopy and Structure *J. Electron Spectrosc. Relat. Phenom.* **2004**, 137-140, 795.

[24] J. L. Dehmer, Dan Dill, and Scott Wallace. Shape-Resonance-Enhanced Nuclear-Motion Effects in Molecular Photoionization. *Phys. Rev. Lett.* **1979**, 43, 1005.

[25] D. A. Outka and J. Stöhr. Curve fitting analysis of near-edge core excitation spectra of free, adsorbed, and polymeric molecules. *J. Chem. Phys.* **1988**, 88, 3539.

[26] A. Kotani and S. Shin. Resonant inelastic x-ray scattering spectra for electrons in solids. *Rev. Mod. Phys.* **2001**, 73, 203.

[27] W. Gudat and C. Kunz. Close Similarity between Photoelectric Yield and Photoabsorption Spectra in the Soft-X-Ray Range. *Phys. Rev. Lett.* **1972**, 29, 169.

[28] R. G. Nuzzo and D. L. Allara. Adsorption of bifunctional organic disulfides on gold surfaces. *J. Am. Chem. Soc.* **1983**, 105, 4481.

[29] A. Ulman. Formation and Structure of Self-Assembled Monolayers. *Chem. Rev.* **1996**, 96, 1533.

[30] J. C. Love, L. A. Estroff, J. K. Kriebel, R. G. Nuzzo, and G. M. Whitesides. Self-Assembled Monolayers of Thiolates on Metals as a Form of Nanotechnology. *Chem. Rev.* **2005**, 105, 1103.

[31] F. Schreiber. Self-assembled monolayers: from simple model systems to biofunctionalized interfaces. *J. Phys.: Condens. Matter* **2004**, 16, R881.

[32] F. Schreiber. Structure and growth of self-assembling monolayers. *Prog. Surf. Sci.* **2000**, 65, 151.

[33] H. J. Lee, T. T. Goodrich, and R. M. Corn. SPR Imaging Measurements of 1-D and 2-D DNA Microarrays Created from Microfluidic Channels on Gold Thin Films. *Anal. Chem.* **2001**, 73, 5525.

[34] J. Ladd, A. D. Taylor, M. Piliarik, J. Homola, and S. Jiang. Hybrid Surface Platform for the Simultaneous Detection of Proteins and DNAs Using a Surface Plasmon Resonance Imaging Sensor. *Anal. Chem.* **2008**, 80, 4231.

[35] J. Spadavecchia, M.G. Manera, F. Quaranta, P. Siciliano, and R. Rella. Surface plamon resonance imaging of DNA based biosensors for potential applications in food analysis. *Biosens. Bioelectron.* **2005**, 21, 894.

[36] C. Boozer, J. Ladd, S. Chen, Q. Yu, J. Homola, and S. Jiang. DNA Directed Protein Immobilization on Mixed ssDNA/Oligo(ethylene glycol) Self-Assembled Monolayers for Sensitive Biosensors. *Anal. Chem.* **2004**, 76, 6967.

[37] C. Boozer, J. Ladd, S. Chen, and S. Jiang. DNA-Directed Protein Immobilization for Simultaneous Detection of Multiple Analytes by Surface Plasmon Resonance Biosensor. *Anal. Chem.* **2006**, 78, 1515.

[38] E. Braun, Y. Eichen, U. Sivan, and G. Ben-Yoseph. DNA-templated assembly and electrode attachment of a conducting silver wire. *Nature* **1998**, 391, 775.

[39] M. Schena, D. Shalon, R. W. Davis, and P. O. Brown. Quantitative Monitoring of Gene Expression Patterns with a Complementary DNA Microarray. *Science* **1995**, 270, 467.

[40] P. O. Brown and D. Botstein. Exploring the new world of the genome with DNA microarrays. *Nature Genetics* **1999**, 21, 33.

[41] H. Kimura-Suda, D. Y. Petrovykh, M. J. Tarlov, and L. J. Whitman. Base-Dependent Competitive Adsorption of Single-Stranded DNA on Gold. *J. Am. Chem. Soc.* **2003**, 125, 9014.

[42] L. M. Demers, M. Ostblom, H. Zhang, N.-H. Jang, B. Liedberg, and C. A. Mirkin. Thermal Desorption Behavior and Binding Properties of DNA Bases and Nucleosides on Gold. *J. Am. Chem. Soc.* **2002**, 124, 11248.

[43] L. K. Wolf, Y. Gao, and R. M. Georgiadis. Sequence-Dependent DNA Immobilization: Specific versus Nonspecific Contributions. *Langmuir* **2004**, 20, 3357.

[44] M. Ostblom, B. Liedberg, L. M. Demers, and C. A. Mirkin. On the Structure and Desorption Dynamics of DNA Bases Adsorbed on Gold: A Temperature-Programmed Study. *J. Phys. Chem. B* **2005**, 109, 15150.

[45] S. Piana and A. Bilic. The Nature of the Adsorption of Nucleobases on the Gold [111] Surface. *J. Phys. Chem. B* **2006**, 110, 23467.

[46] A. Opdahl, D. Y. Petrovykh, H. Kimura-Suda, M. J. Tarlov, and L. J. Whitman. Independent control of grafting density and conformation of single-stranded DNA brushes. *Proc. Natl. Acad. Sci. U. S. A.* **2007**, 104, 9.

[47] H. Kimura-Suda, A. Opdahl, M. J. Tarlov, L. J. Whitman, and D. Y. Petrovykh. Characterization and Controlled Properties of DNA Immobilized on Gold Surfaces. *Kobunshi Ronbunshu* **2008**, 65, 46.

[48] U. Rant, K. Arinaga, S. Fujita, N. Yokoyama, G. Abstreiter, and M. Tornow. Structural Properties of Oligonucleotide Monolayers on Gold Surfaces Probed by Fluorescence Investigations. *Langmuir* **2004**, 20, 10086.

[49] T. K. Chiu and R. E. Dickerson. 1 Åcrystal structures of B-DNA reveal sequence-specific binding and groove-specific bending of DNA by magnesium and calcium. *J. Mol. Biol.* **2000**, 301, 915.

[50] T. M. Herne and M. J. Tarlov. Characterization of DNA Probes Immobilized on Gold Surfaces. *J. Am. Chem. Soc.* **1997**, 119, 8916.

[51] R. Levicky, T. M. Herne, M. J. Tarlov, and S. K. Satija. Using Self-Assembly To Control the Structure of DNA Monolayers on Gold: A Neutron Reflectivity Study. *J. Am. Chem. Soc.* **1998**, 120, 9787.

[52] A. B. Steel, T. M. Herne, and M. J. Tarlov. Electrochemical Quantitation of DNA Immobilized on Gold. *Anal. Chem.* **1998**, 70, 4670.

[53] A. W. Peterson, R. J. Heaton, and R. M. Georgiadis. The effect of surface probe density on DNA hybridization. *Nucl. Acids Res.* **2001**, 29, 5163.

[54] R. Georgiadis, K. P. Peterlinz, and A. W. Peterson. Quantitative Measurements and Modeling of Kinetics in Nucleic Acid Monolayer Films Using SPR Spectroscopy. *J. Am. Chem. Soc.* **2000**, 122, 3166.

[55] E. L. S. Wong, E. Chow, and J. J. Gooding. DNA Recognition Interfaces: The Influence of Interfacial Design on the Efficiency and Kinetics of Hybridization. *Langmuir* **2005**, 21, 6957.

[56] D. Y. Petrovykh, H. Kimura-Suda, L. J. Whitman, and M. J. Tarlov. Quantitative Analysis and Characterization of DNA Immobilized on Gold. *J. Am. Chem. Soc.* **2003**, 125, 5219.

[57] D. Y. Petrovykh, H. Kimura-Suda, M. J. Tarlov, and L. J. Whitman. Quantitative Characterization of DNA Films by X-ray Photoelectron Spectroscopy. *Langmuir* **2004**, 20, 429.

[58] D. Y. Petrovykh, V. Perez-Dieste, A. Opdahl, H. Kimura-Suda, J. M. Sullivan, M. J. Tarlov, F. J. Himpsel, and L. J. Whitman. Nucleobase Orientation and Ordering in Films of Single-Stranded DNA on Gold. *J. Am. Chem. Soc.* **2006**, 128, 2.

[59] C.-Y. Lee, P. Gong, G. M. Harbers, D. W. Grainger, D. G. Castner, and L. J. Gamble. Surface Coverage and Structure of Mixed DNA/Alkylthiol Monolayers on Gold: Characterization by XPS, NEXAFS, and Fluorescence Intensity Measurements. *Anal. Chem.* **2006**, 78, 3316.

[60] G. E. Poirier. Characterization of Organosulfur Molecular Monolayers on Au(111) using Scanning Tunneling Microscopy. *Chem. Rev.* **1997**, 97, 1117.

[61] K. Kummer, D. V. Vyalikh, G. Gavrila, A. Kade, M. Weigel-Jech, M. Mertig, and S. L. Molodtsov. High-resolution photoelectron spectroscopy of self-assembled mercaptohexanol monolayers on gold surfaces. *J. Electron Spectrosc. Relat. Phenom.* **2008**, 163, 59.

[62] A. Shaporenko, A. Terfort, M. Grunze, and M. Zharnikov. A detailed analysis of the photoemission spectra of basic thioaromatic monolayers on noble metal substrates. *J. Electron Spectrosc. Relat. Phenom.* **2006**, 151, 45.

[63] K. Heister, L. S. O. Johansson, M. Grunze, and M. Zharnikov. A detailed analysis of the C 1s photoemission of n-alkanethiolate films on noble metal substrates. *Surf. Sci.* **2003**, 529, 36.

[64] A. L. Allred. Electronegativity values from thermochemical data. *J. Inorg. Nucl. Chem.* **1961**, 17, 215.

[65] L. Pauling. *The Nature of the Chemical Bond.* Cornell University Press, New York, 3rd edition 1980.

[66] S. Shimada, T. Hiroi, T. Ida, M. Mizuno, K. Endo, E. Z. Kurmaev, and A. Moewes. X-ray photoelectron and carbon Kalpha emission measurements and calculations of O-, CO-, N-, and S-containing substances. *J. Polym. Sci. B* **2007**, 45, 162.

[67] M. Cardona and L. Ley, editors. *Photoemission in Solids I: General Principles.* Springer, Berlin 1978.

[68] D. G. Castner, K. Hinds, and D. W. Grainger. X-ray Photoelectron Spectroscopy Sulfur 2p Study of Organic Thiol and Disulfide Binding Interactions with Gold Surfaces. *Langmuir* **1996**, 12, 5083.

[69] J. Heeg, U. Schubert, and F. Küchenmeister. Mixed self-assembled monolayers of terminally functionalized thiols at gold surfaces characterized by angle resolved X-ray photoelectron spectroscopy (ARXPS) studies. *Fresenius J. Anal. Chem.* **1999**, 365, 272.

[70] G. Heimel, L. Romaner, J.-L. Brdas, and E. Zojer. Organic/metal interfaces in self-assembled monolayers of conjugated thiols: A first-principles benchmark study. *Surf. Sci.* **2006**, 600, 4548.

[71] T. Ishida, M. Hara, I. Kojima, S. Tsuneda, N. Nishida, H. Sasabe, and W. Knoll. High Resolution X-ray Photoelectron Spectroscopy Measurements of Octadecanethiol Self-Assembled Monolayers on Au(111). *Langmuir* **1998**, 14, 2092.

[72] M. Wirde, U. Gelius, and L. Nyholm. Self-Assembled Monolayers of Cystamine and Cysteamine on Gold Studied by XPS and Voltammetry. *Langmuir* **1999**, 15, 6370.

[73] M. Wirde, U. Gelius, T. Dunbar, and D.L. Allara. Modification of self-assembled monolayers of alkanethiols on gold by ionizing radiation. Ionizing Radiation and Polymers *Nuclear Instruments and Methods in Physics Research Section B: Beam Interactions with Materials and Atoms* **1997**, 131, 245.

[74] J. A. Rodriguez, J. Dvorak, T. Jirsak, G. Liu, J. Hrbek, Y. Aray, and C. Gonzalez. Coverage Effects and the Nature of the Metal-Sulfur Bond in S/Au(111): High-Resolution Photoemission and Density-Functional Studies. *J. Am. Chem. Soc.* **2003**, 125, 276.

[75] J. D. Watson and F. H. C. Crick. Molecular Structure of Nucleic Acids: A Structure for Deoxyribose Nucleic Acid. *Nature* **1953**, 171, 737.

[76] M. H. F. Wilkins, A. R. Stokes, and H. R. Wilson. Molecular Structure of Nucleic Acids: Molecular Structure of Deoxypentose Nucleic Acids. *Nature* **1953**, 171, 738.

[77] R. E. Franklin and R. G. Gosling. Molecular Configuration in Sodium Thymonucleate. *Nature* **1953**, 171, 740.

[78] C. J. May, H. E. Canavan, and D. G. Castner. Quantitative X-ray Photoelectron Spectroscopy and Time-of-Flight Secondary Ion Mass Spectrometry Characterization of the Components in DNA. *Anal. Chem.* **2004**, 76, 1114.

[79] C.-Y. Lee, L. J. Gamble, D. W. Grainger, and D. G. Castner. Mixed DNA/oligo(ethylene glycol) functionalized gold surfaces improve DNA hybridization in complex media. *Biointerphases* **2006**, 1, 82.

[80] Y. Takahata, A. K. Okamoto, and D. P. Chong. DFT calculation of core-electron binding energies of pyrimidine and purine bases. *Int. J. Quantum Chem.* **2006**, 106, 2581.

[81] T. Hayakawa, M. Yoshinari, and K. Nemoto. Direct attachment of fibronectin to tresyl chloride-activated titanium. *Journal of Biomedical Materials Research Part A* **2003**, 67A, 684.

[82] R. Fu, B. Zheng, J. Liu, S. Weiss, J. Y. Ying, M. S. Dresselhaus, G. Dresselhaus, J. Satcher Jr., and T. Baumann. Studies of the chemical and pore structures of the carbon aerogels synthesized by gelation and supercritical drying in isopropanol. *J. Appl. Polym. Sci.* **2004**, 91, 3060.

[83] R. K. Brow and Z. A. Osborne. XPS Studies of Fluorine Bonding in Phosphate Glasses. *Surface and Interface Analysis* **1996**, 24, 91.

[84] K. Juodkazis, J. Juodkazyte, V. Jasulaitiene, A. Lukinskas, and B. Sebeka. XPS studies on the gold oxide surface layer formation. *Electrochem. Commun.* **2000**, 2, 503.

[85] C. D. Wagner, D. A. Zatko, and R. H. Raymond. Use of the oxygen KLL Auger lines in identification of surface chemical states by electron spectroscopy for chemical analysis. *Anal. Chem.* **1980**, 52, 1445.

[86] J. E. Huheey, E. A. Keiter, and R. L. Keiter. *Inorganic Chemistry: Principles of Structure and Reactivity.* HarperCollins, New York, 4th edition 1993.

[87] A. M. James and M. P. Lord. *Macmillan's Chemical and Physical Data.* Macmillan, London 1992.

[88] N. V. Hud and M. Polak. DNA-cation interactions: the major and minor grooves are flexible ionophores. *Curr. Opin. Struct. Biol.* **2001**, 11, 293.

[89] L. McFail-Isom, C. C. Sines, and L. Dean Williams. DNA structure: cations in charge? *Curr. Opin. Struct. Biol.* **1999**, 9, 298.

[90] H. Asanuma, H. Noguchi, K. Uosaki, and H.-Z. Yu. Metal Cation-Induced Deformation of DNA Self-Assembled Monolayers on Silicon: Vibrational Sum Frequency Generation Spectroscopy. *J. Am. Chem. Soc.* **2008**, 130, 8016.

[91] A.B. Steel, R.L. Levicky, T.M. Herne, and M.J. Tarlov. Immobilization of Nucleic Acids at Solid Surfaces: Effect of Oligonucleotide Length on Layer Assembly. *Biophys. J.* **2000**, 79, 975.

[92] B. Tinland, A. Pluen, J. Sturm, and G. Weill. Persistence Length of Single-Stranded DNA. *Macromolecules* **1997**, 30, 5763.

[93] Y. Ishige, M. Shimoda, and M. Kamahori. Immobilization of DNA Probes onto Gold Surface and its Application to Fully Electric Detection of DNA Hybridization using Field-Effect Transistor Sensor. *Jpn. J. Appl. Phys.* **2006**, 45, 3776.

[94] S. D. Keighley, P. Li, P. Estrela, and P. Migliorato. Optimization of DNA immobilization on gold electrodes for label-free detection by electrochemical impedance spectroscopy. *Biosens. Bioelectron.* **2008**, 23, 1291.

[95] Y. Sakao, N. Ueno, F. Nakamura, E. Ito, J. Hayasi, and M. Hara. Formation of DNA self-assembled monolayer on a gold substrate. *Mol. Cryst. Liq. Cryst.* **2003**, 407, 141.

[96] Y. Sakao, F. Nakamura, N. Ueno, and M. Hara. Hybridization of oligonucleotide by using DNA self-assembled monolayer. A selection of papers from the 10th International Conference on Organised Molecular Films *Colloids Surf. B* **2005**, 40, 149.

[97] A. Zangwill. *Physics at Surfaces.* Cambridge University Press, Cambridge 1988.

[98] Y. Fang, T. S. Spisz, and J. H. Hoh. Ethanol-induced structural transitions of DNA on mica. *Nucl. Acids Res.* **1999**, 27, 1943.

[99] A. P. Feinberg and B. Vogelstein. A technique for radiolabeling DNA restriction endonuclease fragments to high specific activity. *Anal. Biochem.* **1983**, 132, 613.

[100] D. S. Karpovich and G. J. Blanchard. Direct Measurement of the Adsorption Kinetics of Alkanethiolate Self-Assembled Monolayers on a Microcrystalline Gold Surface. *Langmuir* **1994**, 10, 3315.

[101] A. B. Parekh and J. W. Putney Jr. Store-Operated Calcium Channels. *Physiol. Rev.* **2005**, 85, 757.

[102] J. Roos, P. J. DiGregorio, A. V. Yeromin, K. Ohlsen, M. Lioudyno, S. Zhang, O. Safrina, J. A. Kozak, S. L. Wagner, M. D. Cahalan, G. Velicelebi, and K. A. Stauderman. STIM1, an essential and conserved component of store-operated Ca2+ channel function. *J. Cell Biol.* **2005**, 169, 435.

[103] P. S. Brookes, Y. Yoon, J. L. Robotham, M. W. Anders, and S.-S. Sheu. Calcium, ATP, and ROS: a mitochondrial love-hate triangle. *Am. J. Physiol. Cell Physiol.* **2004**, 287, C817.

[104] R. Rizzuto and T. Pozzan. Microdomains of Intracellular Ca2+: Molecular Determinants and Functional Consequences. *Physiol. Rev.* **2006**, 86, 369.

[105] Z. Grabarek. Structural Basis for Diversity of the EF-hand Calcium-binding Proteins. *Journal of Molecular Biology* **2006**, 359, 509.

[106] R. B. Best and G. Hummer. Unfolding the Secrets of Calmodulin. *Science* **2009**, 323, 593.

[107] T.C. Südhof. The synaptic vesicle cycle. *Annu. Rev. Neurosci.* **2004**, 27, 509.

[108] T. Kobayashi and R. J. Solaro. Calcium, thin filaments, and the integrative biology of cardiac contractility. *Annu. Rev. Physiol.* **2005**, 67, 39-67.

[109] R. D. Jackson et al. Calcium plus Vitamin D Supplementation and the Risk of Fractures. *N. Engl. J. Med.* **2006**, 354, 669.

[110] U. B. Sleytr and P. Messner. Crystalline Surface Layers on Bacteria. *Annual Review of Microbiology* **1983**, 37, 311.

[111] Series of reviews in *FEMS Microbiol. Rev.* **1997**, 20, 5–175.

[112] M. Sara and U. B. Sleytr. S-Layer Proteins. *J. Bacteriol.* **2000**, 182, 859.

[113] W. Shenton, D. Pum, U. B. Sleytr, and S. Mann. Synthesis of cadmium sulphide superlattices using self-assembled bacterial S-layers. *Nature* **1997**, 389, 585.

[114] S. Dieluweit, D. Pum, and U. B. Sleytr. Formation of a gold superlattice on an S-layer with square lattice symmetry. *Supramol. Sci.* **1998**, 5, 15.

[115] M. Mertig, R. Kirsch, W. Pompe, and H. Engelhardt. Fabrication of highly oriented nanocluster arrays by biomolecular templating. *Eur. Phys. J. D* **1999**, 9, 45.

[116] M. Mertig, R. Wahl, M. Lehmann, P. Simon, and W. Pompe. Formation and manipulation of regular metallic nanoparticle arrays on bacterial surface layers: an advanced TEM study. *Eur. Phys. J. D* **2001**, 16, 317.

[117] R. Wahl, M. Mertig, J. Raff, S. Selenska-Pobell, and W. Pompe. Electron-Beam Induced Formation of Highly Ordered Palladium and Platinum Nanoparticle Arrays on the S Layer of Bacillus sphaericus NCTC 9602. *Adv. Mater.* **2001**, 13, 736.

[118] M. Merroun, A. Rossberg, C. Hennig, A.C. Scheinost, and S. Selenska-Pobell. Spectroscopic characterization of gold nanoparticles formed by cells and S-layer protein of Bacillus sphaericus JG-A12. *Mater. Sci. Eng. C* **2007**, 27, 188.

[119] U. Queitsch, E. Mohn, F. Schäffel, L. Schultz, B. Rellinghaus, A. Blüher, and M. Mertig. Regular arrangement of nanoparticles from the gas phase on bacterial surface-protein layers. *Appl. Phys. Lett.* **2007**, 90, 113114.

[120] D. V. Vyalikh, S. Danzenbächer, M. Mertig, A. Kirchner, W. Pompe, Yu. S. Dedkov, and S. L. Molodtsov. Electronic Structure of Regular Bacterial Surface Layers. *Phys. Rev. Lett.* **2004**, 93, 238103.

[121] A. P. Mancuso, A. Schropp, B. Reime, L.-M. Stadler, A. Singer, J. Gulden, S. Streit-Nierobisch, C. Gutt, G. Grübel, J. Feldhaus, F. Staier, R. Barth, A. Rosenhahn, M. Grunze, T. Nisius, T. Wilhein, D. Stickler, H. Stillrich, R. Frömter, H.-P. Oepen, M. Martins, B. Pfau, C. M. Günther, R. Könnecke, S. Eisebitt, B. Faatz, N. Guerassimova, K. Honkavaara, V. Kocharyan, R. Treusch, E. Saldin, S. Schreiber, E. A. Schneidmiller, M. V. Yurkov, E. Weckert, and I. A. Vartanyants. Coherent-Pulse 2D Crystallography Using a Free-Electron Laser X-Ray Source. *Phys. Rev. Lett.* **2009**, 102, 035502.

[122] G. J. Thomas. Raman spectroscopy of protein and nucleic acid assemblies. *Annu. Rev. Biophys. Biomol. Struct.* **1999**, 28, 1.

[123] R. Schweitzer-Stenner. Visible and UV-resonance Raman spectroscopy of model peptides. *J. Raman Spectrosc.* **2001**, 32, 711.

[124] A. V. Mikhonin, Z. Ahmed, A. Ianoul, and S. A. Asher. Assignments and Conformational Dependencies of the Amide III Peptide Backbone UV Resonance Raman Bands. *J. Phys. Chem. B* **2004**, 108, 19020.

[125] D. V. Vyalikh, A. Kirchner, S. Danzenbacher, Yu. S. Dedkov, A. Kade, M. Mertig, and S. L. Molodtsov. Photoemission and Near-Edge X-Ray Absorption Fine Structure Studies of the Bacterial Surface Protein Layer of Bacillus sphaericus NCTC 9602. *J. Phys. Chem. B* **2005**, 109, 18620.

[126] Uniprot database. `http://www.uniprot.org/`.

[127] A. Kade, D. V. Vyalikh, S. Danzenbächer, K. Kummer, A. Blüher, M. Mertig, A. Lanzara, A. Scholl, A. Doran, and S. L. Molodtsov. X-ray Absorption Microscopy of Bacterial Surface Protein Layers: X-ray Damage. *J. Phys. Chem. B* **2007**, 111, 13491.

[128] H. Van Doveren and J. A. T. H. Verhoeven. XPS spectra of Ca, Sr, Ba and their oxides. *J. Electron Spectrosc. Relat. Phenom.* **1980**, 21, 265.

[129] J. Y. Ko, Z. Xingtai, T. K. Sham, F. Heigl, T. Regier, and R. Blyth. X-ray absorption near-edge structure (xanes) of calcium l3, 2 edges of various calcium compounds and x-ray excited optical luminescence (xeol) studies of luminescent calcium compounds. In *AIP Conference Proceedings*, volume 882 2007.

[130] D. V. Vyalikh, V. V. Maslyuk, A. Blüher, A. Kade, K. Kummer, Yu. S. Dedkov, T. Bredow, I. Mertig, M. Mertig, and S. L. Molodtsov. Charge Transport in Proteins Probed by Resonant Photoemission. *Phys. Rev. Lett.* **2009**, 102, 098101.

[131] V. V. Maslyuk, I. Mertig, T. Bredow, M. Mertig, D. V. Vyalikh, and S. L. Molodtsov. Electronic structure of bacterial surface protein layers. *Phys. Rev. B* **2008**, 77, 045419.

[132] R. Krishnan, J. S. Binkley, R. Seeger, and J. A. Pople. Self-consistent molecular orbital methods. XX. A basis set for correlated wave functions. *J. Chem. Phys.* **1980**, 72, 650.

[133] V. R. Saunders, R. Dovesi, C. Roetti, R. Orlando, C. M. Zicovich-Wilson, N. M. Harrison, K. Doll, B. Civalleri, I. Bush, Ph. D'Arco, and M. Llunell. *CRYSTAL2003 User's Manual.* University of Turin, Turin, 2004. `http://www.crystal.unito.it/Manuals/crystal03.pdf`.

[134] A. D. Becke. Density-functional thermochemistry. III. The role of exact exchange. *J. Chem. Phys.* **1993**, 98, 5648.

[135] TURBOMOLE database. Institute für Physikalische Chemie, Universität Karlsruhe, `ftp://ftp.chemie.uni-karlsruhe.de/pub/basen/ca`.

[136] M. J. Pilling and P. W. Seakins. *Reaction kinetics.* Oxford University Press, Oxford 1996. Reprint.

[137] M.A. Bolorizadeh, V.A. Sashin, A.S. Kheifets, and M.J. Ford. Electronic band structure of calcium oxide. *J. Electron Spectrosc. Relat. Phenom.* **2004**, 141, 27.

[138] T. Saitoh, A. Sekiyama, K. Kobayashi, T. Mizokawa, A. Fujimori, D. D. Sarma, Y. Takeda, and M. Takano. Temperature-dependent valence-band photoemission spectra of $La_{1-x}Sr_xMnO_3$. *Phys. Rev. B* **1997**, 56, 8836.

[139] A. Fujimori, J. H. Weaver, and A. Franciosi. Core-hole screening and plasmon satellites in calcium. *Phys. Rev. B* **1985**, 31, 3549.

[140] W. Wurth, J. Stöhr, P. Feulner, X. Pan, K. R. Bauchspiess, Y. Baba, E. Hudel, G. Rocker, and D. Menzel. Bonding, structure, and magnetism of physisorbed and chemisorbed $O2$ on Pt(111). *Phys. Rev. Lett.* **1990**, 65, 2426.

[141] J. Stewart-Ornstein, A. P. Hitchcock, D. Hernandez Cruz, P. Henklein, J. Overhage, K. Hilpert, J. D. Hale, and R. E. W. Hancock. Using Intrinsic X-ray Absorption Spectral Differences To Identify and Map Peptides and Proteins. *J. Phys. Chem. B* **2007**, 111, 7691.

[142] J. Stöhr, F. Sette, and Allen L. Johnson. Near-Edge X-Ray-Absorption Fine-Structure Studies of Chemisorbed Hydrocarbons: Bond Lengths with a Ruler. *Phys. Rev. Lett.* **1984**, 53, 1684.

[143] G. Apai, J. F. Hamilton, J. Stohr, and A. Thompson. Extended X-Ray Absorption Fine Structure of Small Cu and Ni Clusters: Binding-Energy and Bond-Length Changes with Cluster Size. *Phys. Rev. Lett.* **1979**, 43, 165.

[144] J. Stöhr, K. Baberschke, R. Jaeger, R. Treichler, and S. Brennan. Orientation of Chemisorbed Molecules from Surface-Absorption Fine-Structure Measurements: CO and NO on Ni(100). *Phys. Rev. Lett.* **1981**, 47, 381.

[145] J. Stöhr and D. A. Outka. Determination of molecular orientations on surfaces from the angular dependence of near-edge x-ray-absorption fine-structure spectra. *Phys. Rev. B* **1987**, 36, 7891.

[146] E. R. Peterson, C. Buth, D. A. Arms, R. W. Dunford, E. P. Kanter, B. Krässig, E. C. Landahl, S. T. Pratt, R. Santra, S. H. Southworth, and L. Young. An x-ray probe of laser-aligned molecules. *Appl. Phys. Lett.* **2008**, 92, 094106.

[147] S. Molodtsov, S. Fedoseenko, D. Vyalikh, I. Iossifov, R. Follath, S. Gorovikov, M. Brzhezin-skaya, Y. Dedkov, R. Püttner, J.-S. Schmidt, V. Adamchuk, W. Gudat, and G. Kaindl. High-resolution Russian-German beamline at BESSY. *Appl. Phys. A: Mater. Sci. Process.* **2009**, 94, 501.

[148] S. A. Gorovikov, S. L. Molodtsov, and R. Follath. Optical design of the high-energy resolution beamline at a dipole magnet of BESSY II. *Nucl. Instrum. Methods Phys. Res., Sect. A* **1998**, 411, 506.

[149] F. C. Brown, R. Z. Bachrach, and A. Bianconi. Fine structure above the carbon K-edge in methane and in the fluoromethanes. *Chem. Phys. Lett.* **1978**, 54, 425.

[150] V. N. Sivkov and A. S. Vinogradov. *Physics of the Solid State* **1983**, 25, 897.

[151] S. V. Nekipelov and V. N. Sivkov. *Physics of the Solid State* **1994**, 36, 1512.

[152] R. Nakajima, J. Stöhr, and Y.U. Idzerda. Electron-yield saturation effects in L-edge x-ray magnetic circular dichroism spectra of Fe, Co, and Ni. *Phys. Rev. B* **1999**, 59, 6421.

[153] D. V. Vyalikh, A. Kirchner, A. Kade, S. Danzenbacher, Yu. S. Dedkov, M. Mertig, and S. L. Molodtsov. Spectroscopic studies of the electronic properties of regularly arrayed two-dimensional protein layers. *J. Phys.: Condens. Matter* **2006**, 18, S131.

[154] Y. Zubavichus, A. Shaporenko, M. Grunze, and M. Zharnikov. Is X-ray Absorption Spectroscopy Sensitive to the Amino Acid Composition of Functional Proteins? *J. Phys. Chem. B* **2008**, 112, 4478.

[155] M. L. Gordon, G. Cooper, C. Morin, T. Araki, C. C. Turci, K. Kaznatcheev, and A. P. Hitchcock. Inner-Shell Excitation Spectroscopy of the Peptide Bond: Comparison of the C 1s, N 1s, and O 1s Spectra of Glycine, Glycyl-Glycine, and Glycyl-Glycyl-Glycine. *J. Phys. Chem. A* **2003**, 107, 6144.

[156] B. W. Loo Jr., I. M. Sauerwald, A. P. Hitchcock, and S. S. Rothman. A new sample preparation method for biological soft X-ray microscopy: nitrogen-based contrast and radiation tolerance properties of glycol methacrylate-embedded and sectioned tissue. *J. Microsc.* **2001**, 204, 69.

[157] Y. Zubavichus, A. Shaporenko, M. Grunze, and M. Zharnikov. Innershell Absorption Spectroscopy of Amino Acids at All Relevant Absorption Edges. *J. Phys. Chem. A* **2005**, 109, 6998.

[158] A.P. Hitchcock, C. Morin, Y.M. Heng, R.M. Cornelius, and J.L. Brash. Towards practical soft X-ray spectromicroscopy of biomaterials. *Journal of Biomaterials Science, Polymer Edition* **2002**, 13, 919.

[159] K. Kaznacheyev, A. Osanna, C. Jacobsen, O. Plashkevych, O. Vahtras, O. H. Agren, V. Carravetta, and A. P. Hitchcock. Innershell Absorption Spectroscopy of Amino Acids. *J. Phys. Chem. A* **2002**, 106, 3153.

[160] J. Boese, A. Osanna, C. Jacobsen, and J. Kirz. Carbon edge XANES spectroscopy of amino acids and peptides. *J. Electron Spectrosc. Relat. Phenom.* **1997**, 85, 9.

[161] V. Carravetta, O. Plashkevych, and H. Ågren. A theoretical study of the near-edge x-ray absorption spectra of some larger amino acids. *J. Chem. Phys.* **1998**, 109, 1456.

[162] V. N. Sivkov, V. N. Akimov, A. S. Vinogradov, and T. M. Eimkina. *Optics and Spectroscopy* **1986**, 60, 318.

[163] V. N. Sivkov, V. N. Akimov, and A. S. Vinogradov. *Optics and Spectroscopy* **1987**, 63, 275.

[164] J. T. Waber and D. T. Cromer. Orbital Radii of Atoms and Ions. *J. Chem. Phys.* **1965**, 42, 4116.

[165] E. W. Schlag, D.-Y. Yang, S.-Y. Sheu, H. L. Selzle, S. H. Lin, and P. M. Rentzepis. Dynamical principles in biological processes: A model of charge migration in proteins and DNA. *Proc. Natl. Acad. Sci.* **2000**, 97, 9849.

[166] E.W. Schlag, S.-Y. Sheu, D.-Y. Yang, H.L. Selzle, and S.H. Lin. Distal Charge Transport in Peptides. *Angew. Chem. Int. Ed.* **2007**, 46, 3196.

[167] M. R. Howells, A. P. Hitchcock, and C. J. Jacobsen (Eds.). Special issue on radiation damage. *J. Electron Spectrosc. Relat. Phenom.* **2009**, 170, 1 - 68.

[168] http://www.bessy.de/upload/bitpdfs/mustang.pdf.

[169] J. A. Bearden and A. F. Burr. Reevaluation of X-Ray Atomic Energy Levels. *Rev. Mod. Phys.* **1967**, 39, 125.

A   Experimental details

A.1   Beamlines and experimental end-stations

A.1.1   Russian-German beamline at BESSY II

All presented data were obtained at the Berliner Elektronenspeicherring für Synchrotron-strahlung (BESSY) using radiation from the Russian-German beamline (RGBL) [15, 148]. This dipole bending magnet beamline provides moderate photon flux density distributed continuously over a wide range of photon energies from 30 to 1500 eV and is therefore particularly suitable for PE and near-edge X-ray absorption fine structure (NEXAFS) studies of radiation damage sensitive organic molecules [61, 120, 127, 167]. For beam monochromatization the RGBL is equipped with a plane-grating monochromator resulting in an energy resolution between 80 and 120 meV FWHM when going from the C $1s$ to the O $1s$ absorption threshold. The light spot size at the sample position was $20{\times}80$ μm^2

The spectral dependence of the photon flux was determined using a freshly prepared, clean Au layer as photocathode. Cleanliness of the layer had been checked before by X-ray photoelectron spectroscopy. At the time of the experiments the flux curve of the RGBL exhibited dips in the photon energy range of O $1s$ excitations due to oxygen contamination of the optical elements. This involves the risk to introduce artificial features to O $1s$ NEXAFS spectra upon normalization, because there the photon flux derived structure is much larger than the sample signal. Hence, I decided to repeat XAS measurements in the O $1s$ range at the beamline D1011 of the MAX II storage ring at MAXlab (Lund University, Sweden).

All experiments at BESSY were performed using the MUSTANG end-station [168] at a pressure better than 5×10^{-10} mbar and room temperature. For PE experiments this end-station is equipped with a Phoibos 150 electron energy analyzer for high-energy resolution PE experiments (Specs GmbH). Accounting for thermal broadening the overall energy resolution was set to 150 meV (full width at half maximum, FWHM). Least-squares fit analysis of the spectra was performed using Lorentzian line shapes convoluted with a Gaussian function accounting for limited experimental resolution. Secondary electrons

were factored in the form of an integral (Shirley) background. All spectra were aligned to a binding energy scale relative to the Au $4f_{7/2}$ peak recorded from a reference gold sample and set to 84.0 eV binding energy [169].

XAS spectra were recorded in the total electron yield (TEY) detection mode by recording the sample drain current. They were normalized to the incident photon flux which was recorded with the help of a clean, polycrystalline gold layer. In XAS experiments energy resolution is solely determined by the beamline performance. Energy calibration was done for each spectrum using the energy separation between the first- and second-order light excited Au $4f_{7/2}$ photoemission line taken from a clean gold plate which was additionally mounted to the sample holder.

A.1.2   Beamline D1011 at the MAX-lab facility

Part of the experiments discussed in chapter 5 were repeated at the beamline D1011 located at the MAX II storage ring of the MAX-lab facility (Lund, Sweden). This dipole bending-magnet beamline reveals beam properties very similar to those of the RGBL at BESSY II (cf. A.1.1), with less pronounced structure in the photon flux curve around the O $1s$ absorption threshold, but with worse energy resolution. The XAS experiments were performed using the front experimental station at a pressure better than 5×10^{-10} mbar.

The spectra were recorded in the TEY detection mode by recording the drain current into the irradiated sample. Spectra obtained with the also available MCP detector set to zero eV retarding potential did not deviate from those obtained from monitoring the drain current. Also, after normalization to the incident photon flux, all recorded spectra were identical to the similarly normalized spectra recorded at the RGBL.

A.2   Sample preparation

A.2.1   Mercaptohexanol self-assembled monolayers

One-side polished, naturally oxidized Si wafers (100) were cleaned in an ultrasonic acetone bath and thoroughly rinsed with an ethanolic solution. Subsequently, a 3 nm thick adhesion layer of chromium was deposited at a rate of 0.01 nm/s, followed by a 100 nm layer of gold at 0.1 nm/s. Immediately before adsorption of 6-mercapto-1-hexanol (MCH), the gold film was rinsed with fuming nitric acid for 10 s, subsequently the gold surface was neutralized in a solution consisting of aqueous ammonium (25% solution), hydrogen peroxide (30% solution) and deionised water (NH_3 aq.:H_2O_2:$H_2O \stackrel{\wedge}{=}$ 1:1:5) for 2 min and finally rinsed with deionised water. The cleaned gold film was immersed in a 2% ethanolic solution of MCH for 120 min and then thoroughly rinsed with pure ethanol. The thiol group of the

MCH chemically adsorbs to the gold surface, creating a monolayer of MCH. To minimize adventitious contamination of the MCH monolayer, the sample was not allowed to dry by storing it in deionised water. Only prior to transfering the sample into the UHV chamber, it was dried in argon atmosphere. All chemicals were purchased from Sigma-Aldrich Co.

A.2.2   Genomic DNA

One-side polished, naturally oxidized Si wafers (100) were cleaned in an ultrasonic acetone bath and thoroughly rinsed with an ethanolic solution. Subsequently, a 3 nm thick adhesion layer of chromium was deposited at a rate of 0.01 nm/s, followed by a 100 nm layer of gold at 0.1 nm/s. The gold underlayer ensured good electric contact between the sample and the ground and additionally minimizes the amount of undesired contaminations, e.g. atmospheric adsorbates, by virtue of the low reactivity. 50 μl of double stranded salmon testes DNA (sodium salt, 41.2% GC content, SIGMA Aldrich) with a length of approximately 2000 base pairs were adsorbed from a 1 g/l solution in deionised water and let dry on the substrate. According to the vendor's product information the DNA was extracted in saturated sodium chloride, filtrated and precipitated during the isolation process. The samples were stored under argon atmosphere until they were introduced into the vacuum chamber.

A.2.3   Different $MgCl_2$ concentrations

As DNA probe the following thiol-modified oligonucleotide has been used: O1-SH (5'-HS-$(CH_2)_6$-PO_4-TTT TTT TTT CAT TTC TTA TCA CAG GCT CAA ACC AGT CC-3'). Gold substrates, prepared as in A.2.2 were immersed for 1.5 h in aqueous solutions with 1 μM O1-SH and 0, 2, 20, and 120 mM $MgCl_2$. Subsequently, the samples were treated with 1 mM aqueous MCH solution (Aldrich) for 1 h. After each immobilization step the samples were carefully rinsed with deionized water and blown dry with nitrogen. The samples had been stored in argon atmosphere until they were introduced into the experimental chamber.

A.2.4   Different types of solvent

Ethanolic solution

The pure MCH layer was prepared according to A.2.1. To prepare the samples with 30 and 60 base pairs (bp) double-stranded DNA, thiol-derivatised single-stranded poly-GC DNA (HS-ssDNA) was first hybridized with complementary oligonucleotides in SSC buffer (1x). The thiol group of the HS-ssDNA was attached at the 5' end via a $(CH_2)_6$ spacer. The HS-ssDNA and the complementary oligonucleotides were purchased from

Biozym Scientific GmbH with a concentration of 100 pmol/μl. The starting hybridization temperature was 90°C. The temperature was decreased with a rate of 3.5 K/min down to 6°C. The hybridization product (HS-dsDNA) was adsorbed at the cleaned gold film from 100 pmol/μl solutions in SSC (1x) and PB100 buffer for 60 min, and the sample rinsed with deionised water. Thereafter the prepared DNA samples were treated with MCH, by immersing it in a 2% ethanolic solution of MCH for 120 min and rinsing it thoroughly with pure ethanol. The DNA samples were stored and dried in the same way as described for the MCH sample.

Aqueous solution

The dsDNA was prepared by hybridizing 1 μM GC30-SH (5'-HS-$(CH_2)_6$-PO_4-GCG CCC CGC GGC CCC CCG CCG CCC GCG-3') and GC60-SH (5'-HS-$(CH_2)_6$-PO_4-CCC GGG CGC CGG CCG CGG GGC GCG GCG GCG CGC GGG CGG CCC CGG CGG GGG CGG GCC CCC-3') with 1.05 μM of the complementary oligomers (Biozym Scientific GmbH, Germany) in aqueous solution with 20 mM $MgCl_2$. The concentrations of the complementary strands was used in excess to ensure that all single stranded GC30-SH and GC60-SH were hybridized. Both fragments were hybridized by heating the corresponding solutions up to 95 °C, and then, cooling them down to 4 °C with a cooling rate of 0.1 K/min. Gold substrates prepared as in A.2.2 were then immersed in the 1 μM dsDNA fragment solution for 1.5 h, and then, treated with 1 mM aqueous MCH solution for 1 h.

A.2.5   Simultaneous DNA immobilization and SAM formation

1.05 μM GC30 ssDNA was hybridized with 1 μM GC30 HS-ssDNA in aqueous solution with 20 mM $MgCl_2$. To this end the solution was heated up to 95°C and then cooled down to 4°C with a cooling rate of 0.1 K/min. Subsequently, the immobilization buffer was diluted with an aqueous 20 mM $MgCl_2$, 1 μM MCH solution in order to obtain a 1 μM total thiol concentration with a dsDNA share χ of 0.25, 0.50, 0.75 and 1.00, respectively. Then, gold substrates prepared as in A.2.2 were immersed for 1.5 h. Finally, the samples were rinsed with dionised water and blown dry with nitrogen.

A.2.6   Bacterial surface protein layers on SiO_x/Si

The S layer was isolated from the bacterium B. sphaericus NCTC 9602 as was described previously [117] and deposited onto naturally oxidized Si wafers (SiO_x/Si(100), n-type, commercial grade, 25×6 mm^2 in size), which had been thoroughly cleaned and plasma treated (RF power 20W, 5 min, pressure of ambient gases of 1×10^{-2} mbar) prior to the protein deposition. The protein suspension (1 mg ml^{-1} in 25 mMTris buffer, 10 mM of $MgCl_2$, pH 7.4) was placed *ex situ* onto the substrate for about 30 min. Thereafter the rest

of the protein suspension was removed, the samples were rinsed with deionized water, blow dry with nitrogen and stored under argon atmosphere until they were inserted into the experimental station operating at ultrahigh vacuum conditions. Part of the samples was characterized by transmission electron microscopy (TEM) revealing excellent structural quality of the individual S layer sheets. To determine the degree of substrate coverage and the homogeneity of the S-layer films on the $SiO_x/Si(100)$ substrates, the samples were examined by scanning electron microscopy (SEM) and atomic force microscopy (SFM). It was found that the wafers were homogeneously covered with protein. Typically, surface coverage rates between 60 and 80% were obtained. SFM revealed a thickness of the dried, "as-deposited" S-layer sheets of 5.0 nm.

Acknowledgments

I am deeply grateful to Prof. Clemens Laubschat for the possibility to do my doctoral work in his research group. This holds particularly for the freedom he granted, the constant support in any conceivable way he gave and the trust he put in me and my work. Moreover, I thank every single member of his research group for being the accessible and helpful colleagues they are. This especially accounts to Denis Vyalikh and Serguei Moldotsov who promoted and supported me in many different ways, be it the experimental support and the long nights spent together at the beamline, be it the valuable hints, comments, discussions and cheer-ups–not only with respect to data analysis and research paper writing–which allowed me to benefit from their rich experience in many aspects of the "day-to-day business" in science.

I owe my parents for their love, their trust, their support and the way in which they brought me up. The impact they had on me, my traits and my views has come clearly to my mind only during the time of this work. I also have to apologize to them, my sister and the rest of my family for the little time I could spare to be with them during the last two years.

I thank Michael Mertig, Anja Blüher, Michael Weigel-Jech, Alfred Kick and Martin Bönsch from the BioNanotechnology and Structure Formation Group (Max Bergmann Center of Biomaterials and Institute of Materials Science, Dresden University of Technology) who always provided with samples of excellent quality without which this work would have been infeasible right from the beginning.

I acknowledge the financial support by the Deutsche Forschungsgemeinschaft under the grant No. MO 1049/5-1.

Last but not least, I am indebted to all the friends I found here in Dresden, with whom I shared many wonderful moments and who have always been understanding at the numerous occasions I haven't been able to be with them.

Eigenständigkeitserklärung

Hiermit versichere ich, dass ich die vorliegende Arbeit mit dem Titel "Investigation of structural properties in biomolecular systems using synchrotron-based spectroscopies" ohne unzulässige Hilfe Dritter und ohne Benutzung anderer als der angegebenen Hilfsmittel angefertigt habe; die aus fremden Quellen direkt oder indirekt übernommenen Gedanken sind als solche kenntlich gemacht. Die Arbeit wurde bisher weder im Inland noch im Ausland in gleicher oder ähnlicher Form einer anderen Prüfungsbehrde vorgelegt.

Die Dissertation wurde am Institut für Festkörperphysik in dem Zeitraum von Oktober 2007 bis November 2009 unter der wissenschaftlichen Betreuung von Prof. Dr. C. Laubschat angefertigt.

Die Promotionsordnung der Fakultät Mathematik und Naturwissenschaften an der Technischen Universität Dresden erkenne ich hiermit an.

Dresden, November 2007